Chapter V

Mechanical Stability of Retained Austenite and Efficiency of the TRIP Effect

The mechanical stability of dispersed retained austenite, i.e. the resistance of retained austenite to mechanically induced martensitic transformation, was characterised at room temperature on steels HSiI and LSi differing by their silicon content. The steels had been heat-treated in such a way that each specimen contained the same volume fraction of austenite. Depending on the specimen, retained austenite contained various amounts of carbon and was surrounded by different phases. Measurements of the variation of the volume fraction of untransformed austenite as a function of uniaxial plastic straining revealed that the mechanical properties of the TRIP-assisted multiphase steels result of interactions taking place between the different phases constituting the microstructure. The higher silicon content allows higher carbon enrichment during bainitic tempering. Hence, the mechanical stability of retained austenite is then higher. However, it is shown that, beside the carbon content of retained austenite, strengthening mechanisms occurring in the other phases also influence the austenite resistance to martensitic transformation. The presence of thermal martensite and solid solution strengthening of the idiomorphic ferrite matrix can protect austenite from the externally applied load through a 'shielding effect'. As a consequence, increase of the mechanical stability of retained austenite is not directly related to the decrease of the Ms temperature by carbon enrichment. This chapter also shows that martensitic transformation of retained austenite can be dynamically monitored by acoustic emission measurements during tensile testing. The acoustic emission amplitude appears to scale with the transformation rate of austenite.

1. Introduction

The TRIP effect, i.e. the mechanically induced martensitic transformation of metastable austenite, has been proven for some years to contribute very effectively to the deformation process in a large variety of iron-based alloys. Numerous studies have shown that the mechanically-activated displacive and diffusionless transformation of austenite improves strength and ductility by maintaining a high work-hardening rate during straining [Pat53, Ang54, Zack67, Lud69, Olson75, Ono76, Olson78, Olson82a, b, Strin92, Tamu92]. The effects of *Transformation Induced Plasticity* are classically ascribed to 2 different mechanisms [Lebl89, Mark95]: (i) the stress-assisted nucleation of martensitic variants favourably oriented with respect to the applied stress (*Magee mechanism* [Magee68]), and (ii) the plastic strain of the phases due to the volume and shape changes associated with the displacive transformation (*Greenwood-Johnson effect* [Green65]). Mechanical properties are improved when particular conditions concerning the chemical composition or the testing temperature are fulfilled. In Fe-Ni-Cr alloys [Ang54, Fahr71, Bhan72], Fe-Ni alloys [Yeo63, Bhan72] or in other highly alloyed *fully austenitic steels* [Zack67, Chan71], tensile strength and elongation are markedly enhanced when the chemical composition is such that the M_s temperature is just below the testing temperature. The testing temperature range should be situated just above the M_s^{σ} temperature which separates the regimes of stress-assisted martensitic transformation (on the same nucleation site as during cooling) and strain-induced transformation (when plastic deformation of austenite first occurs and creates new nucleation sites for transformation). In addition to M_s and M_f describing the thermal stability of austenite, M_s^{σ} has been proposed as a characteristic of the mechanical stability of austenite. This means that the (meta)stability of austenite, i.e. the lack of driving force for spontaneous transformation without external work, has to be so controlled that the combination of transformation plasticity and classical plasticity favourably influences the work-hardening rate and therefore delays the onset of necking [Lud69].

Martensitic transformation of metastable austenite has also been reported to improve toughness of ultra-high strength martensitic [Haid87, Haid88] and bainitic steels [Sand81, Miih87, Tomi93] when austenite is present as a *dispersed phase* in the microstructure. Also in these steels, the effect of deformation-induced transformation of dispersed austenite on fracture-controlling processes depends on the austenite mechanical stability which can be tuned by parameters such as austenite shape [Bhad83], size, or chemical composition [Haid87, Haid88].

The TRIP effect is also thought to be the main phenomenon responsible of the improved balance of strength and ductility exhibited by the TRIP-assisted multiphase steels

[Mats87]. Indeed, chapter IV has shown that for the conventional high silicon TRIP-aided steels, improvement of both strength and ductility can be related to the presence of retained austenite that transforms during straining.

The present literature dealing with the TRIP-assisted multiphase steels has not elucidated how exactly the TRIP effect influences mechanical properties and, especially, which parameters of the microstructure control the mechanical stability of retained austenite. While some studies have shown that mechanical properties improve when the initial volume fraction of retained austenite increases (which requires increases of the carbon, silicon and manganese contents) [Tsuk91, Mats92, Saku92a, b], other works have shown that the stability of retained austenite has also to be taken into account [Saku91a, b, Itam95]. A superior strength-ductility balance is attained when strain-induced transformation of austenite occurs gradually during plastic flow. However, austenite stability was directly related to its carbon enrichment at the end of the bainitic tempering. Whereas Sugimoto et.al. [Sugi93] and Itami et. al. [Itam94] have shown that the morphology of retained austenite influences its stability, hardly anything has been reported on the role of the other phases surrounding retained austenite.

Chapter IV has shown that the maximum strength-ductility balance of both conventional high silicon and new low silicon TRIP-assisted multiphase steels corresponds to the retention of a maximum volume fraction of retained austenite in the microstructure and therefore to an effective TRIP effect. However, it was concluded that beside a TRIP effect, a composite strengthening effect related to the presence of martensite also affects the mechanical properties of the low silicon TRIP-aided steels. Furthermore, even if the mechanical properties exhibited by such a low silicon steel are quite remarkable when compared to the properties of Dual-Phase steels or of solid-solution and precipitation hardened high-strength steels, they remain lower than the properties of conventional high silicon TRIP-assisted multiphase steels with the same global carbon content. It was shown in chapter IV that despite a similar microstructure and a similar retained austenite volume fraction, the true stress at maximum load and the true uniform strain were globally lower (by 100 MPa and 0.05 respectively) as compared with a similar TRIP-aided steel differing only by a higher silicon content [Jac98a].

The purpose of this chapter is to contribute to the understanding of the factors governing the transformation of retained austenite during uniaxial tensile testing at room temperature. We investigate the influence of the TRIP effect on the mechanical properties of 2 cold-rolled C-Mn-Si TRIP-assisted multiphase steels differing by their silicon content, i.e. steels HSiI and LSi. The influences of chemical composition and heat-treatment parameters on

the stability of retained austenite will be elucidated. It will be shown that the mechanically-induced transformation of retained austenite is influenced not only by the carbon concentration of retained austenite but also by the properties of the other phases in the microstructure.

Furthermore, a correlation between the transformation rate of austenite during plastic flow and acoustic emission will be established. It is well known that martensitic transformation can be monitored with the help of acoustic emission measurements [Spei71]. Martensitic transformation leads to the generation of transient elastic waves propagating through the matrix with an energy proportional to the volume of the transformed region [Spei71, Mohr86]. Acoustic emission has therefore been widely used in studies dealing either of the martensitic transformation during cooling or of the straining of fully austenitic stainless steels [Taka80, Zhu92, Moor95]. Furthermore, Tseng et al. [Tseng87] have shown that acoustic emission can be used for monitoring martensitic transformation of austenite in Dual Phase steels during cooling and straining. However, nothing can be found in the literature on the use of acoustic emission measurements for online monitoring martensitic transformation of dispersed retained austenite in TRIP-assisted multiphase steels. This study will show that the continuous acoustic emission recorded during uniaxial tensile testing of TRIP-assisted multiphase steels can be related to the martensitic transformation of retained austenite and to dislocation motion.

2. Experimental Procedure

Steels HSiI and LSi differing by their silicon contents were investigated in this chapter. Their chemical compositions are reminded in Table 5.1. A cast ingot of steel HSiI was hot-rolled to a thickness of 4mm following a classical route. Coiling was simulated at relatively low temperature (550°C for 1h –see chapter II). Steel HSiI was then cold-rolled 75% to 1mm in thickness. Steel LSi is an industrial steel hot-rolled to a thickness of 5.5mm following classical practice. Steel LSi was cold-rolled 82% also to the thickness of 1mm.

(10^{-3} wt.%)	C	Mn	Si	P	S	Cr	Ni	Cu	Nb	Al	N
HSiI	130	1420	1500	13	9	13	20	8	0	27	7.9
LSi	160	1300	380	13	12	19	27	19	13	30	6.3

Table 5.1: Chemical compositions (10^{-3} wt.%) of the investigated steels.

Heat-treatments were carried out on 40mm x 240mm samples oriented in the rolling direction. The heat-treatment scheme is schematically represented in figure 5.1. Table 5.2

shows the 3 particular heat-treatment conditions (intercritical annealing temperature (T_1) and time (t_1) and bainitic tempering temperature (T_2) and time (t_2)) used for the 2 steel grades. These heat-treatment conditions correspond to a range of favourable combinations of strength and ductility which had been determined in previous chapter [Jac98a, b] (other bainitic tempering times will also be considered in this chapter for steel LSi).

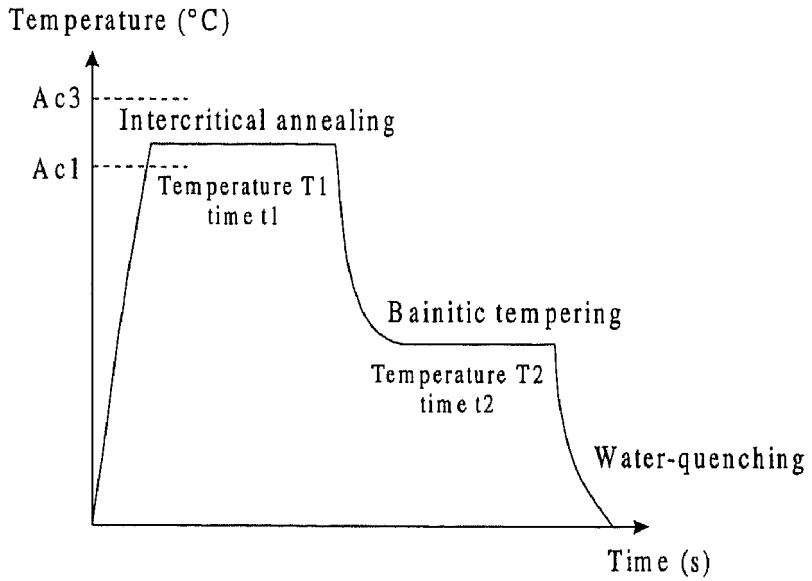

Figure 5.1: Schematic representation of the heat-treatment scheme applied after cold-rolling in order to generate the multiphase microstructure.

HSiI		
	I	760°C/2min/410°C/5min
	II	775°C/2min/360°C/5min
	III	775°C/2min/410°C/5min
LSi		
	IV	730°C/5min/370°C/30s
	V	730°C/5min/370°C/1min
	VI	730°C/5min/370°C/3min

Table 5.2: Heat-treatment conditions of the 3 different specimens of each steel grade considered in this chapter.

Tensile specimens were prepared according to the European standard EN10002-1. The initial gauge length was 50mm and the width was 12.5mm. Tensile testing was done at a crosshead speed of 2mm/min. Measured loads and elongations were converted to true stress - true strain curves. As in chapter IV, strain hardening was characterised by the incremental strain-hardening exponent ($n_{incr.}$).

Microindentation Vickers hardness measurements of the idiomorphic ferrite matrix were carried out on samples of steels HSiI and LSi. Because of the small grain size of ferrite (~5-10μm), loads of 1 and 2g were chosen in order to keep the indentation size small enough in comparison to the grain size. Prior to these tests, the samples were mechanically polished to 0.25μm diamond paste and then electrolytically polished for 10min in a solution of 5% $HClO_4$ and 95% glacial acetic acid in order to remove any work hardened surface layer. They were finally etched with 2% Nital for revealing the different phases. After indentation, the diagonals and area of the impressions were precisely measured by scanning electron microscopy (SEM). These measurements were calibrated by carrying out the same indentation tests with 1 and 2g load on standards of known hardness under 10g.

Microstructures were studied by scanning electron microscopy (SEM). The procedure used for the preparation of the specimens can be found in chapter II. The initial retained austenite content of the samples as well as the evolution of the volume fraction of austenite after different extents of plastic straining were measured by Mössbauer spectroscopy. Mössbauer spectroscopy is more sensitive and more accurate than X-ray diffraction and is not influenced by the crystallographic texture. 20mm long samples were cut from the tensile test specimens and chemically thinned to a thickness of 100μm using a solution of 14ml of 40% HF and 100ml of 30% H_2O_2 diluted in 100ml distilled water. These samples were then electrolytically polished at ±15°C in a solution of 5% $HClO_4$ and 95% glacial acetic acid to a thickness of 30 to 50 μm. As described in chapter III, the volume fractions of idiomorphic ferrite, bainite and martensite were determined by combining results from image analysis and dilatometry. The carbon content of retained austenite was estimated from the lattice parameter measured by X-ray diffraction using Cu-Kα radiation. The lattice parameter determined using the $(220)\gamma$ and $(311)\gamma$ peaks was converted to carbon content by using the relationship $a_0(Å) = 3.578 + 0.033\ C(wt.\%)$. The effects of manganese and silicon on the austenite lattice parameter were taken into account by using the corrections proposed by Dyson et.al. [Dyson70].

The acoustic emission of the samples was monitored during tensile tests. The transducer with a bandwidth of 100-300 kHz was directly attached to the gauge length of the sample using a thin layer of high vacuum grease as coupling medium. The pre-amplifier gain was fixed at 40 dB. The continuous emission was measured using the Average Signal Level (ASL). In contrast to the Root Mean Square (RMS), the ASL is a time-average of the continuous emission obtained by integration of the logarithmically (rather than linearly) amplified AE signal. The ASL therefore allows measurement over a wider dynamic range at the expense of resolution (which is of 1dB). The background noise level was 7 dB for all the tests.

3. Results

3.1 Microstructure and Mechanical Properties

Figure 5.2 shows typical SEM micrographs of the microstructure of steel HSiI after the 3 heat treatment conditions considered for this steel grade. Idiomorphic ferrite constitutes the major phase of the microstructure while non idiomorphic ferrite phases (i.e. bainite and retained austenite) are dispersed at the grain boundaries of the ferrite grains. As a consequence of the higher intercritical temperature for specimens II and III (i.e. 775°C instead of 760°C), the volume fraction of non-idiomorphic ferrite phases is larger. Retained austenite is associated with bainite either as remaining part of the initial intercritical austenite grains (*'blocky' type austenite*) or as inter-laths films (*'film' type austenite*). No martensite can be found in the microstructure at the end of heat-treatments I and III (i.e. 5 minutes at 410°C). However, some grains of martensite can be found after the heat-treatment II (which corresponds to a bainitic tempering at a lower temperature (360°C) for the same time of 5 min) (see chapter III).

Figure 5.3 presents SEM micrographs of the microstructure obtained at the end of the 3 particular heat-treatments considered in the case of steel LSi. For these 3 specimens, the intercritical temperature (730°C) and time (5 min) as well as the bainitic tempering temperature (370°C) were kept identical. Only the nature of the second phases has changed as a consequence of the change of the bainitic tempering time (30s, 1 min and 3 min). Specimens IV and V with the shortest bainitic tempering times contain martensite while only bainite and retained austenite can be found in specimen VI. In addition to grain boundary grains, steel LSi specimens also contain very small intra-ferritic austenite grains (*'isolated' type austenite*) resulting from the intercritical annealing of cold-rolled pearlite colonies [Jac98b]. It is also noteworthy that the ferrite grain size is slightly smaller in steel LSi than in steel HSiI.

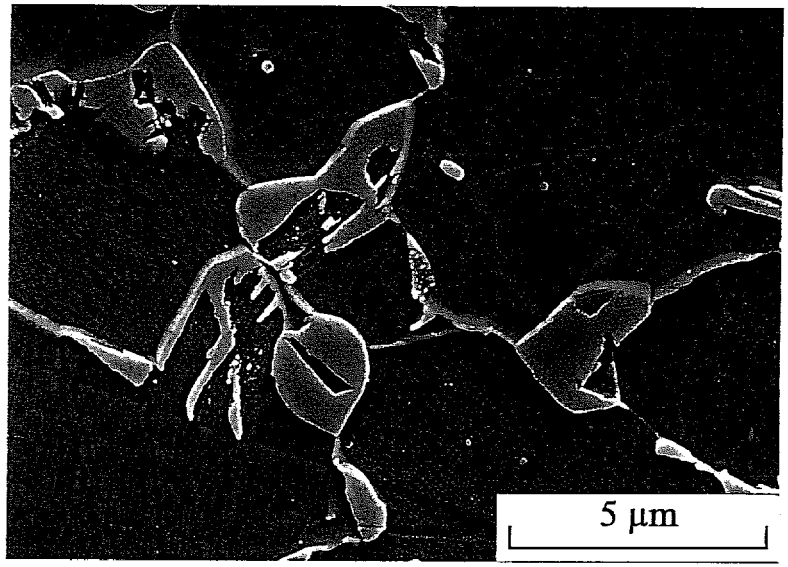

(a)

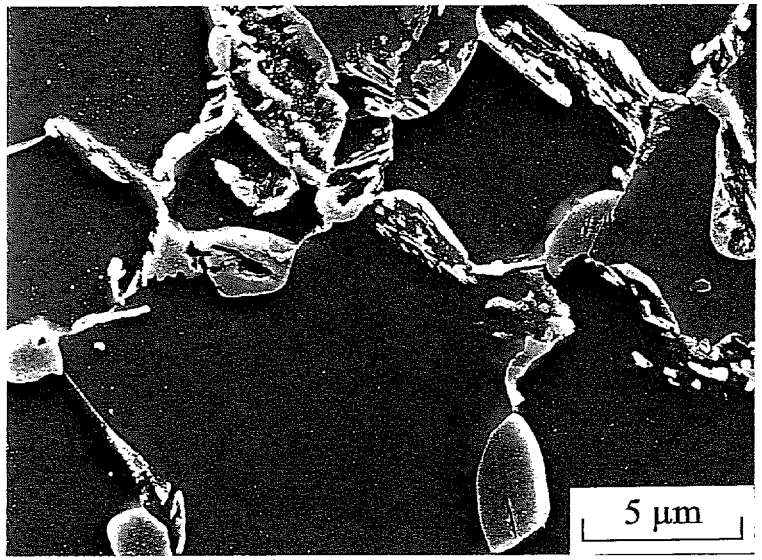

(b)

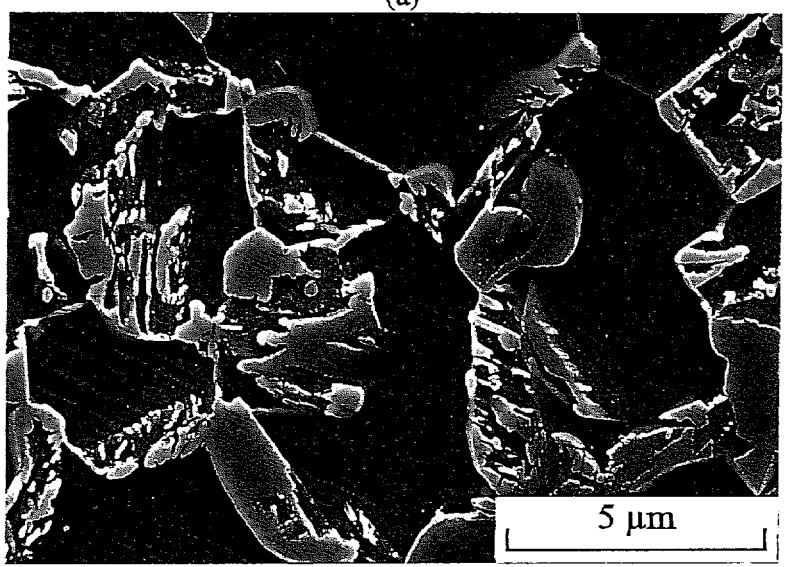

(c)

Figure 5.2: SEM micrographs of the typical microstructure of steel HSiI after the 3 different heat-treatments; (a) specimen I, (b) specimen II, and (c) specimen III.

(b)

5 µm

(a)

(c)

Figure 5.3: SEM micrographs of the typical microstructure of steel LSi after the 3 different heat-treatments; (a) specimen IV, (b) specimen V, and (c) specimen VI.

The volume fractions of the different phases constituting the microstructure of the 6 specimens as well as the carbon content of retained austenite are given in Table 5.3. All specimens contain nearly the same volume fraction of retained austenite, except specimen

VI which contains slightly less austenite. Idiomorphic ferrite is always the major phase while the volume fractions of bainite are around 30% for specimens II and III and around 10 - 20% for the other specimens. Specimens IV and V contain 5 to 10% of martensite which means that the Ms temperatures after these 2 heat treatment conditions are above room temperature. Specimen VI of steel LSi corresponds to the shortest bainitic tempering time at 370°C needed to lower the Ms temperature to room temperature (see chapter III). For steel HSiI, specimens I and III have a Ms temperature below room temperature, while the presence of some grains of martensite in the microstructure of specimen II means that its Ms temperature is just above room temperature.

			Ferrite (F) (%)	Bainite (B) (%)	Retained Austenite ($V_{\gamma r}$) (%)	'Thermal' Martensite (M_{therm}) (%)	Carbon content of $R\gamma$ (wt.%)	
HSiI					± 0.5			
	I	760°C/2min/410°C/5min	~ 75	~ 15	8	0	0.93	Ms < Tamb.
	II	775°C/2min/360°C/5min	~ 60	~ 30	7.9	~ 0	0.85	Ms ~ Tamb.
	III	775°C/2min/410°C/5min	~ 60	~ 30	7.8	0	0.97	Ms < Tamb.
LSi								
	IV	730°C/5min/370°C/30s	~ 75	~ 9	8.8	~ 7	0.61	Ms > Tamb.
	V	730°C/5min/370°C/1min	~ 75	~ 12	8.1	~ 5	0.68	Ms > Tamb.
	VI	730°C/5min/370°C/3min	~ 75	~ 19	6.1	0	0.73	Ms ~ Tamb.

Table 5.3: Volume fractions of the different phases constituting the microstructure of each specimen and carbon content of retained austenite as estimated by X-ray diffraction.

Table 5.3 also gives the austenite carbon content estimated from the lattice parameter measured by x-ray diffraction. Specimens of steel HSiI present a higher carbon enrichment of austenite than specimens of steel LSi. For specimens I and III, the carbon content reaches the maximum carbon enrichment of austenite allowed by the T_0-curve at 410°C for this steel composition (see chapter III). For specimen II, the carbon content of austenite is lower and does not reach the maximum predicted by the T_0-curve. For steel LSi, the carbon enrichment is lower because of the shorter bainitic holding times and because of the loss of carbon by partial carbide precipitation (see chapter III). The carbon content of austenite in specimen IV (with the shortest tempering time) is only somewhat higher than the level estimated by considering that all carbon concentrates in the 25% intercritical austenite formed at 730°C. Further bainitic tempering of steel LSi is accompanied by a carbon enrichment of austenite. After 3 minutes, austenite then becomes sufficiently carbon-rich that it does not transform to martensite during cooling to room temperature.

Figure 5.4 presents the true stress - true strain curves of the different specimens. Following the results of chapter IV, steel HSiI (figure 5.4(a)) exhibits better mechanical properties than steel LSi, i.e. higher true stresses at maximum loads and larger true uniform strains. Specimen II presents the highest true stress at maximum load but a lower true uniform strain than specimens I and III. The best strength-ductility combination is obtained with specimen I. Mechanical properties of steel LSi (figure 5.4(b)) are globally lower than that of steel HSiI. It can be seen that, when the bainitic tempering time increases from specimen IV to VI, the true stress at maximum load decreases and the yield strength increases. Specimen V with the intermediate bainitic tempering time presents the largest true uniform strain for specimens of steel LSi.

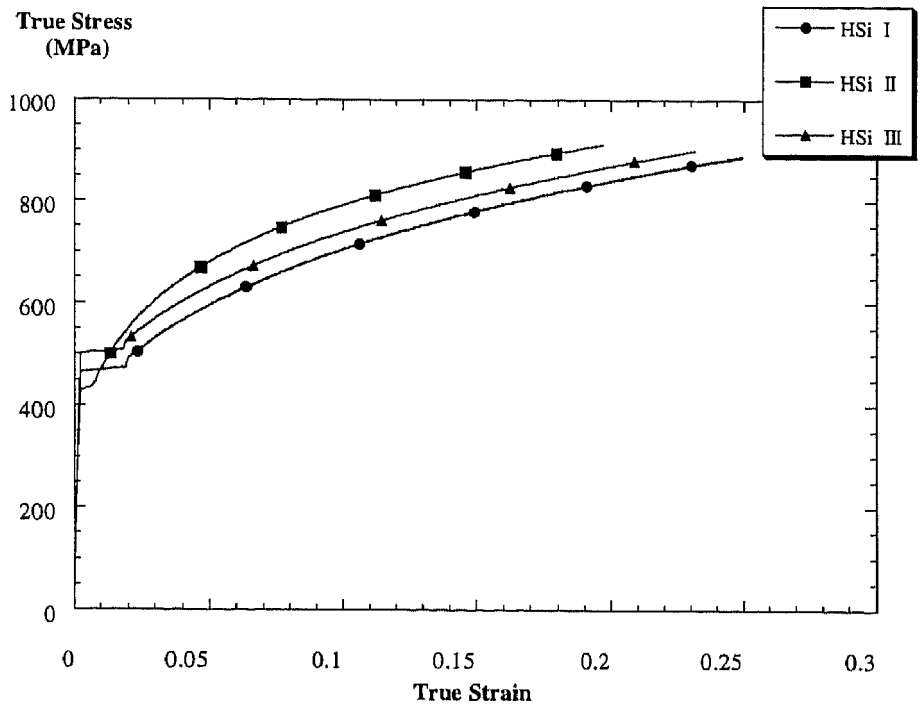

(a)

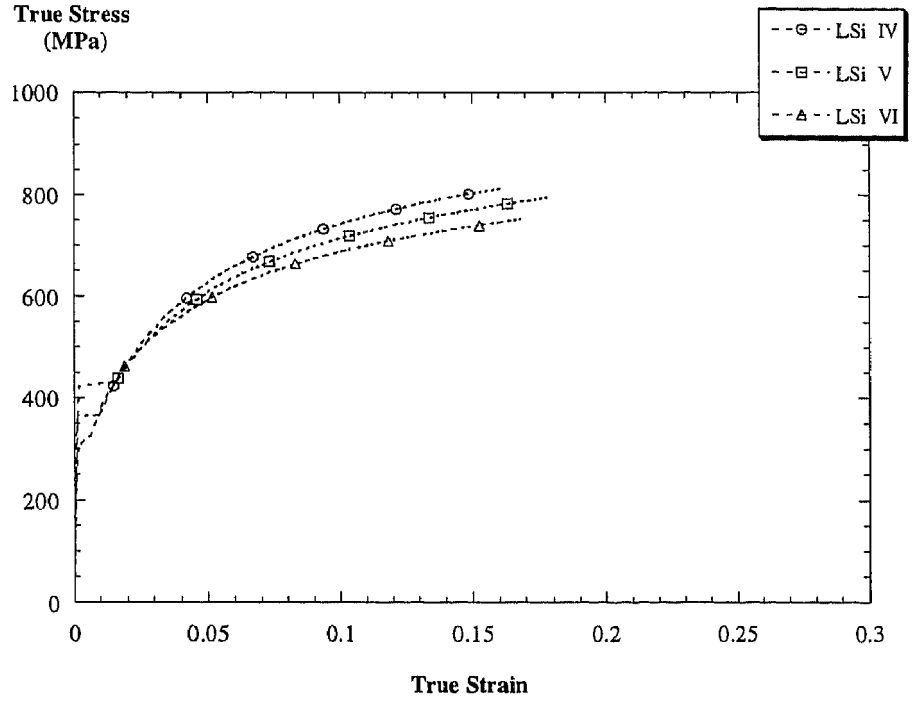

(b)

Figure 5.4: True stress – true strain curves of (a) the specimens of steel HSiI and (b) the specimens of steel LSi.

Figure 5.5 presents the variation of the incremental work-hardening ($n_{incr.}$) as a function of strain. The straight line corresponds to the instability criterion ε_u=n. It appears that the different strength-ductility combinations are associated with completely different work-hardening behaviours. The large true uniform strains of specimens I and III of steel HSiI are due to the maintaining of a high, slightly increasing incremental work-hardening exponent during straining. Specimen II presents a higher value of $n_{incr.}$ after the Lüders plateau than specimens I and III. However, this high initial level does not maintain and the progressive decrease of $n_{incr.}$ induces an earlier onset of necking (when the instability criterion is fulfilled). In comparison to steel HSiI, specimens of steel LSi present a completely different evolution of hardening during plastic straining. After the onset of yielding, $n_{incr.}$ increases first to very high values (0.3-0.35) for specimens IV and V. $n_{incr.}$ thereafter decreases steeply to values lower than for steel HSiI.

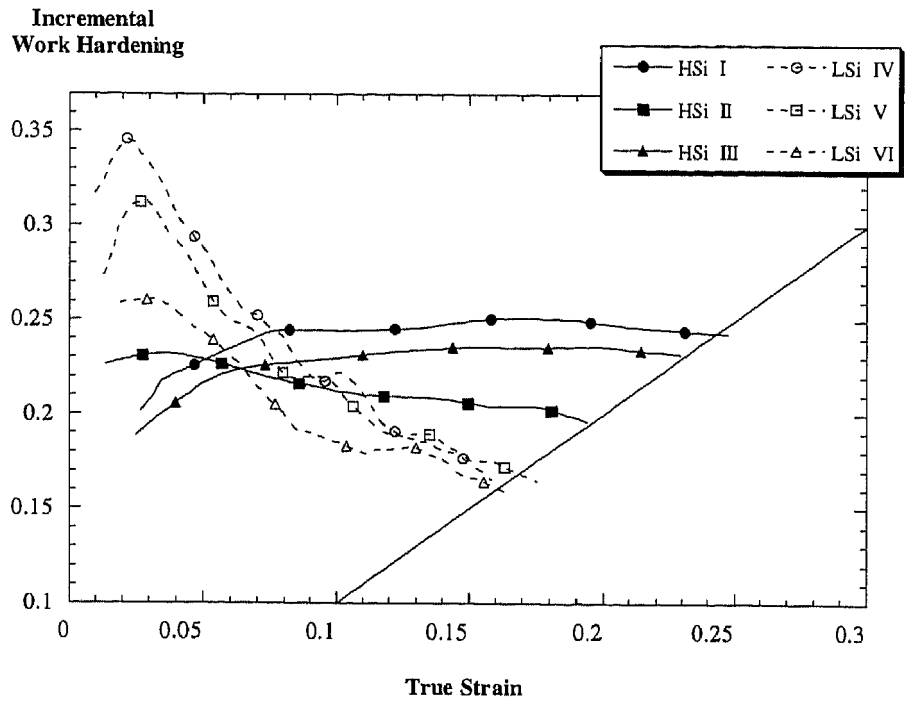

Figure 5.5: Incremental work-hardening curves ($n_{incr.}$) of the different specimens of steels HSiI and LSi.

In summary, in the case of steel HSiI, the best mechanical properties with a delayed onset of necking correspond to an initial low value of $n_{incr.}$ which increases with true strain. For steel LSi, the best mechanical properties are obtained when $n_{incr.}$ shows a high initial value that decreases with true strain [Jac98b].

Figure 5.6 summarises the microindentation measurements of the hardness of idiomorphic ferrite grains in specimens I of steel HSiI and in specimen VI of steel LSi. For steel LSi, specimen VI was chosen in order to avoid any possible effect of the presence of internal stresses generated by the formation of martensite during cooling. Up to 100 measurements have been made in each case. As the same mean value of hardness was obtained with loads of 1 and 2g, all measurements have been collected together. It can be seen that the ferrite matrix of steel HSiI has a significantly higher hardness than that of steel LSi[1].

[1] The same difference in the hardness of the idiomorphic ferrite matrix of steels HSiI and LSi has been recently also observed by nanoindentation measurements by using an atomic force microscope (AFM). The measurements have been carried out at University of Saarland, Department of Materials Science, University Bldg. 43B, P.O. Box 151150, D-66041 Saarbrueken, Germany. We acknowledge Dr. M. Göken for the provision of the experimental facilities.

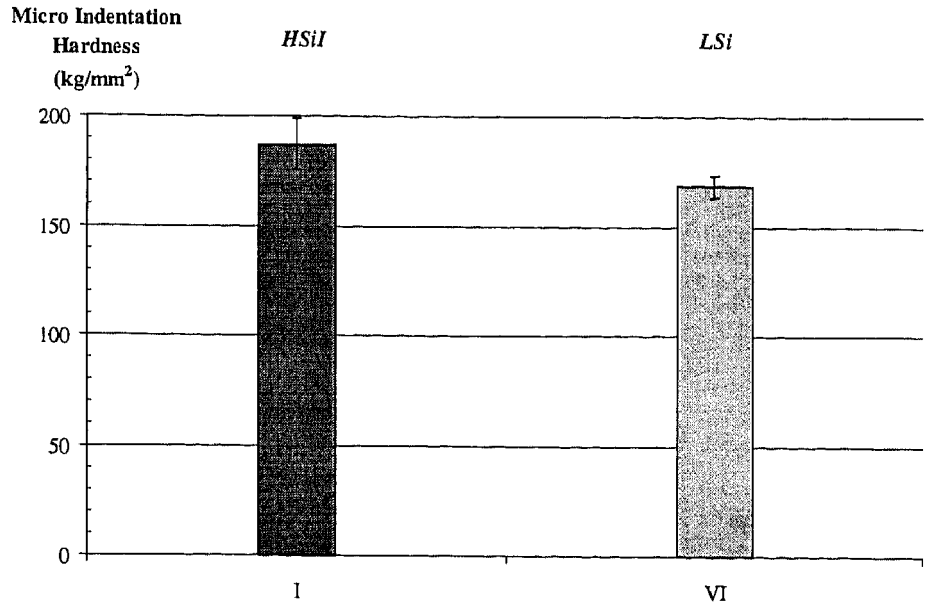

Figure 5.6: Micro-indentation hardness of specimen I of steel HSiI and of specimen VI of steel LSi (loads of 1 and 2 g).

3.2 Retained Austenite and Plastic Strain

Figure 5.7 presents the evolution of the retained austenite content with plastic strain for each heat-treatment conditions of steels HSiI and LSi. Even though all specimens contain about the same initial content of retained austenite, the rate of austenite transformation during plastic straining is different. Retained austenite content decreases more slowly for specimens of steel HSiI (figure 5.7(a)). For specimens I and III, almost no austenite transforms before a strain of 0.04. Austenite then transforms very progressively at larger strain. For specimen II of steel HSiI and for the 3 specimens of steel LSi (figure 5.7(b)), retained austenite contents decrease more rapidly. The fastest austenite transformation rate is observed for specimens IV and VI. It is noteworthy that part of austenite remains untransformed when the samples have been strained up to the onset of necking. This is more clearly seen on figure 5.8 which presents the variation of the proportion of retained austenite transformed to martensite ($1-V\gamma_r/V\gamma_{r0}$) as a function of normalised strain $\varepsilon/\varepsilon_u$. A variable portion of retained austenite does not transform to martensite during uniform tensile testing. For specimens of steel HSiI, only 50 to 60% of the initial volume fractions of austenite transforms before the onset of necking. This proportion is larger for steel LSi: it is then comprised between 65 and 80%. Figure 5.8 best illustrates that austenite transforms very progressively for specimens I and III but very much faster for specimens IV and VI. For these 2 latter samples, all the *transformable* retained austenite is already transformed after only 30% of the true uniform strain. In the case of steel LSi, specimen V

with an intermediate bainitic tempering time exhibits a particular behaviour: the austenite transforms more progressively and the fraction of austenite transformed at the onset of necking is larger than for specimens IV and VI with shorter and longer bainitic tempering times, respectively.

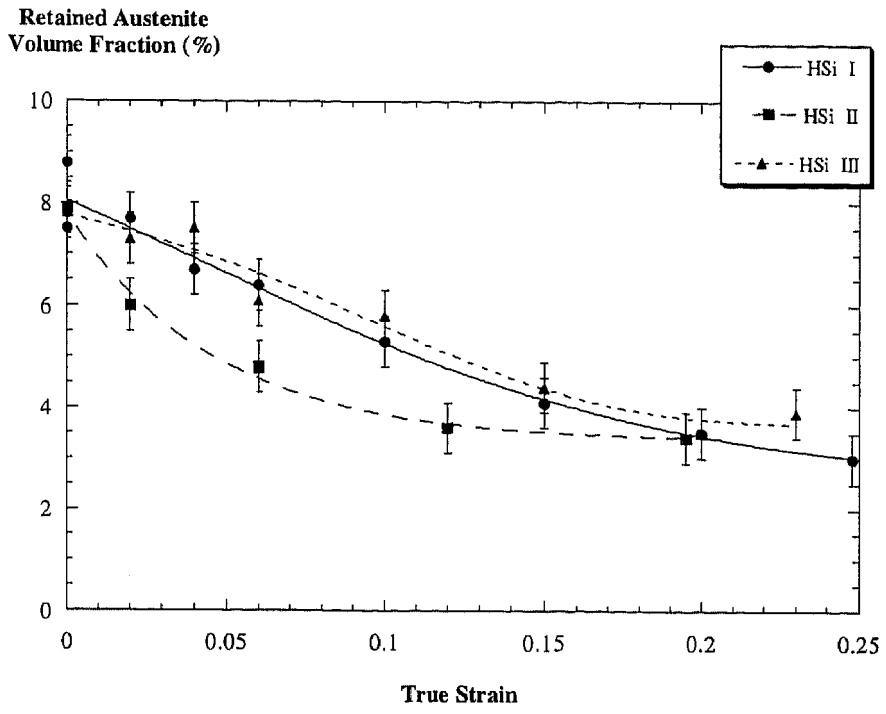

(a)

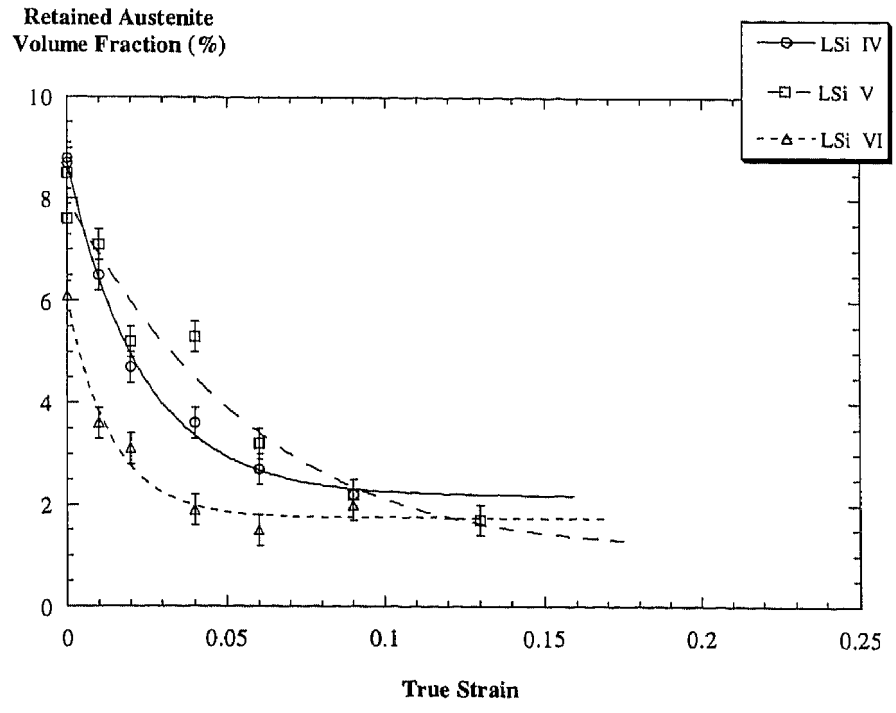

(b)

Figure 5.7: Retained austenite content as a function of true strain for specimens of (a) steel HSiI, and (b) steel LSi.

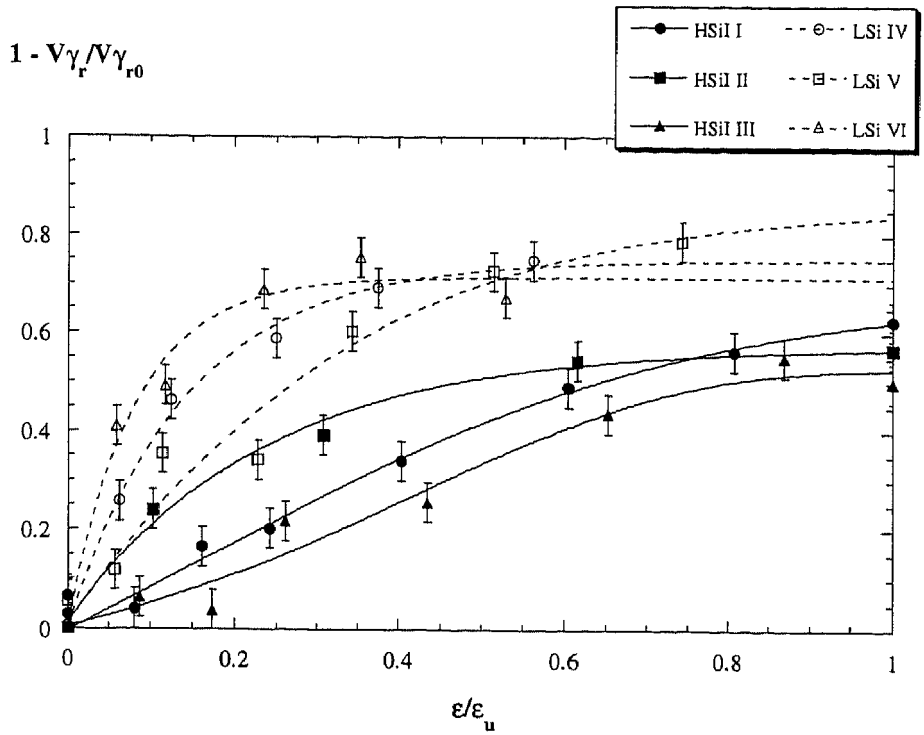

Figure 5.8: Proportion of transformed austenite as a function of true strain normalised by true uniform strain of the specimens of steels HSiI and LSi, respectively.

In order to estimate the transformation rate of retained austenite during plastic straining, the variations of the normalised *transformable* austenite have been exponentially fitted on figure 5.9:

$$\frac{V\gamma - V\gamma_{\varepsilon_u}}{V\gamma_0 - V\gamma_{\varepsilon_u}} = ke^{-n\varepsilon}$$

where $V\gamma_{\varepsilon u}$ is the volume fraction of retained austenite remaining untransformed at true uniform strain; $V\gamma_0$ is the initial volume fraction of retained austenite; k and n are constants. The transformation rate can be thus related to n.

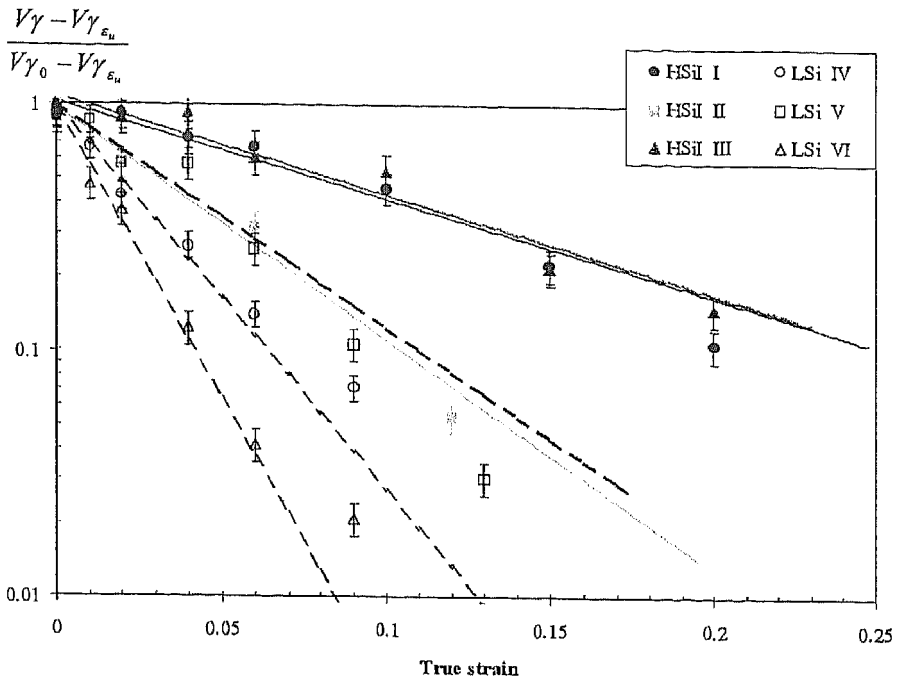

Figure 5.9: Variations of the transformable austenite as a function of true strain for the different specimens of steels HSiI and LSi. The straight lines correspond to the exponential fit.

We can see on figure 5.9 that specimens I and III of steel HSiI show a low transformation rate. Specimen II of steel HSiI and specimen V of steel LSi show similar transformation rates, slightly higher than for specimens I and III. For specimens IV and VI of steel LSi, the transformation rates are very high. It is surprising that specimen VI which contains a higher austenite carbon content than specimens IV and V (Table 5.3) transforms very rapidly like specimen IV which contains less carbon in austenite.

3.3 Acoustic Emission

In order to distinguish the contributions to acoustic emission due to the motion of dislocations and to the TRIP effect, the acoustic emission was measured during tensile testing of samples of steel LSi heat-treated in such a way as to present either a ferrite-martensite microstructure or a ferrite-bainite microstructure. The ferrite-martensite specimen was obtained after an isothermal holding of 5min at 730°C (i.e. the same intercritical conditions as for specimens IV to VI) followed by a direct water-quenching to room temperature ('Dual Phase' specimen). The ferrite-bainite specimen was obtained after a bainitic tempering of 30 minutes at 370°C (after the same intercritical annealing conditions). As shown in chapter III, only 1% of retained austenite remains in the microstructure after such a heat-treatment. The true stress – true strain curve together with

the ASL (Average Signal Level) are given in figure 5.10 for these 2 specimens. Both specimens exhibit intense continuous emission at the beginning of plastic straining. The ferrite-martensite sample (figure 5.10(a)) exhibits continuous yielding during which a maximum of the ASL is observed. The ASL then decreases progressively and nearly reduces to the noise level at the onset of necking. For the ferrite-bainite specimen (figure 5.10(b)), the initial ASL peak is observed during the Lüders plateau. The acoustic emission signal abruptly decreases at the end of the plateau and a low, progressively decreasing ASL is then recorded to the onset of necking.

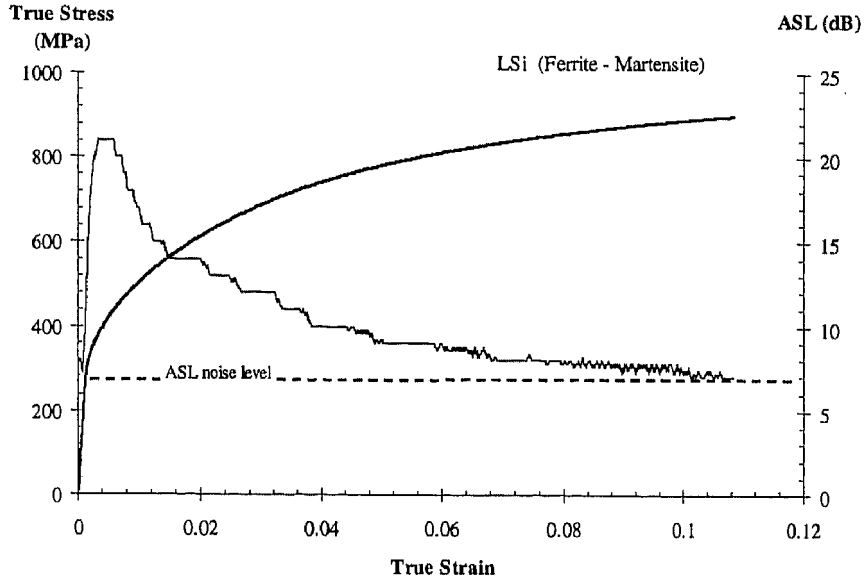

(a)

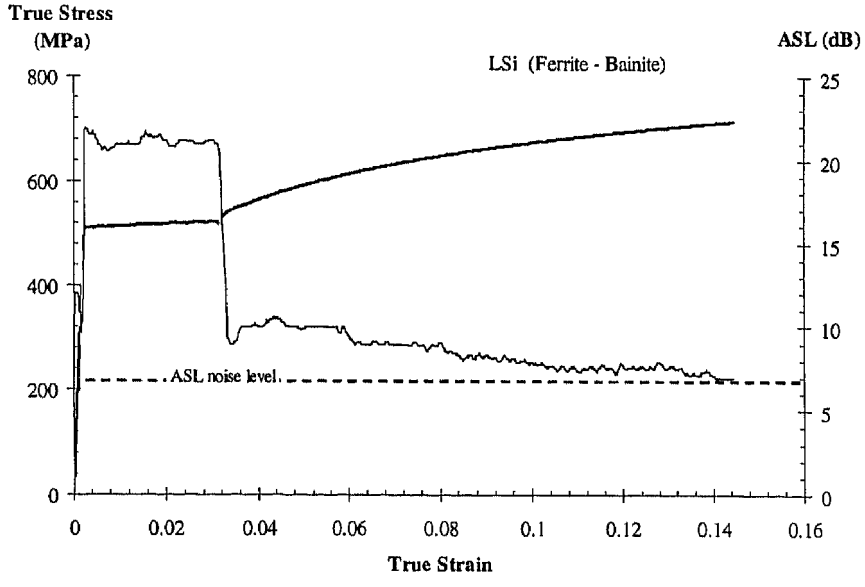

(b)

Figure 5.10: True stress - true strain curve and corresponding acoustic emission Average Signal Level (ASL) of steel LSi with (a) ferrite - martensite and (b) ferrite - bainite microstructures.

Figure 5.11 presents the true stress - true strain curves of the 3 specimens of steel HSiI together with the ASL levels measured during testing. The 3 ASL curves exhibit a first peak corresponding to the Lüders plateau. However, the acoustic emission does not decrease continuously afterwards as in the case of the ferrite-martensite and ferrite-bainite microstructures (figure 5.10). A higher ASL level with a few additional peaks can be observed for the 3 specimens. For specimen II (figure 5.11(b)), the ASL is high up to a true strain of 0.09 and then decreases quite rapidly to the noise level. For specimens I and III (figures 5.11(a) and 5.11(c)), the continuous emission is lower after the Lüders plateau than for specimen II, but a constant ASL level is maintained up to higher values of true strain (around 0.16 and 0.19 for specimens I and III respectively).

True stress - true strain curves together with ASL curves of specimens of steel LSi are presented in figure 5.12. Once again, the ASL curves present a high initial level corresponding to the onset of yielding or to the Lüders plateau. However, in comparison with the specimens of steel HSiI, the acoustic emission disappears earlier during straining for steel LSi. Despite similar initial peak values for steels HSiI and LSi, the ASL levels of specimens IV to VI become lower than the noise level for true strains larger than 0.12 (i.e. 2/3 of the true uniform strain) while acoustic activity can be detected up to true uniform strain for specimens I to III. Specimen IV (figure 5.12(a)) presents a higher initial ASL level which decreases more rapidly after a true strain of 0.04. Specimen V (figure 5.12(b)) keeps a high continuous acoustic emission for a true strain up to 0.06. Specimen VI (figure 5.12(c)) presents a low ASL level after the Lüders plateau.

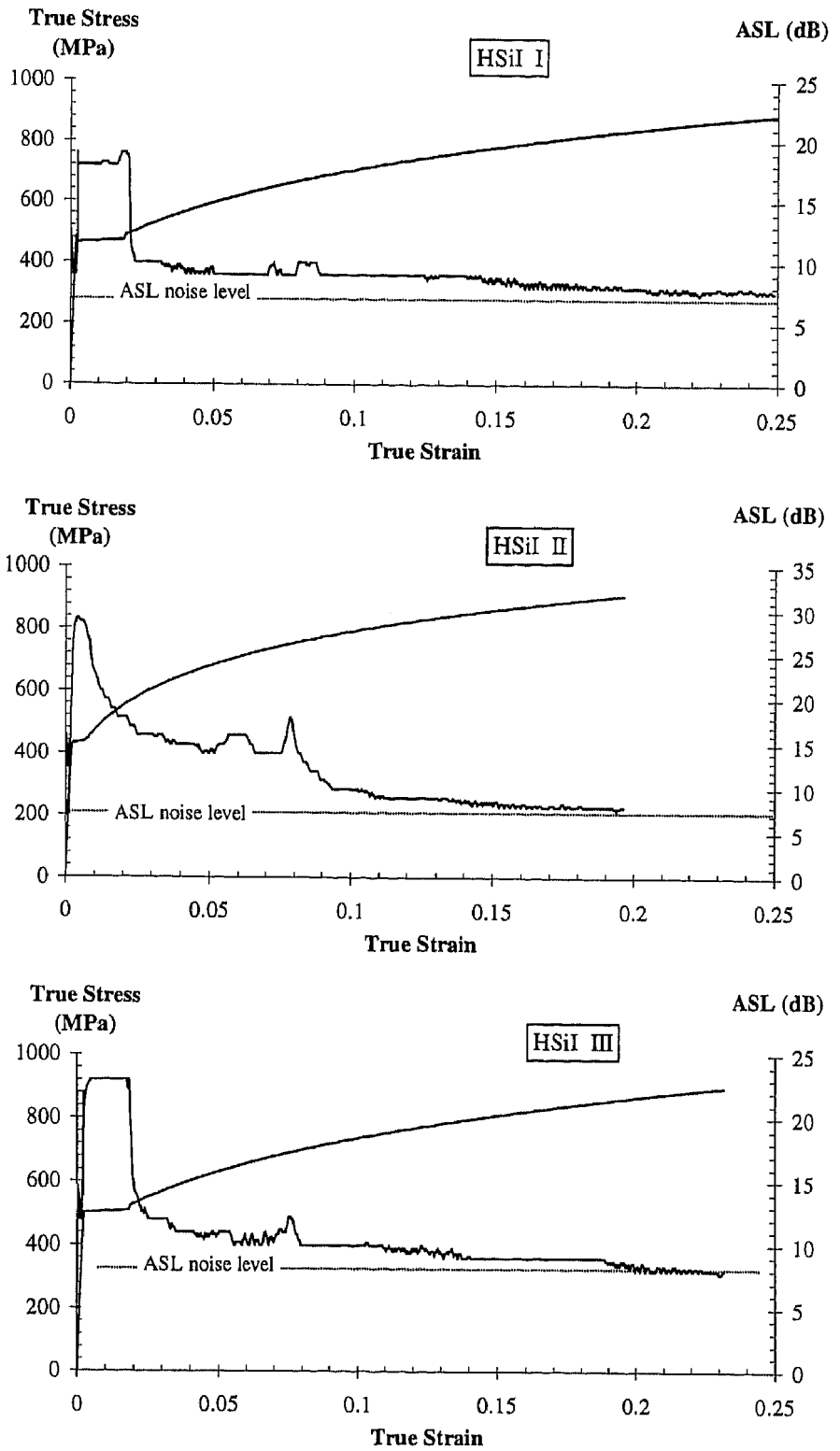

Figure 5.11: True stress – true strain and acoustic emission ASL curves for specimens I, II, and III of steel HSiI.

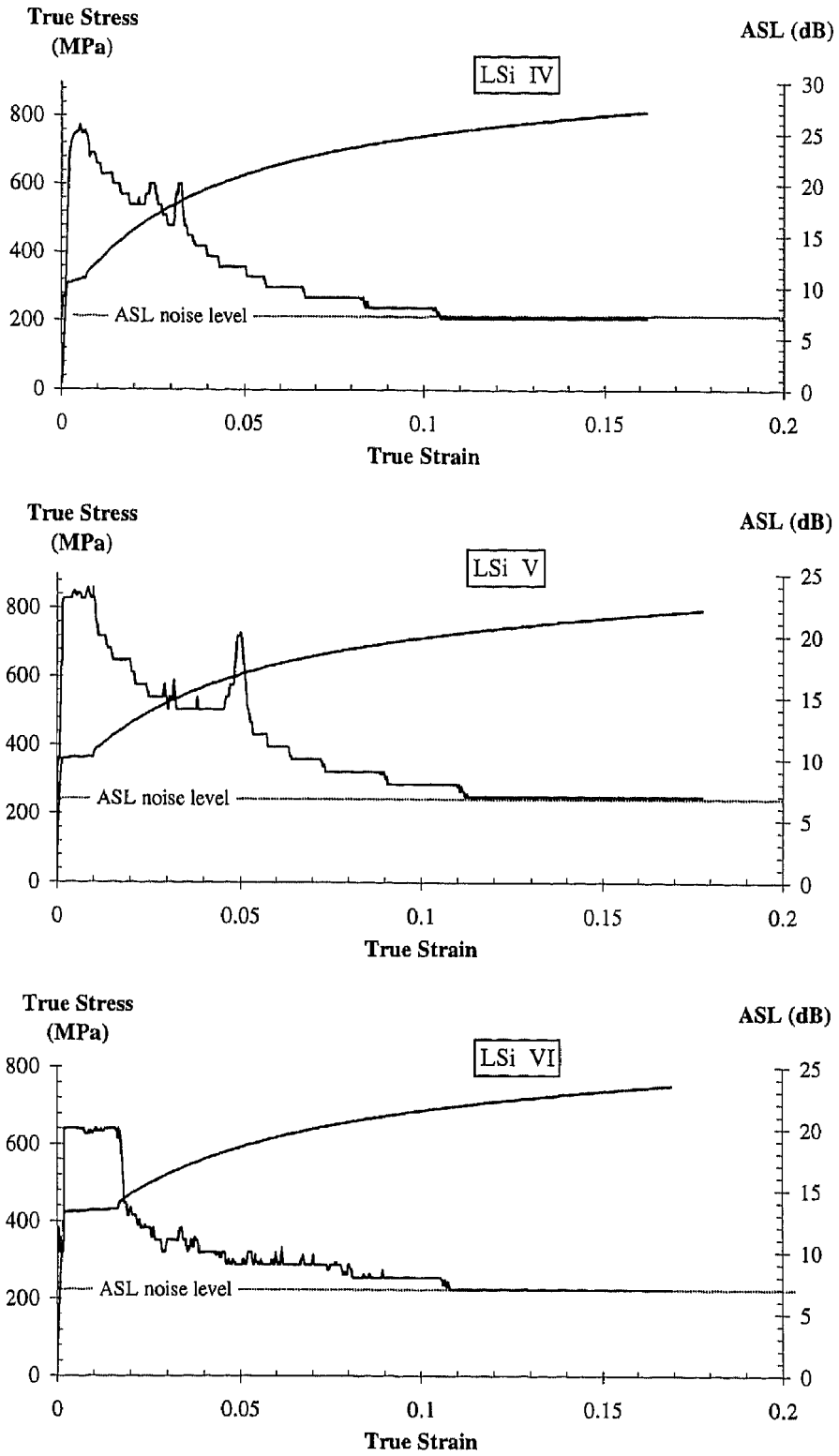

Figure 5.12: True stress – true strain and acoustic emission ASL curves for specimens IV, V, and VI of steel LSi.

4. Discussion

4.1 Mechanical Stability of Retained Austenite

Steels HSiI and LSi differ principally by their silicon contents. The heat-treatments have been chosen in such a way as to generate microstructures containing nearly the same amount of retained austenite. These microstructures however differ by the chemical composition of retained austenite, i.e. mainly by the carbon content, and the nature and volume fractions of the other phases (Table 5.3). These differences seem to influence in a large way the true stress – true strain curves (figure 5.4) and, particularly, the evolution of the incremental work-hardening exponents (figure 5.5).

It is often assumed [Tsuk91, Saku91b, Itam95] that the mechanical stability of retained austenite increases when its carbon content increases. As carbon is the best austenite stabiliser, a more carbon rich austenite has a lower M_s temperature so that the work to trigger martensitic transformation has to be increased. Mechanically-induced martensitic transformation therefore occurs later during straining. Figure 5.13 presents, for the 6 specimens of steels HSiI and LSi, the transformation rate of transformable austenite (expressed by the parameter n determined by the exponential fitting of figure 5.9) as a function of the carbon content of retained austenite. For the 3 specimens of steel HSiI, this figure shows that a linear correlation between the carbon content of retained austenite and its resistance to martensitic transformation can be established (unbroken line). In addition, other parameters of the microstructure also influence the stability of austenite. The 3 specimens of steel LSi differ only by the bainitic tempering time. The increasing carbon enrichment of retained austenite as the tempering time increases brings about a progressive decrease of the *thermal* martensite (i.e. the martensite formed during cooling). However, the absence of martensite at the expense of a carbon-richer austenite in specimen VI of steel LSi brings about a large increase of the transformation rate with respect to specimens IV and V. The presence of a small amount of martensite in specimens IV and V thus plays a favourable role on the mechanical stability of retained austenite. On comparison to the dotted line in figure 5.13 corresponding to similar microstructures consisting of ferrite, bainite and retained austenite exhibiting various levels of carbon, specimens IV and V present a reduced transformation rate. This indicates a *shielding effect* due to the high strength of martensite. The overall strength of the multiphase microstructure of these steels strongly depends on the strengths and volume fractions of the different phases present in the microstructure [Tomo82, Su87, Poech92]. The load transfer to the small volume fraction of high strength martensite in specimens IV and V effectively protects retained austenite from the external stress. As a consequence, despite a very low carbon content,

retained austenite in specimens IV and V exhibits an apparent mechanical stability that is comparable to that of specimen II of steel HSiI where austenite presents a much higher carbon content. This contribution to austenite mechanical stability disappears when martensite disappears from the microstructure (specimen VI). Presence of thermal martensite in the multiphase microstructure of the low silicon TRIP-aided steel has thus not only a strengthening effect (as presented in chapter IV) but also indirectly improves the mechanical stability of retained austenite and therefore the effectiveness of the TRIP effect. It can be anticipated that the other phases with their respective strengthening mechanisms, can also modify the apparent mechanical stability of retained austenite.

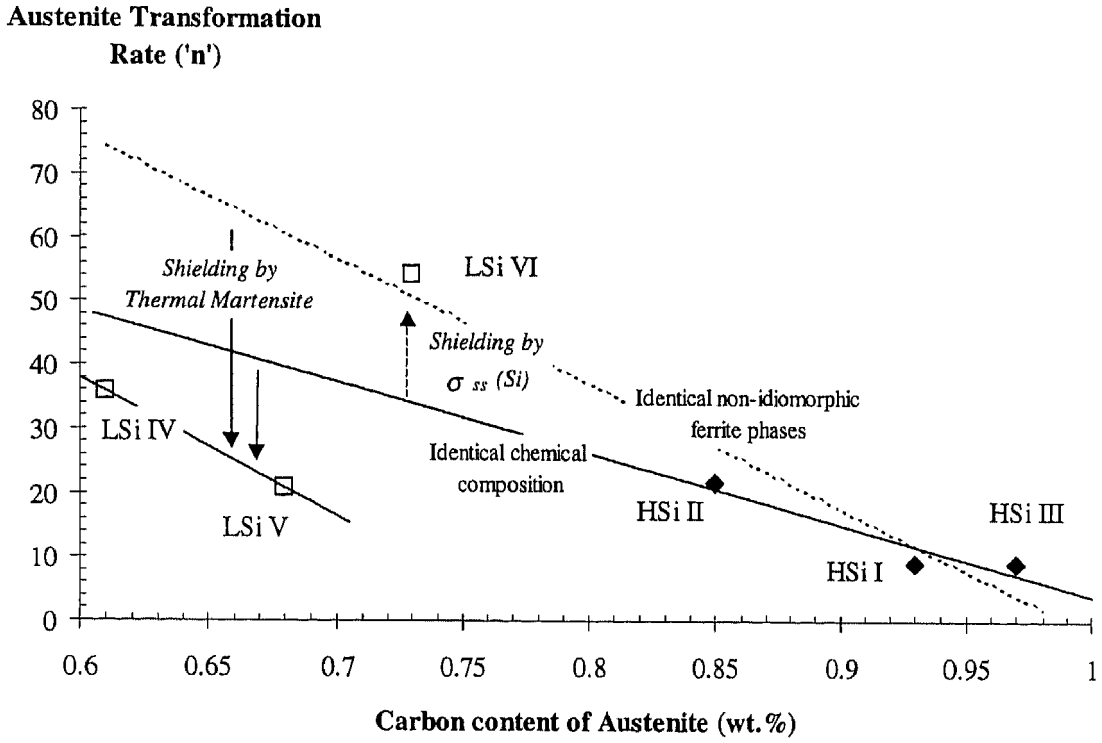

Figure 5.13: Transformation rate of austenite (expressed by the parameter 'n' of the exponential fitting) as a function of the carbon content of retained austenite of the specimens of steels HSiI and LSi (unbroken line: linear fitting of the 3 specimens of steel HSiI (identical chemical composition); dotted line: linear fitting of the 3 specimens of steel HSiI and specimen LSi VI (identical nature of the non-idiomorphic ferrite phases)).

Idiomorphic ferrite is always the major phase in TRIP-assisted multiphase steels. Hardly anything has been reported in the literature on the effect of the mechanical properties of ferrite [Sugi92]. Since the intercritical annealing time is too short to induce redistribution of substitutional elements (see chapter III), the ferrite matrix of the different specimens contains either 1.5 or 0.38 wt.% of silicon for steels HSiI or LSi, respectively. Silicon is known as a potent solid solution strengthening element of ferrite. Indeed, microindentation

hardness measurements presented in figure 5.6 show that the idiomorphic ferrite is harder in specimen I (steel HSiI) than in specimen VI (steel LSi). Steel LSi has a typical composition of cold-rolled Dual Phase steels and the hardness of its ferrite matrix is in good agreement with published results on Dual Phase steels [Mard77, Chen85]. The yield strength may be calculated from these hardness values by considering that, for a rigid-plastic material indented by a Vickers indenter, the yield strength is approximately 1/3 of the hardness ($\sigma_y \sim H_v/3$) [Mott56 Vand84]. This means that, due to the different solid solution strengthening by silicon, the ferrite of specimens of steel HSiI presents a yield strength higher by about 65 MPa than the ferrite of steel LSi. This experimental value is in good agreement with the solid solution strengthening effect of silicon predicted by Leslie [Lesl72], Sugden et.al [Sugd88] and Pickering et.al [Pick77, Pick92]. These authors propose a strengthening effect by silicon of the order of 100 MPa for 1wt.% of solute[2]. On the other hand, it seems that the solid solution strengthening effect of silicon in austenite is much smaller. Pickering [Pick78] and Aranzabal [Aran97] report a strengthening effect by silicon in austenite of the order of 20MPa for 1wt.% of solute. It can be therefore postulated that the higher strength of the ferrite matrix in specimens of steel HSiI could be sufficient to improve the mechanical stability of retained austenite. This could explain on figure 5.13 the difference observed at the carbon content of specimen VI between the unbroken line corresponding to specimens with a high silicon identical chemical composition and the dotted line corresponding to similar microstructures in low and high silicon steels. Many studies deal with the tuning of the amount and stability of retained austenite in TRIP-aided steels by changing the amount of silicon (from 1 to 2.5wt.%) [Tsuk91, Saku91b, Sugi92, Mats92]. None of these studies consider the solid solution strengthening effect of silicon. The stabilising effect ascribed to silicon [Tsuk91, Saku91b] could also partly result from the higher strength of the idiomorphic ferrite matrix with a higher silicon content.

Bainite in the TRIP-aided steels mainly influences the morphology of retained austenite and as a consequence, the proportion of austenite not transformed at the onset of necking. Indeed, it has been shown in figure 5.8 that 40 to 50% of the initial amount of retained austenite of the 3 specimens of steel HSiI remains untransformed at the onset of necking. Figure 5.14 presents typical micrographs of specimens of steel HSiI strained up to the onset of necking. This figure shows that the untransformed austenite corresponds to the

[2] Recognising that solid-solution strengthening by silicon can play a role on the strength of ferrite, it is also worth noting that steel LSi contains a small amount of niobium (Table 5.1) (added for easier control of the industrial hot-rolling process) that improves the strength of ferrite. Indeed, observations by TEM have shown that niobium carbo-nitrides are present in the idiomorphic ferrite matrix of specimens of steel LSi so that this ferrite is precipitation strengthened. Without these precipitates, ferrite of steel LSi should be still softer as predicted by the previous authors.

interlath film associated with bainitic ferrite (the film type). As already observed by Chung et.al., Sugimoto et.al. [Sugi93] and Itami et.al [Itam94], this film type of austenite located between bainitic ferrite laths cannot easily transform during straining. Owing to the small size of the bainitic ferrite laths, bainite also allows a 'shielding' effect of this film type of austenite. Furthermore, as shown in chapter III, the carbon enrichment of austenite along the broad face of the bainitic ferrite platelets is the highest. In specimens of steel LSi, this film type of austenite may be less present since the carbide precipitation occurring during the bainitic tempering (demonstrated in chapter III) will take place preferentially in the carbon richer region, i.e. between the bainitic ferrite platelets. However, as shown in figure 5.15, specimens of steel LSi present a different 'isolated' type of retained austenite that also remains untransformed at the onset of necking. This isolated type of austenite corresponds to the austenite dispersed within idiomorphic ferrite grains. As already reported [Jac98b], this intragranular austenite formed during the intercritical annealing of cold-rolled pearlite colonies. In these colonies, austenite nucleates on fine cementite particles resulting from the spheroidisation of the deformed pearlite. This intragranular retained austenite does not transform during straining because of a high manganese content [Cai85] and of a size stabilising effect [Kins77]. The untransformed part of retained austenite at the onset of necking in steels HSiI and LSi is thus linked to the proportions of bainite and intragranularly dispersed austenite. As a consequence, only the blocky type of austenite contributes to the TRIP effect[3].

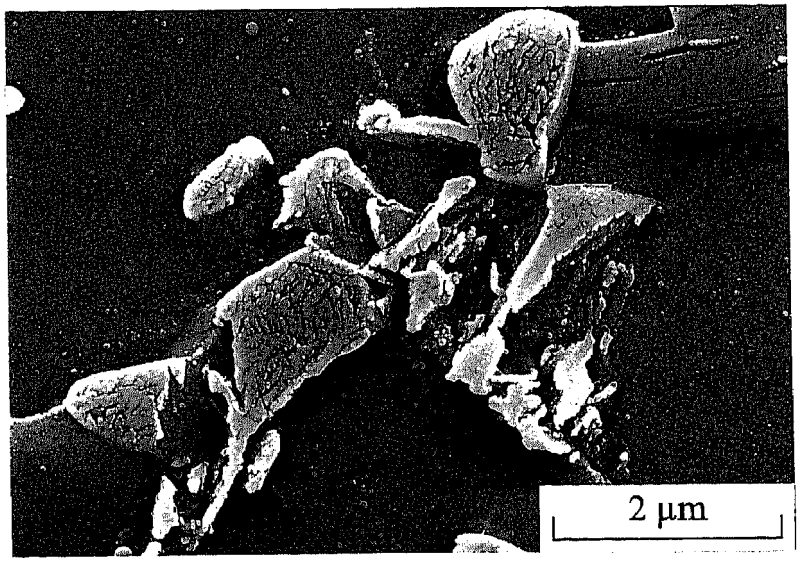

(a)

[3] This distinction between blocky type and film type of retained austenite will be also established on the basis of an energetical criterion in chapter VII dealing with the fracture controlling processes and toughness properties of TRIP-assisted multiphase steels.

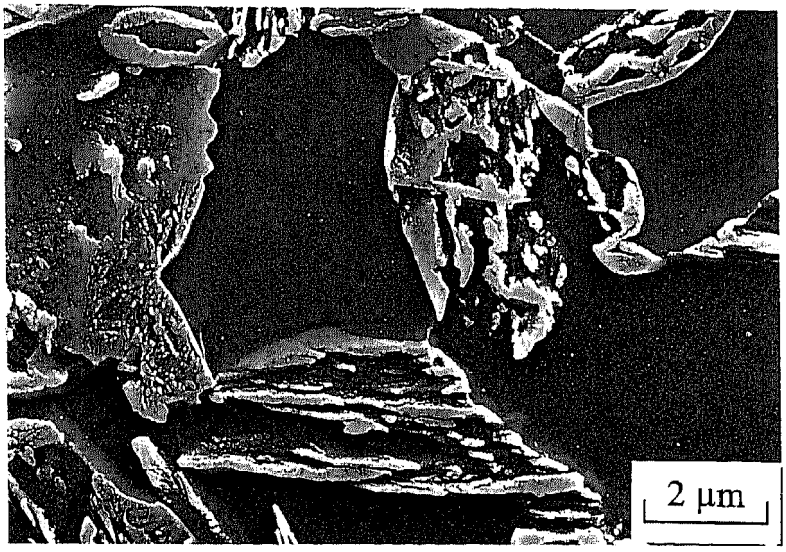

(b)

Figure 5.14: SEM micrographs of not transformed retained austenite associated with bainite in the case of specimens I and II of steel HSiI after tensile testing up to true uniform strain.

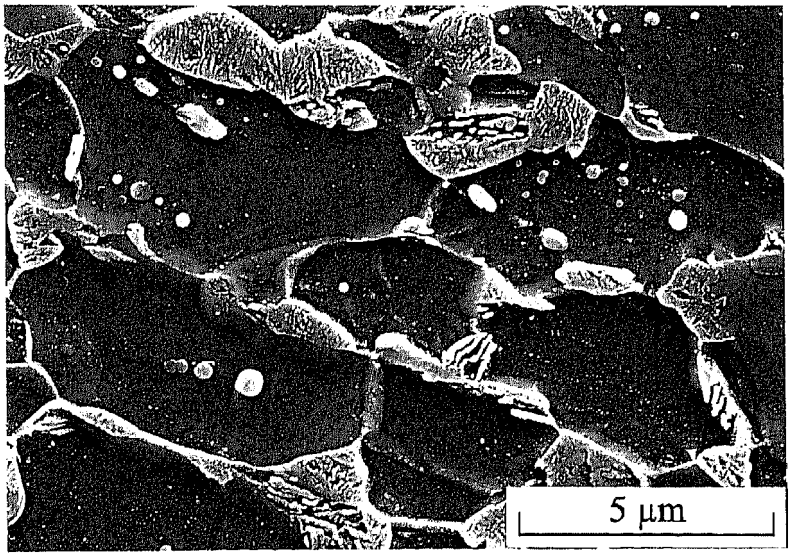

Figure 5.15: SEM micrograph of specimen V of steel LSi after tensile testing up to true uniform strain.

Once austenite begins to transform during plastic straining, the mechanical properties resulting from the interactions of the phases constituting the microstructure are also influenced by the growing volume fraction of martensite. The martensitic transformation influences the stress-strain behaviour both through the generation of free dislocations in ferrite and through the formation of a hard phase. As for Dual Phase steels, it can be postulated that the volume and shape changes accompanying the austenite to martensite transformation bring about plastic deformation of the surrounding ferrite and therefore

yields to an increase of the dislocation density [Furu79, Rigs79, Rizk82, Bour83]. In contrast to the fully austenitic TRIP steels, no selection of favourably oriented variants of martensite during stress-assisted transformation has ever been reported for the TRIP-aided steels. Anyway, the effect on the mechanical properties could not be explained by the stress-assisted transformation of the very small volume fraction of retained austenite involved in these steels. In the case of Dual Phase steels, dislocation strengthening results from the dislocations generated during quenching to room temperature. For TRIP-aided steels, the dislocation strengthening of ferrite can be distributed all over the plastic straining. As sometimes reported [Moyer75, Saka83], the extent of deformed ferrite is related to the difference of specific volumes of austenite and martensite which is directly related to the carbon content of austenite. Furthermore, an increase of the carbon content of austenite strongly increases the strength of martensite [Tamu82, Young94]. This means that the carbon content of retained austenite not only determines in a large way its mechanical stability but also influences the effectiveness of the TRIP effect by determining the volume expansion and the strength of martensite.

As a consequence, the mechanically-induced martensitic transformation in specimens of steel HSiI with more carbon rich retained austenite is more effective and more uniformly distributed all along plastic straining. Work-hardening then increases progressively, which postpones the onset of necking. The TRIP effect induces the increment of hardening necessary in order to avoid reaching the instability criterion [Olson82b]. On the other hand, steel LSi presents improved mechanical properties in comparison to Dual Phase steels of similar composition because the strengthening effect of martensite evolves during the first stage of plastic straining rather than being completely fixed by the quenching. As shown in figures 5.4 and 5.9, the best mechanical properties (i.e. specimens I and III) are obtained when the martensitic transformation is the most progressive (even if a lower content of austenite is transformed). In contrast, specimens with a faster martensitic transformation (II and V) exhibit higher initial values of work-hardening (even higher for specimen V because of the free dislocations generated by the thermal martensite) but the hardening due to martensitic transformation levels off rapidly in such a way that high values of $n_{incr.}$ cannot be maintained and lower true uniform strains are therefore attained.

4.2 Martensitic Detection by Acoustic Emission

Acoustic emission is related to the generation and propagation of transient elastic waves in the microstructure caused by physical mechanisms accompanied by a rapid release of energy [Olson82b, Mohr86, Strin92]. The acoustic emission recorded during the tensile

testing of the different TRIP-aided specimens (figures 5.11 and 5.12) as well as during testing of ferrite-martensite and ferrite-bainite specimens (figure 5.10) is generated by 2 phenomena intervening in the plastic deformation process: dislocation motion and martensitic transformation.

The motion of a dislocation creates elastic waves due to the relaxation of the elastic stress field in the lattice (Peierls barrier). This process is considered as the basic mechanism by which dislocations can cause acoustic emission [Gill71]. However, since the motion of a single dislocation is unlikely to produce a detectable acoustic emission signal, it appears that acoustic emission from dislocation motion occurs only when many dislocations move simultaneously within a small volume of the deforming material. Furthermore, theoretical modelling of how dislocation motion can be related to the detection of elastic waves has demonstrated that the acoustic emission rate (i.e. the continuous emission amplitude since individual pulses are not resolvable [Hei83]) is not proportional to the total dislocation density or to the mobile dislocation density, but to the rate of change of the mobile dislocation density [Heip87a]. Together with this effect of avalanche of moving dislocations, the distance of glide of the dislocations and the velocity of motion have been proved to be key factors affecting the acoustic emission due to dislocation motion.

As a consequence, ferrite-martensite and ferrite-bainite specimens of steel LSi exhibit a typical evolution of the continuous acoustic emission with true strain, with peak values at the onset of yielding. For the ferrite-bainite microstructure, the high ASL is confined during the Lüders plateau (Figure 5.10(b)). This phenomenon results from the sudden breakaway of many dislocations from solute pinning atmospheres. Once Lüders bands have propagated through the whole specimen, the samples enter the work-hardening region. The acoustic emission is then drastically lowered and further decreases with plastic strain. As deformation proceeds, the density of obstacles to the glide of the dislocations increases. These obstacles, such as dislocation forest and tangles, progressively reduce the distance the dislocations move and thereby reduce the size of the generated elastic waves until most of the moves become undetectable. The same evolution is observed for the ferrite-martensite specimen. Despite the continuous yielding behaviour exhibited by ferrite-martensite microstructure, the motion of the high density of dislocations generated in ferrite by the martensite formed on quenching [Furu79, Rigs79] brings about a high ASL. The further decrease of ASL with increasing strain can then also be related to the decrease of the rate of change of the mobile dislocation density and to the increasing number of obstacles to dislocation motion.

In comparison to these 2 microstructures, specimens of both steels HSiI and LSi containing retained austenite that martensitically transformed during straining exhibit different evolutions of ASL with true strain. These particular evolutions can be related to the transformation rate of austenite so that acoustic emission appears to be a sensitive technique for dynamically monitoring the martensitic transformation of retained austenite and therefore austenite mechanical stability. In a similar way as mechanical twinning [Heip87b], martensitic transformation generates acoustic emission due to the rapid shear deformation associated with the displacive growth of martensite plates [Spei71].

Figures 5.16 and 5.17 present, for each specimen of steels HSiI and LSi, the true stress – true strain curves together with the ASL level. The 2 vertical lines indicate the true strains corresponding to transformation levels of 25% and 75% of the transformable austenite. As already reported by Tseng et.al. [Tseng87], sustained acoustic activity beyond the onset of yielding can be easily correlated to the transformation of retained austenite.

For steel HSiI, specimen II with a faster transformation of austenite through plastic straining also presents a high acoustic activity confined in the first part of normalised true strain. On the contrary, specimens I and III maintain, after the ASL peak corresponding to the Lüders plateau, a lower acoustic activity over a wider range like the lower rate of transformation. For steel LSi, acoustic activity is always confined in the first part true strain. However, a correlation with the transformation rate can also be observed. Specimens IV and VI present a fast decreasing acoustic activity while the slower martensitic transformation in specimen V ensures a higher ASL on a larger range of strain.

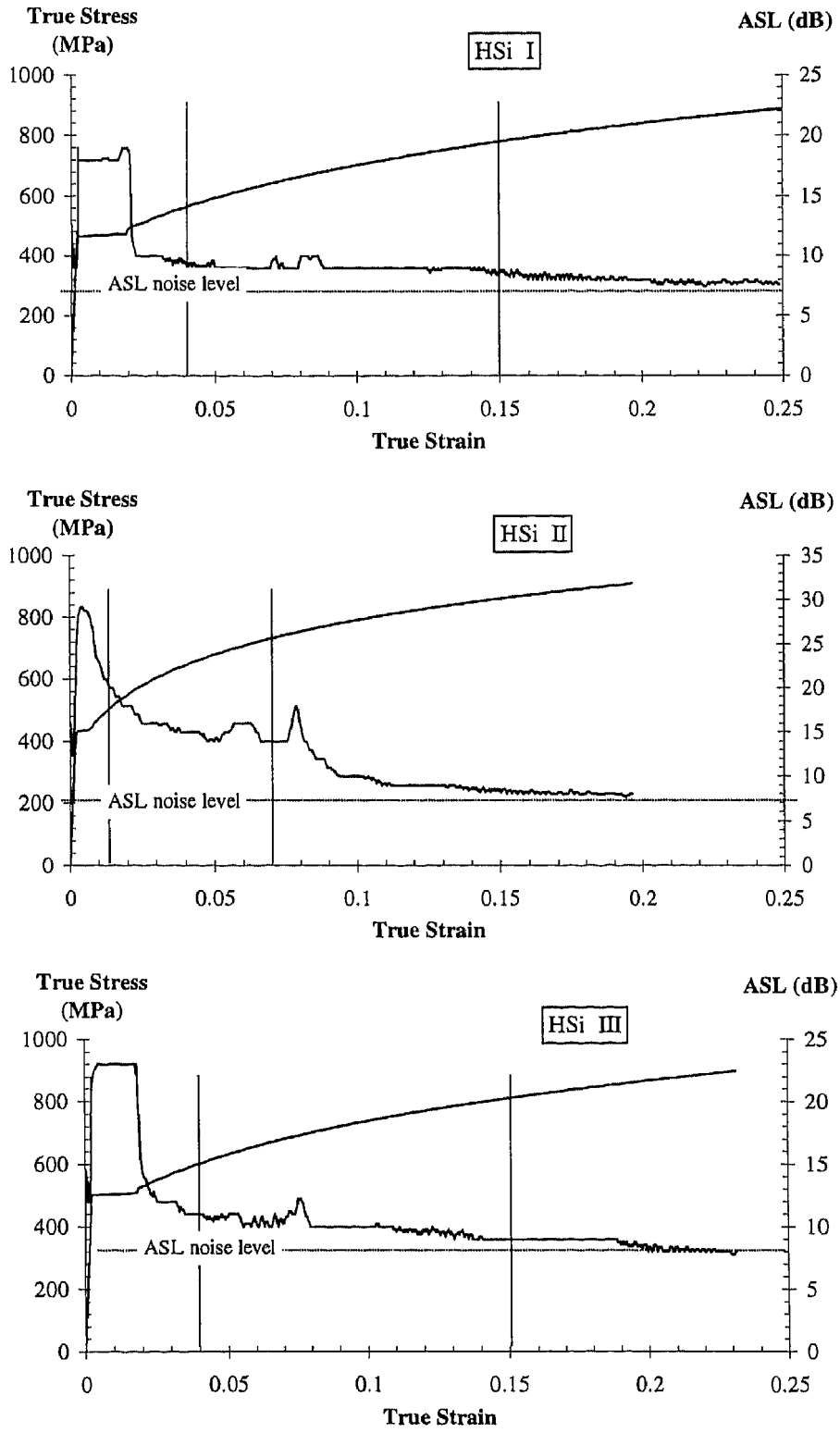

Figure 5.16: True stress – true strain curve and acoustic emission ASL curve for the 3 specimens of steel HSiI (the vertical lines indicate the true strains for which 25% and 75% of the transformable austenite has transformed).

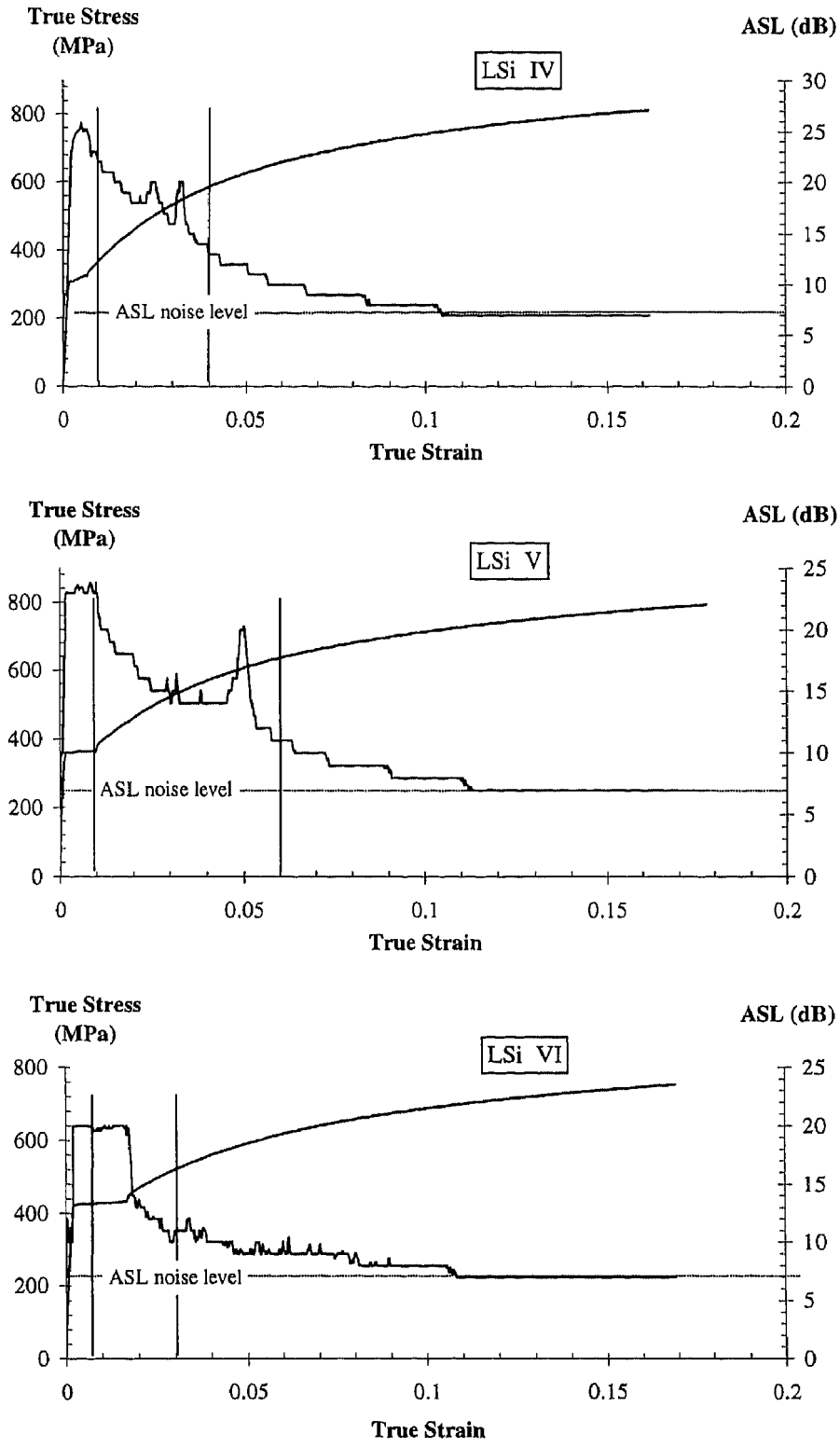

Figure 5.17: True stress – true strain curve and acoustic emission ASL curve for the 3 specimens of steel LSi (the vertical lines indicate the true strains for which 25% and 75% of the transformable austenite has transformed).

5. Conclusion

This chapter has elucidated the factors contributing to the mechanical stability of austenite retained as a dispersed phase in 2 TRIP-assisted multiphase steels differing by their silicon content. Different specimens were considered for which the initial retained austenite content was identical. It was shown that mechanical properties result from interactions between the different phases. When austenite is a dispersed phase in a multiphase microstructure, its mechanical stability depends on the intrinsic effect of loading on martensitic transformation, but also on the influence of the other phases. The resulting 'apparent' stability of retained austenite will thus depend not only of austenite parameters but also of the other interacting phases. Next chapter will show that the 'intrinsic' mechanical stability of retained austenite can be characterised by considering the temperature dependence of the mechanical properties.

In the case of the low silicon steel LSi, the thermal martensite formed during cooling to room temperature was shown to constitute an effective load carrier in such a way that martensite exerts a *shielding effect* protecting austenite from the externally applied load. This effect somewhat compensates for the poor stability due to the low carbon enrichment. It may be postulated that the solid solution strengthening effect of silicon leads to an effective strengthening of the idiomorphic ferrite matrix and thus also to a shielding effect. Bainite was shown to influence the morphology of retained austenite and so the amount of austenite transformed before the onset of necking. As a consequence, description of the mechanical stability of retained austenite has to take into account in a much larger way than previously carried out in the literature the potential effects of the surrounding matrix which can exhibit various mechanical properties.

Finally, this study has also shown that tensile testing of TRIP-assisted multiphase steels brings about an acoustic activity that has been related to the 2 mechanisms generating acoustic waves during straining, that is dislocation motion and martensitic transformation. Continuous acoustic activity was therefore related to the transformation rate of austenite and it was concluded that acoustic emission could be used for dynamic monitoring of the TRIP effect during straining.

References

[Ang54] T. Angel: *J. Iron and Steel Inst.*, 1954, pp. 165-174

[Aran97] J. Aranzabal, I. Gutierrez, J.M. Rodriguez-Ibabe, and J.J. Urcola: *Metall. Trans. A*, 1997, vol. 28A, pp. 1143-1156

[Bhad83] H.K.D.H. Bhadeshia, and D.V. Edmonds: *Metal Sc.*, 1983, vol. 17, pp. 411-419

[Bhan72] D. Bhandarkar, V.F. Zackay, and E.R. Parker: *Metall. Trans.*, 1972, vol. 3, pp. 2619-2631

[Bour83] D.L. Bourell, and A. Rizk: *Acta Metall.*, 1983, vol. 31(4), pp. 609-617

[Cai85] X.-L. Cai, A.J. Garratt-Reed, and W.S. Owen: *Metall. Trans. A*, 1985, vol. 16A, pp. 543-557

[Chan71] G.R. Chanani, V.F. Zackay, and E.R. Parker: *Metall. Trans.*, 1971, vol. 2, pp. 133-139

[Chen85] Q.A. Chen, R. Kaspar, and O. Pawelski: *Z. Metallkde*, 1985, vol. 76, pp. 348-352

[Dyso70] D.J. Dyson, and B. Holmes: *J. Iron Steel Inst.*, 1970, vol. 208, pp. 469-474

[Fahr71] D. Fahr: *Metall. Trans.*, 1971, vol. 2, pp. 1883-1892

[Furu79] T. Furukawa, H. Morikawa, H. Takechi, and K. Koyama: *Proc. Conf. Structure and Properties of Dual Phase Steels*, R.A. Kot and J.W. Morris ed., TMS-AIME, Warrendale, PA, 1979, pp. 281-303

[Gill71] P.P. Gillis: *Proc. Symp. on Acoustic Emission*, R.G. Liptai, ASTM, 1971, pp. 20-29

[Green65] G.W. Greenwood, and R.H. Johnson: *Proc. Roy. Soc. London, Ser. A*, 1965, vol. 283, pp. 403-422

[Haid87] G.N. Haidemenopoulos, G.B. Olson, and M. Cohen: *Proc. 34th Sagamore Army Materials Research Conf.*, Lake George, New York, 1987, pp. 549-593

[Haid88] G. Haidemenopoulos: PhD thesis, MIT, 1988

[Heip83] C.R. Heiple, and S.H. Carpenter: *Acoustic Emission*, J.R. Matthews ed., Gordon and Breach Sc. Publ., 1983, pp. 15-104

[Heip87a] C.R. Heiple, and S.H. Carpenter: *J. Acous. Em.*, 1987, vol. 6, pp. 177-204

[Heip87b] C.R. Heiple, and S.H. Carpenter: *J. Acous. Em.*, 1987, vol. 6, pp. 215-236

[Itam94] A. Itami, M. Takahashi, and K. Ushioda: *Proc. Symp. High-Strength Steels for Automotive Industry*, C.E. Slater, Baltimore, MD, 1994, 245-254

[Itam95] A. Itami, M. Takahashi, and K. Ushioda: *ISIJ Int.*, 1995, vol. 35, pp. 1121-1127

[Jac98a] P. Jacques, K. Eberle, Ph. Harlet, and F. Delannay: *Proc. 40th Mechanical Working and Steel Processing Conference*, Pittsburgh, PA, October 25-28, 1998, ISS, Warrendale PA, pp. 239-250

[Jac98b] P. Jacques, X. Cornet, Ph. Harlet, J. Ladrière, and F. Delannay: *Metall. Trans. A*, 1998, vol. 29A, pp. 2383-2393

[Kins77] K.R. Kinsman, G. Das, and R.F. Hehemann: *Acta Metall.*, 1977, vol. 25, pp. 359-365

[Lebl89] J.B. Leblond, J. Devaux, and J.C. Devaux: *Int. J. Plasticity*, 1989, vol. 5, pp. 551-572

[Lesl72] W.C. Leslie: *Metall. Trans.*, 1972, vol. 3, pp. 5-26

[Lud69] D.C. Ludwigson, and J.A. Berger: *J. Iron and Steel Inst.*, 1969, pp. 63-69

[Magee68] C.L. Magee, and H.W. Paxton: *Trans. Metall. Soc. AIME*, 1968, vol. 242, pp. 1741-1749

[Mard77] A.R. Marder: *Formable HSLA and Dual-Phase Steels*, A.T. Davenport ed., TMS-AIME, Warrendale, PA, 1977, pp. 87-98

[Mark95] F. Marketz, and F.D. Fischer: *Metall. Trans. A*, 1995, vol. 26A, pp. 267-278

[Mats87] O. Matsumura, Y. Sakuma, and H. Takechi: *Scripta Metall.*, 1987, vol. 21, pp. 1301-1306

[Mats92] O. Matsumura, Y. Sakuma, Y. Ishii, and J. Zhao: *ISIJ Int.*, 1992, vol. 32, pp. 1110-1116

[Miih87] V.T.T. Miihkinen, and D.V. Edmonds: *Mater. Sc. Technol.*, 1987, vol. 3, pp. 441-449

[Mohr86] J. Mohr, and A.K. Mukherjee: *J. Acous. Em.*, 1986, vol. 5, pp. 162-170

[Moor95] V. Moorthy, T. Jayakumar, and B. Raj: *Int. J Ves. & Piping*, 1995, vol. 64, pp. 161-168

[Mott56] B.W. Mott: *Micro-Indentation Hardness Testing*, Butterworths Sc. Publ., London, 1956, pp. 1-15

[Moyer75] J.M. Moyer, and G.S. Ansell: *Metall. Trans. A*, 1975, vol. 6A, pp. 1785-1791

[Olson75] G.B. Olson, and M. Cohen: *Metall. Trans. A*, 1975, vol. 6A, pp. 791-795

[Olson78] G.B. Olson, and M. Azrin: *Metall. Trans. A*, 1978, vol. 9A, pp. 713-721

[Olson82a] G.B. Olson, and M. Cohen: *Metall. Trans. A*, 1982, vol. 13A, pp. 1907-1914

[Olson82b] G.B. Olson: *Deformation, processing and structures*, G. Krauss, ed. ASM, 1982, pp.391-424

[Ono76] H. Onodera, H. Goto, and I. Tamura: *Proc. 1st JIM Int. Symp. New Aspects of Martensitic Transformations*, Kobe, Japan, 1976, pp. 327-338

[Pat53] J.R. Patel, and M. Cohen: *Acta Metall.*, 1953, vol. 1, pp. 531-538

[Pick77] F.B. Pickering: *Hardenability Concepts with Applications to Steel*, DV. Doane and J.S. Kirkaldy eds, TMS-AIME, Warrendale, PA, 1977, pp. 179-225

[Pick78] F.B. Pickering: *Physical metallurgy and the design of steels*, Applied Science Publishers, London, 1978

[Pick92] F.B. Pickering: *Materials Science and technology – Vol. 7: Constitution and Properties of Steels*, F.B. Pickering ed., VCH Publ., Weinheim, 1992, pp. 41-94

[Poech92] M.H. Poech, and H.F. Fischmeister: *Acta Metall.*, 1992, vol. 40(3), pp. 487-494

[Rigs79] J.M. Rigsbee, J.K. Abraham, A.T. Davenport, J.E. Franklin, and J.W. Pickens: *Proc. Conf. Structure and Properties of Dual Phase Steels*, R.A. Kot and J.W. Morris ed., TMS-AIME, Warrendale, PA, 1979, pp. 304-329

[Rizk82] A. Rizk, and D.L. Bourell: *Scripta Metall.*, 1982, vol. 16, pp. 1321-1324

[Saka83] T. Sakaki, K. Sugimoto, and T. Fukuzato: *Acta Metall.*, 1983, vol. 31(10), pp. 1737-1746

[Saku91a] Y. Sakuma, O. Matsumura, and O. Akisue: *ISIJ Int.*, 1991, vol. 31, pp. 1348-1353

[Saku91b] Y. Sakuma, O. Matsumura, and H. Takechi: *Metall. Trans. A*, 1991, vol. 22A, pp. 489-498

[Saku92a] Y. Sakuma, D.K. Matlock, and G. Krauss: *Metall. Trans. A*, 1992, vol. 23A, pp. 1221-1232

[Saku92b] Y. Sakuma, D.K. Matlock, and G. Krauss: *Metall. Trans. A*, 1992, vol. 23A, pp. 1233-1241

[Sand81] B.P.J. Sandvik, and H.P. Nevalainen: *Met. Technol.*, 1981, pp. 213-220

[Spei71] G.R. Speich, and R.M. Fisher: *Proc. Symp. on Acoustic Emission*, R.G. Liptai, ASTM, 1971, pp. 140-151

[Strin92] R.G. Stringfellow, D.M. Parks, and G.B. Olson: *Acta Metall. Mater.*, 1992, vol. 40(7), pp. 1703-1716

[Su87] Y.L. Su, and J. Gurland: *Mater. Sc. Eng.*, 1987, vol. 95, pp. 151-165

[Sugd88] A.A.B. Sugden, and H.K.D.H. Bhadeshia: *Metall. Trans. A*, 1988, vol. 19A, pp. 1597-1602

[Sugi92] K. Sugimoto, N. Usui, M. Kobayashi, and S. Hashimoto: *ISIJ Int.*, 1992, vol. 32, pp. 1311-1318

[Sugi93] K. Sugimoto, M. Misu, M. Kobayashi, and H. Shirasawa: *ISIJ Int.*, 1993, vol. 33, pp. 775-782

[Taka80] K. Takashima, Y. Higo, and S. Nunomura: *Scripta Metall.*, 1980, vol. 14, pp. 489-491

[Tamu82] I. Tamura: *Metal Sc.*, 1982, vol. 16, pp. 245-253

[Tamu92] I. Tamura, and C.M. Wayman: *Martensite*, G.B. Olson and W.S. Owen ed, ASM, 1992, pp. 227-242

[Tomi93] Y. Tomita, and T. Okawa: *Mater. Sc. Eng. A*, 1993, vol. 172, pp. 145-151

[Tomo82] Y. Tomota, and I. Tamura: *Trans. ISIJ*, 1982, vol. 22, pp. 665-677

[Tseng87] D. Tseng, Q.Y. Long, and K. Tangri: *Acta Metall.*, 1987, vol. 35(7), pp. 1887-1894

[Tsuk91] I. Tsukatani, S. Hashimoto, and T. Inoue: *ISIJ Int.*, 1991, vol. 31, pp. 992-1000

[Vand84] G.F. Vander Voort: *Metallography: Principles and Practice*, McGraw-Hill, 1984, pp. 334-383

[Yeo63] R.B.G. Yeo: *Trans. Metall. Soc. AIME*, 1963, vol. 227, pp. 884-890

[Young94] C.H. Young, and H.K.D.H. Bhadeshia: *Mater. Sci. Technol.*, 1994, vol. 10, pp. 209-214

[Zack67] V.F. Zackay, E.R. Parker, D. Fahr, and R. Busch: *Trans. Am. Soc. Met.*, 1967, vol. 60, pp. 252-259

[Zhu92] Z. Zhu, and Q.Y. Long: *Scripta Metall.*, 1992, vol. 26, pp. 1463-1468

Chapter VI

Mechanical Stability of Retained Austenite and Temperature Dependence of Tensile Properties

The mechanical stability of retained austenite in 2 TRIP-assisted multiphase steels differing by their silicon content has been characterised by considering the effect of temperature on the tensile stress – strain curves. As for fully austenitic TRIP steels and ultra-high strength steels, a reversal of the temperature dependence of flow stresses at small strain offset was observed at a particular temperature. This temperature M_s^{σ} delineates the temperature range where the onset of yielding (and the corresponding acoustic emission activity) results from the plastic deformation of austenite from the range where it results from martensitic transformation of austenite. This temperature M_s^{σ} also corresponds to a change of the evolution with temperature of other macroscopic properties such as true stress at maximum load or true uniform strain. It can also be correlated to the enrichment of austenite by carbon. This temperature dependence of the mechanical properties of the TRIP-assisted multiphase steels allows characterising the intrinsic mechanical stability of retained austenite independently of the influence of surrounding phases.

1. Introduction

The mechanical stability of both fully austenitic TRIP steels [Olson78, Olson82, Tamu82, Tamu92] and partly austenitic Ultrahigh Strength steels [Haid87, Haid89a, b] has been often studied by considering the effect of the testing temperature on austenite transformation under an external load. Indeed, temperature is a convenient variable for studying the propensity of austenite to transform into martensite. Such studies have allowed defining the temperature M_s^σ and have shown that mechanical properties such as strength, ductility or toughness reach an optimum at this particular temperature (see chapter I). When austenite is loaded at temperatures between M_s and M_s^σ, the mechanical driving force is sufficient to allow martensitic transformation to nucleate on the same sites as it would have done during simple cooling without any prior plastic deformation of austenite. Transformation is then said to be *stress-assisted* [Olson82, Tamu82]. At a temperature above M_s^σ, the mechanical driving force necessary for triggering martensitic transformation is high enough for the yield stress in austenite to be attained before martensitic transformation [Olson78, Tamu82, Haid89a]. In this *strain-induced* regime, austenite is first plastically deformed and work-hardening then allows martensitic transformation to be triggered. The temperature M_s^σ which defines the boundary between these 2 temperature regimes thus corresponds to a reversal of the temperature dependence of the flow stress [Olson78, Tamu92, Haid89a]. Since mechanical properties influenced by mechanically-induced martensitic transformation show an optimum at M_s^σ, this temperature has been adopted as pertinent parameter characterising the stability of retained austenite [Haid89a, b].

Several studies [Saku92, Sugi92a, b, Jeong93, Saku93, Sugi93] have considered the effect of the testing temperature on the stability of retained austenite, and consequently on the mechanical properties of the conventional high silicon TRIP-assisted multiphase steels. It is obvious that retained austenite stability increases with testing temperature (as shown in chapter I in Dual Phase steels). Increased stability is accompanied by the rapid disappearance of the TRIP effect: in TRIP-aided steels, almost no austenite was found to transform during straining at about 100°C [Saku92, Sugi92a, Jeong93, Saku93]. On the other hand, mechanical testing at low temperature leads to martensitic transformation of retained austenite at small plastic strain. As a consequence, tensile strength generally related to the volume fraction of martensite formed during mechanical testing, decreases when the testing temperature increases [Saku92, Jeong93, Saku93, Sugi93]. However, the influence of temperature on yield strength and elongation is not clear. No attempt of measurement of the temperature M_s^σ of retained austenite in TRIP-aided steels has been reported in the literature.

The mechanical stability of retained austenite at room temperature and the influence of this stability on the mechanical properties have been characterised in chapter V for steels HSiI and LSi differing by their silicon content. The steels had been intercritically annealed and bainitically transformed in such a way that the same amount of retained austenite (with different carbon contents) was generated. Chapter V showed that retained austenite exhibits an 'apparent' stability depending not only on austenite carbon content, but also on the interactions with other phases like thermal martensite and possibly ferrite. It was therefore concluded that the mechanical stability of retained austenite and the efficiency of the TRIP effect have to be considered together with the strengthening mechanisms of the other phases.

The purpose of the present chapter is to further characterise the mechanical stability of retained austenite and its influence on mechanical properties by considering the effect of temperature. We study the same 2 cold-rolled C-Mn-Si TRIP-assisted multiphase steels (i.e. HSiI and LSi) heat-treated in the same conditions as in chapter V. Particular emphasis focuses on steel LSi. It will be shown that a transition temperature corresponding to M_s^{σ} can be experimentally defined when considering the evolution with temperature of the onset of yielding or of other macroscopic mechanical properties. This transition temperature is shown to be correlated with a transition of the acoustic activity.

2. Experimental procedure

The 2 same steels as in chapter V, i.e. high silicon HSiI steel and low silicon LSi steel were investigated in this chapter. The chemical compositions of the 2 steels are reminded in Table 6.1. Table 6.2 presents the heat-treatment conditions of the 6 specimens together with the volume fractions of the different phases and the carbon content of retained austenite estimated from X-ray diffraction measurements. It is worth stressing the fact that each specimen contains nearly the same volume fraction of retained austenite (except for specimen VI of steel LSi for which the volume fraction is slightly smaller). The carbon content of retained austenite is variable. We will mainly focus on specimens V and VI of steel LSi for which the respective the room temperature mechanical stability of retained austenite does not scale with the respective carbon contents (see chapter V). Specimen V presents a temperature M_s higher than room temperature and therefore contains about 5 % of thermal martensite. For specimen VI, the higher carbon content of austenite has brought M_s just below room temperature. As shown in chapter V, specimens I and III of steel HSiI present a higher stability of retained austenite, whereas specimen II exhibits a transformation rate at room temperature similar to that of specimen V of steel LSi.

(10^{-3} wt.%)	C	Mn	Si	P	S	Cr	Ni	Cu	Nb	Al	N
HSiI	130	1420	1500	13	9	13	20	8	0	27	7.9
LSi	160	1300	380	13	12	19	27	19	13	30	6.3

Table 6.1: Chemical compositions (10^{-3} wt.%) of the investigated steels.

			Ferrite (F) (%)	Bainite (B) (%)	Retained Austenite ($V_{\gamma r}$) (%)	'Thermal' Martensite ($M_{therm.}$) (%)	Carbon content of Rγ (wt.%)
HSiI					± 0.5		
	I	760°C/2min/410°C/5min	~ 75	~ 15	8	0	0.93
	II	775°C/2min/360°C/5min	~ 60	~ 30	7.9	~ 0	0.85
	III	775°C/2min/410°C/5min	~ 60	~ 30	7.8	0	0.97
LSi							
	IV	730°C/5min/370°C/30s	~ 75	~ 9	8.8	~ 7	0.61
	V	730°C/5min/370°C/1min	~ 75	~ 12	8.1	~ 5	0.68
	VI	730°C/5min/370°C/3min	~ 75	~ 19	6.1	0	0.73

Table 6.2: Volume fractions of the different phases constituting the microstructure of each specimen of steels HSiI and LSi together with the carbon content of retained austenite estimated from lattice parameter.

The microstructures were studied by scanning electron microscopy (SEM) following the method described in chapter II. The evolution of the volume fraction of retained austenite after different extents of plastic straining was measured by Mössbauer spectroscopy

Isothermal tensile tests were performed at temperatures between –30°C and 120°C on tensile specimens prepared according to the European standard EN10002-1. The upper limit of the temperature range for this study corresponds to the beginning of dynamic strain aging which leads to inhomogeneous deformation (characterised by serrated flow) and therefore shows an extreme sensitivity to temperature and strain rate [Sach82, Sach83]. Tensile tests were carried out in a closed chamber resistively heated or cooled by expansion of pressurised CO_2. A thermocouple was spot-welded at the end of the calibrated zone of each specimen in order to monitor temperature during tensile testing. The chamber was set at the test temperature prior to mounting the sample on the grip in order to minimise (and to keep constant) the time of exposition of the specimens at each temperature.

Tensile tests were carried out at a crosshead speed of 2mm/min. The initial gauge length of the analogic extensometer was 25mm. Measured loads and elongations were converted to true stress – true strain curves. Yield strength (σ_y) was defined as the true stress corresponding to the Lüders deformation plateau. True stress at maximum load (σ_{TS}) and true uniform strain (ε_u) were also measured from the tensile curves. Flow stresses at different strain offsets prior to the Lüders plateau (from 1.10^{-4} to 4.10^{-4}) were measured from the true stress – true strain curves at each temperature by considering the intercepts of the stress-strain curves with straight lines parallel to the elastic zone.

Acoustic emission was also recorded during tensile testing. As during room temperature tests described in chapter V, the transducer with a bandwidth of 100-300 kHz and an operating temperature range of –65°C to 170°C was directly attached to the calibrated zone of the sample using a thin layer of high vacuum grease as coupling medium. The pre-amplifier gain was fixed at 40 dB and the Average Signal Level (ASL) was recorded. The background noise level was 7 dB at all temperatures.

3. Results

3.1. Onset of Yielding

The various behaviours at the onset of yielding are reflected on the flow stresses at different strain offsets calculated from the true stress – true strain curves by considering straight lines parallel to the elastic zone and shifted at zero stress from the corresponding strain offsets. Figure 6.1 presents the evolution with testing temperature of the flow stresses of specimen VI with strain offsets of 1 10^{-4}, 2 10^{-4} and 3 10^{-4} respectively as well as the true stress corresponding to the Lüders plateau and defined hereafter as the yield strength. Flow stresses increase when temperature decreases while the Lüders plateau arises at a rather constant true stress. The difference between the flow stresses at small strain offsets and the yield strength means that a transition zone can be found between the elastic zone and the Lüders plateau. This transition zone will be explicitly shown hereafter. No transition zone between the elastic zone and the yield point elongation can be observed around 60°C so that flow stresses at the different strain offsets then correspond to the Lüders plateau stress. Furthermore, the stress of the Lüders plateau decreases when temperature decreases below about 55°C. From room temperature and for lower temperatures, a small, rapidly rising difference between the flow stresses occurs while Lüders plateau continues to arise at lower stresses.

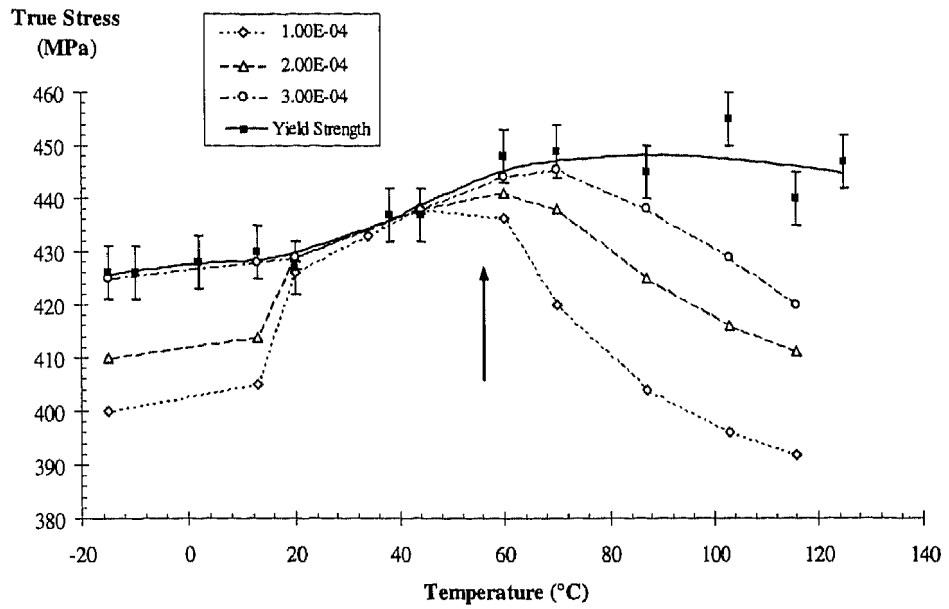

Figure 6.1: Evolution with testing temperature of flow stresses with strain offsets of 1 10^{-4}, 2 10^{-4} and 3 10^{-4} and yield strength of specimen VI.

The evolution as a function of testing temperature of flow stresses with strain offsets of 1 10^{-4}, 4 10^{-4} and 5 10^{-4} are presented in figure 6.2 for specimen V. In this case, the flow stress at 1 10^{-4} increases up to room temperature and remains constant at all temperatures above room temperature. On the other hand, the flow stress at 4 10^{-4} first increases when temperature decreases to around 80°C. It decreases thereafter for decreasing temperatures with a steeper decrease for temperatures lower than room temperature. It is noteworthy that this behaviour corresponds to the evolution of the stress of the Lüders plateau.

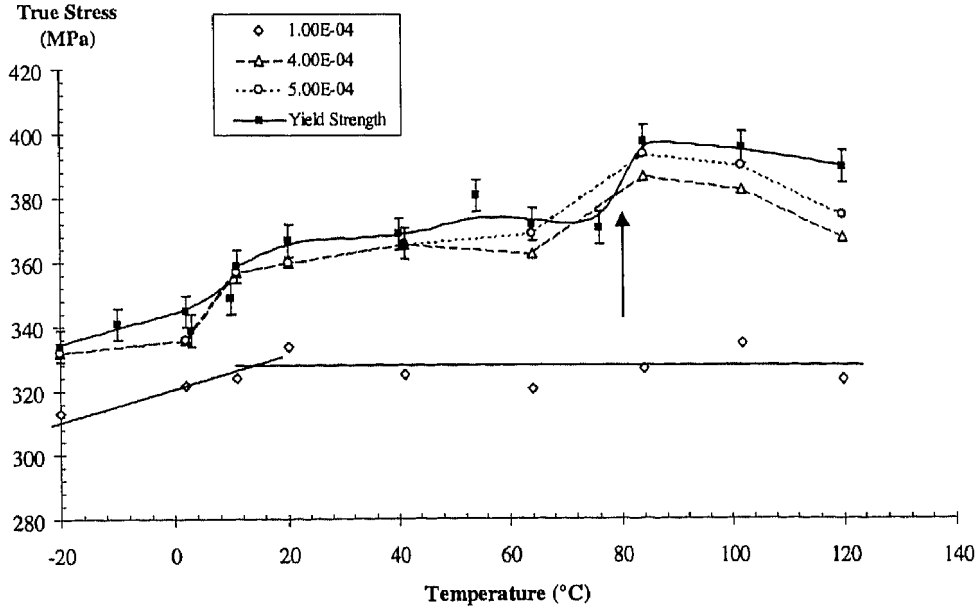

Figure 6.2: Evolution with testing temperature of flow stresses with strain offsets of 1 10^{-4} and 4 10^{-4} and yield strength of specimen V.

In order to interpret the behaviour of samples V and VI of steel LSi in the lower strain regions, samples of steel LSi consisting merely of ferrite-martensite or ferrite-bainite microstructures are first examined. The ferrite-martensite sample was obtained as in chapter V by water-quenching after intercritical annealing at the same temperature (730°C) and for the same time (5minutes) as for the other specimens of steel LSi. On the other hand, the ferrite-bainite sample was obtained at the end of a prolonged bainitic tempering (30 minutes) at 370°C. Figure 6.3 presents the low strain region of these 2 samples tested at room temperature, together with the acoustic activity. As well known, a ferrite-martensite sample (figure 6.3(a)) exhibits continuous yielding associated with a low yield strength. As shown in figure 6.3(a), this smooth transition from elastic deformation to plastic straining with a high work-hardening level is accompanied by a progressively increasing continuous acoustic emission up to a plateau. The ferrite-bainite microstructure exhibits a completely different behaviour at the onset of plastic deformation. This behaviour yields a particular acoustic signature. As shown in figure 6.3(b), a pronounced transition is observed between the linear elastic part and the beginning of the Lüders plateau. This abrupt elastic-plastic transition brings about a sharp transition of the acoustic activity at the onset of Lüders plateau from a low value (close to the noise level) to a high level during the Lüders plateau.

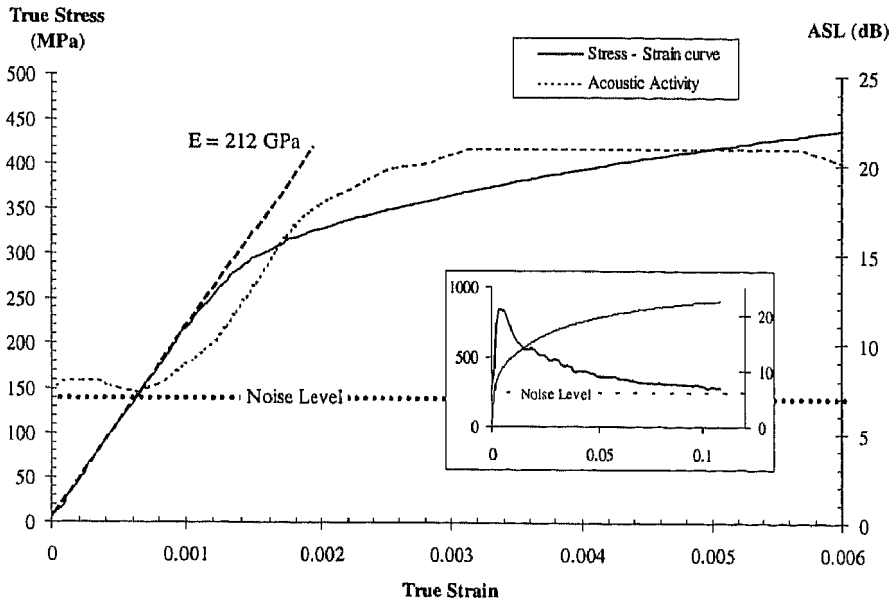

(a)

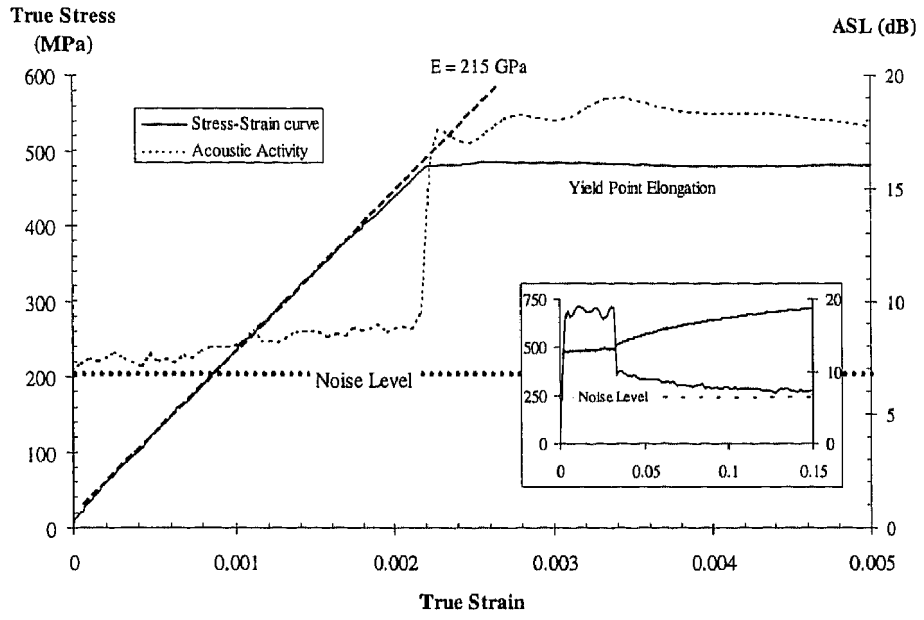

(b)

Figure 6.3: True stress – true strain curve and corresponding acoustic emission ASL of the onset of yielding for (a) ferrite-martensite and (b) ferrite-bainite microstructures of steel LSi.

Additional features can be observed when considering the elastic – plastic transition in tensile tests on specimens V and VI when temperature varies from –20°C to 120°C. Figure 6.4 presents the low strain region of specimen VI for testing temperatures of 103°C, 44°C, 22°C and 13°C respectively, together with the corresponding ASL curves. These temperatures represents the particular behaviour observed in different temperature regions. At the highest test temperature (103°C - figure 6.4(a)), a transition region separates the linear elastic zone and the yield point elongation of the Lüders plateau. The slope change at a strain of 1.75 10^{-3} observable in figure 6.4(a) is accompanied by a sharp jump of the ASL. Thereafter, the beginning of the Lüders deformation brings about a further increase of the acoustic activity. The width of this transition zone between the elastic zone and the Lüders plateau becomes smaller when the test temperature decreases and it completely disappears below about 60°C as represented in figure 6.4(b) which corresponds to a test temperature of 44°C. An abrupt transition from elastic deformation to yield point elongation can be observed as for the ferrite-bainite specimen. This transition also corresponds to a sudden increase of the ASL level. At room temperature (figure 6.4(c)) and at lower temperatures (figure 6.4(d)), a transition zone again appears between the elastic zone and the yield point elongation with a smooth decrease of the slope of the stress-strain relation to the flat Lüders plateau. As for the ferrite-martensite specimen, this smooth yielding gives rise to a monotonously increasing ASL level up to the value of the Lüders plateau.

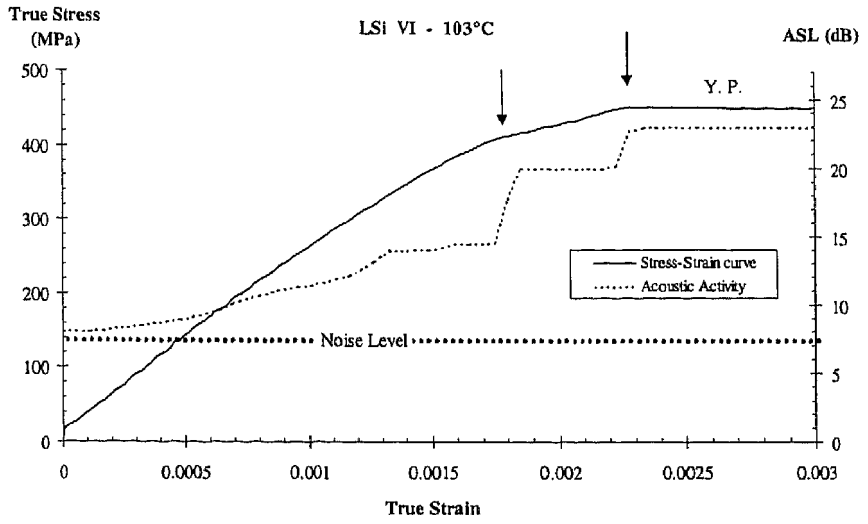
True Stress
(MPa)
LSi VI - 103°C
ASL (dB)
Y. P.
Stress-Strain curve
Acoustic Activity
Noise Level
True Strain

(a)

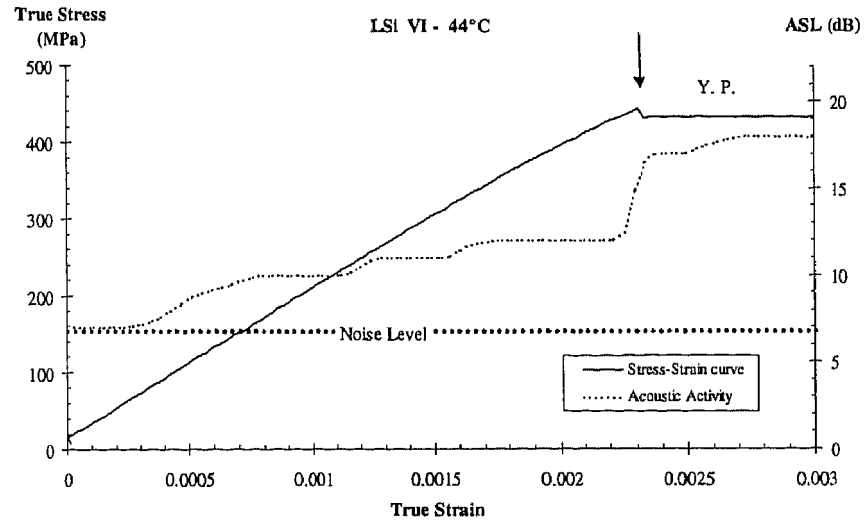
True Stress
(MPa)
LSi VI - 44°C
ASL (dB)
Y. P.
Stress-Strain curve
Acoustic Activity
Noise Level
True Strain

(b)

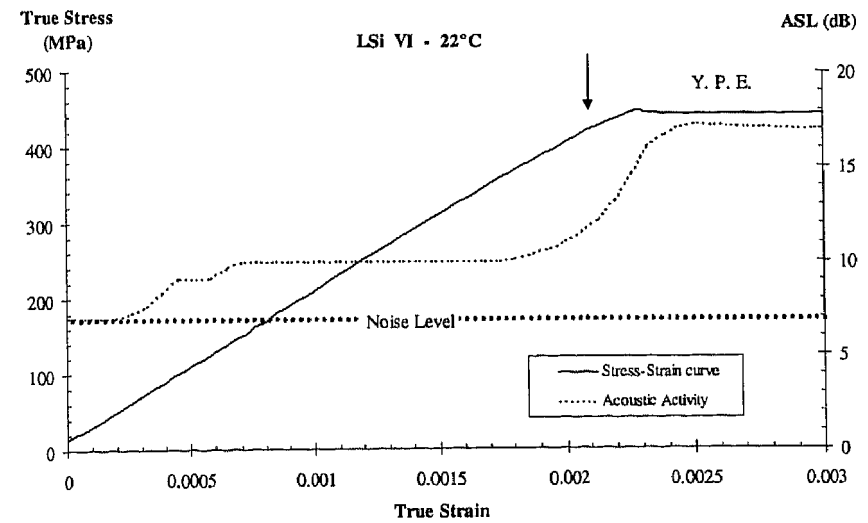
True Stress
(MPa)
LSi VI - 22°C
ASL (dB)
Y. P. E.
Stress-Strain curve
Acoustic Activity
Noise Level
True Strain

(c)

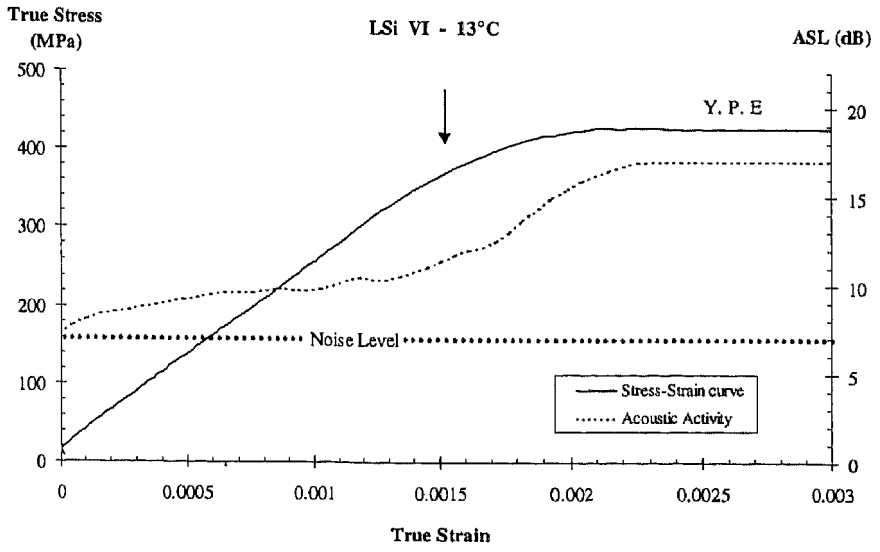

(d)

Figure 6.4: True stress – true strain curve and corresponding acoustic activity of the onset of yielding for specimen VI tested at (a) 103°C, (b) 44°C, (c) 22°C, and (d) 13°C.

As shown in figure 6.5, specimen V presents at all temperatures the yielding characteristics of both ferrite-martensite and ferrite-bainite microstructures. Indeed, it can be seen in figure 6.5(b) that the linear elastic zone is first followed by continuous yielding and then by a Lüders plateau. Furthermore, at temperatures higher than around 85°C (represented here by the behaviour at 102°C), a second transition zone is observed during continuous yielding. As shown in figure 6.5(a) (102°C), the beginning of this second transition zone is marked by an accident in the continuous yielding curve before the Lüders plateau. As for specimen VI, this transition is also marked by a steep rise of the ASL level. This transition zone progressively disappears when the testing temperature decreases and, as shown in figure 6.5(b), only continuous yielding and yield point elongation can be observed for temperatures lower than about 85°C. In this case, the ASL shows a monotonous increase from the onset of continuous yielding to the yield point elongation where it keeps a constant level. For lower testing temperatures, the same yielding behaviour is always observed (figure 6.5(c)).

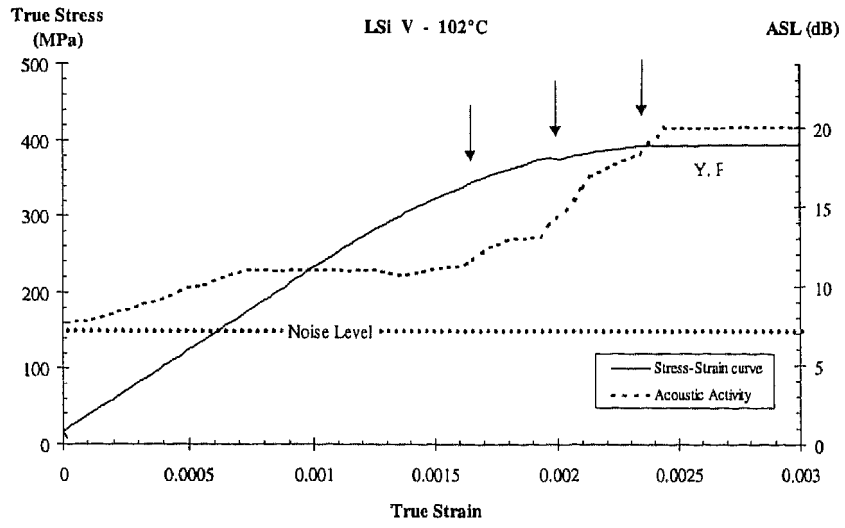

(a)

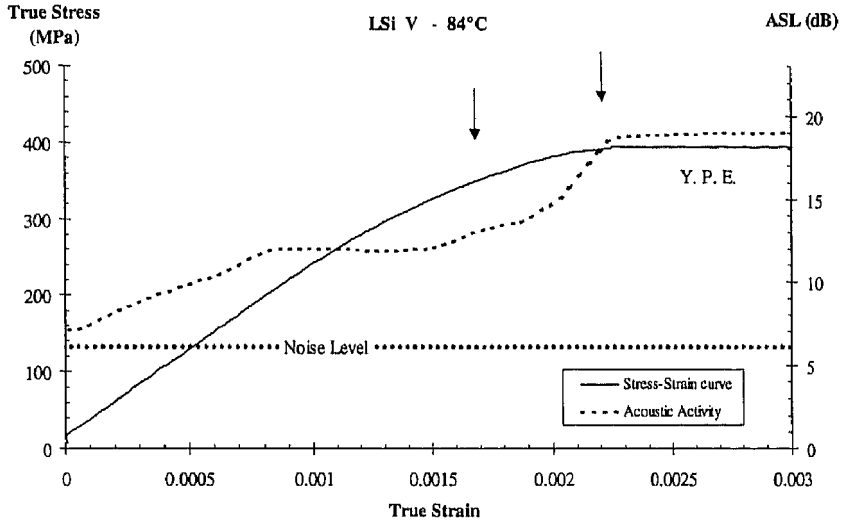

(b)

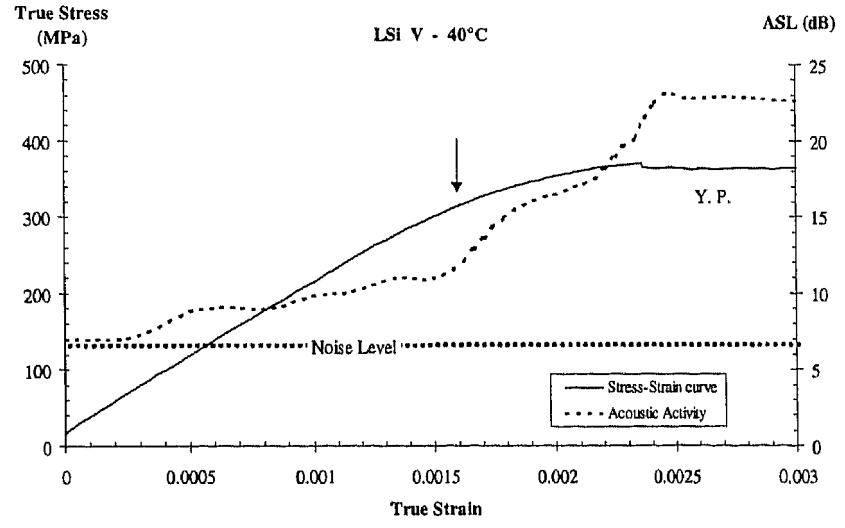

(c)

Figure 6.5: True stress – true strain curve and corresponding acoustic activity of the onset of yielding for specimen V tested at (a) 102°C, (b) 84°C, (c) 41°C.

3.2 Mechanical Properties

Figure 6.6 presents the variations of yield strength (σ_y), true stress at maximum load (σ_{TS}) and true uniform strain (ε_u) with testing temperature for specimens V and VI of steel LSi. Both specimens globally exhibit the same evolution of these 3 properties with temperature. Figure 6.6(a) shows that an increase of the testing temperature brings about an increase of the yield strength σ_y followed by a slow decrease beyond a certain transition temperature. A steeper increase of σ_y seems to occur just before the transition temperature. This transition, which is clearer for specimen V, is situated around 80°C for specimen V and around 55°C for specimen VI. On figure 6.6(b), it can be seen that the true stress at maximum load σ_{TS} shows an inverse trend than σ_y, i.e. a decrease for increasing temperature. It is noticed that a steeper decrease of σ_{TS} seems to occur around 80°C for specimen V and around 55°C for specimen VI, i.e. at the same transition temperature as for σ_y. As shown in figure 6.6(c), the evolution of the true uniform strain with temperature is less clear. ε_u seems first to increase for tensile tests carried out from sub-zero temperatures to room temperature. A high, rather constant true uniform strain is then maintained for temperatures ranging from 20°C to 65°C for specimen V and from 20°C to 45°C for specimen VI. ε_u thereafter exhibits somewhat lower values with a larger scatter (due to the beginning of the occurrence of dynamic strain aging). Nevertheless, it seems that the transition from high to low values of ε_u corresponds to about the same transition temperature as observed for σ_y and σ_{TS}.

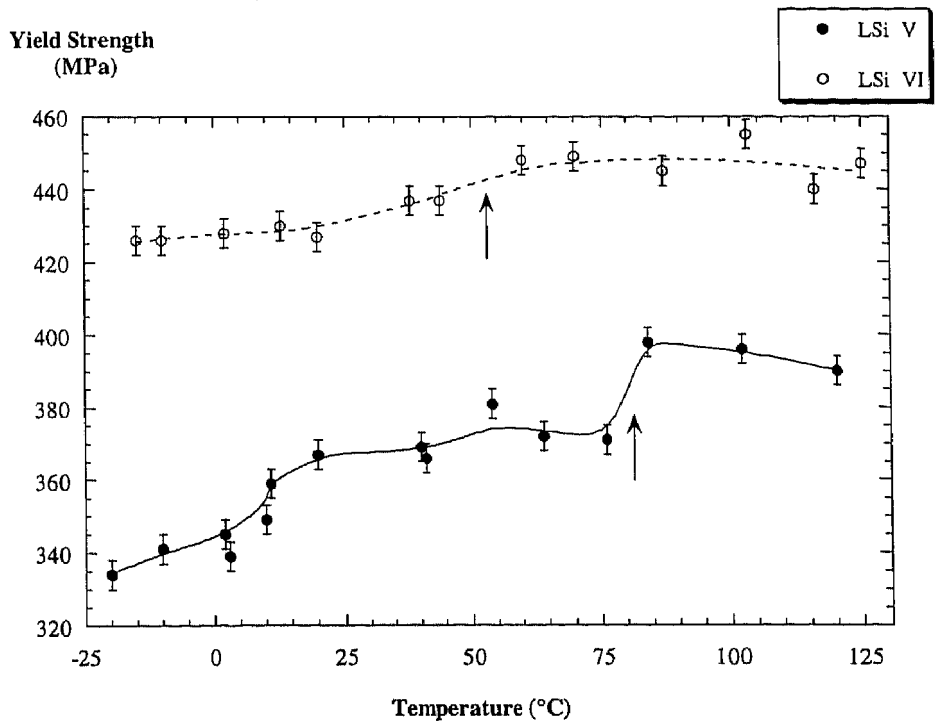

(a)

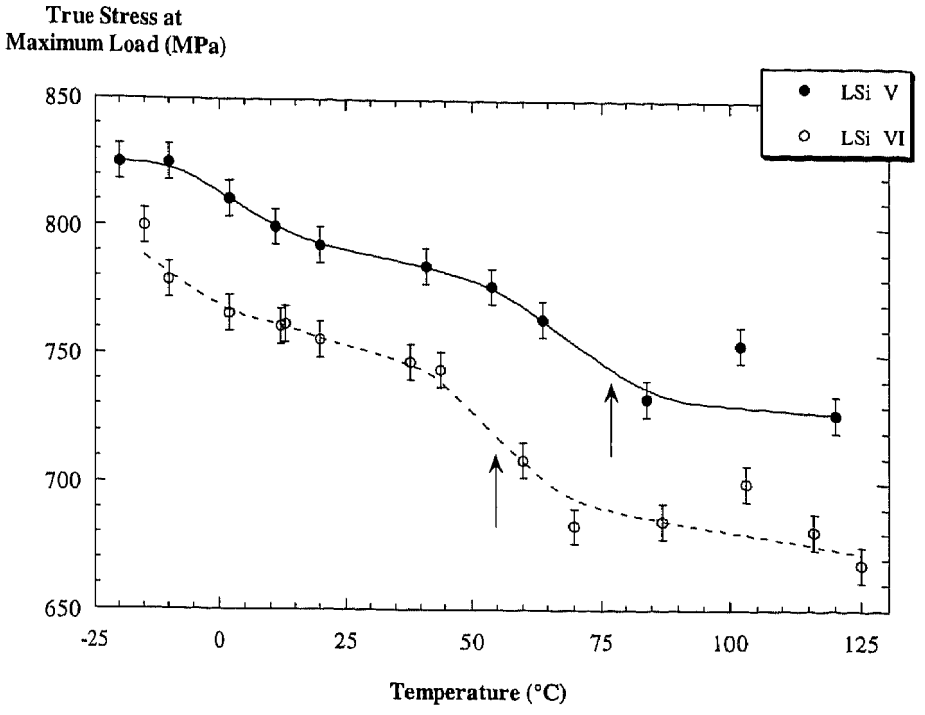

(b)

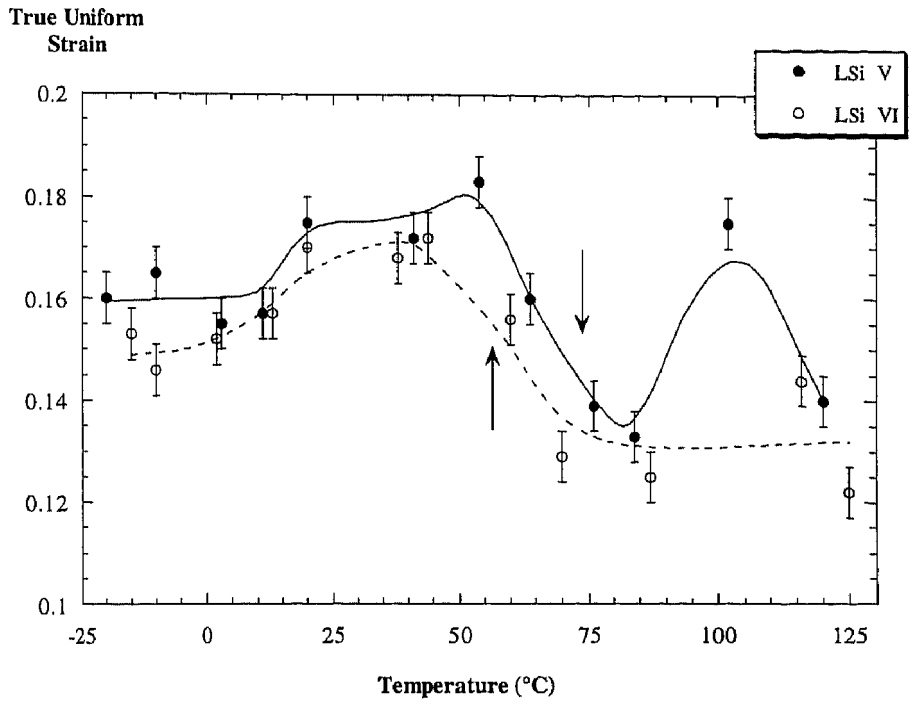

(c)

Figure 6.6: Evolution of (a) yield strength (corresponding to the Lüders plateau) (σ_y), (b) true stress at maximum load (σ_{TS}) and (c) true uniform strain (ε_u) as a function of temperature for specimens V and VI of steel LSi.

Figure 6.7 presents the evolution of the yield strength with testing temperature for the 3 specimens of steel HSiI. Whereas specimen II exhibits the same evolution as specimens V

and VI of steel LSi, i.e. a monotonous increase of σ_y with temperature up to a transition temperature around 40°C, followed by a decrease for higher temperatures, specimens I and III show a different evolution with a monotonous decrease of σ_y for increasing testing temperatures.

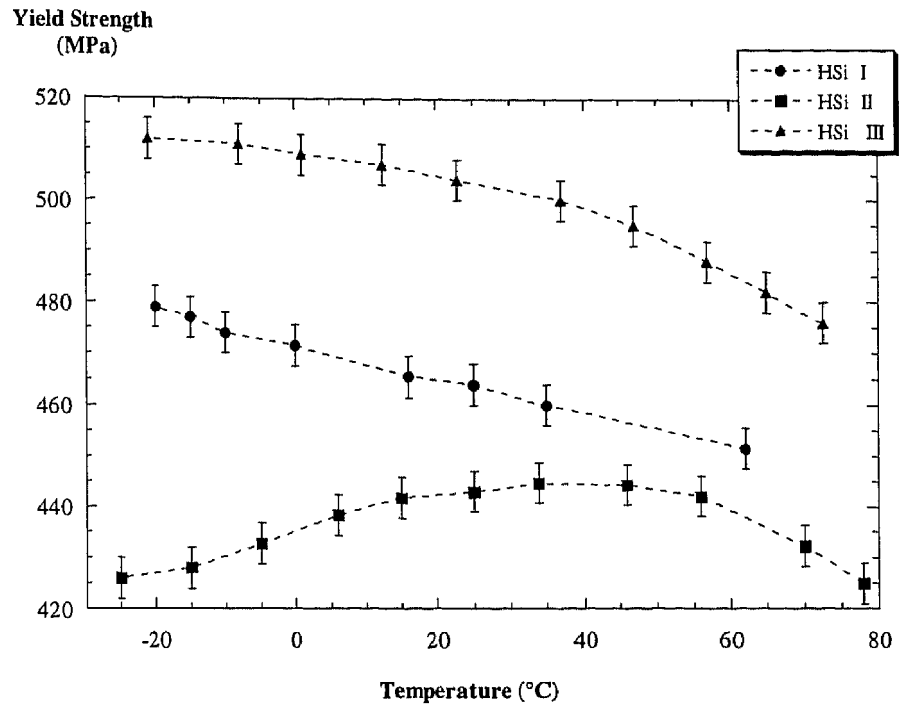

Figure 6.7: Evolution of yield strength as a function of temperature for specimens I, II and III of steel HSiI.

Figure 6.8 presents true stress – true strain curves of specimen V tested at 95°C, 65°C, 20°C and –20°C, respectively, together with the corresponding acoustic activity as represented by the Average Signal Level (ASL). As already presented in chapter V, continuous emission sources are dislocation motion and martensitic transformation. Each curve presents a first peak limited to the Lüders plateau. For the specimen tested at 95°C, the ASL sharply decreases at the end of the plateau and further plastic straining is accompanied by a low acoustic activity. For a testing temperature of 65°C, the ASL exhibits a higher mean level that decreases much more slowly with true strain so that it reaches the noise level only after a true strain of 0.12. For lower testing temperatures, i.e. 20°C and –20°C, the ASL shows higher values at the beginning of uniform straining but it also decreases more rapidly and reaches the noise level for a true strain of 0.08 at 20°C and 0.05 at –20°C.

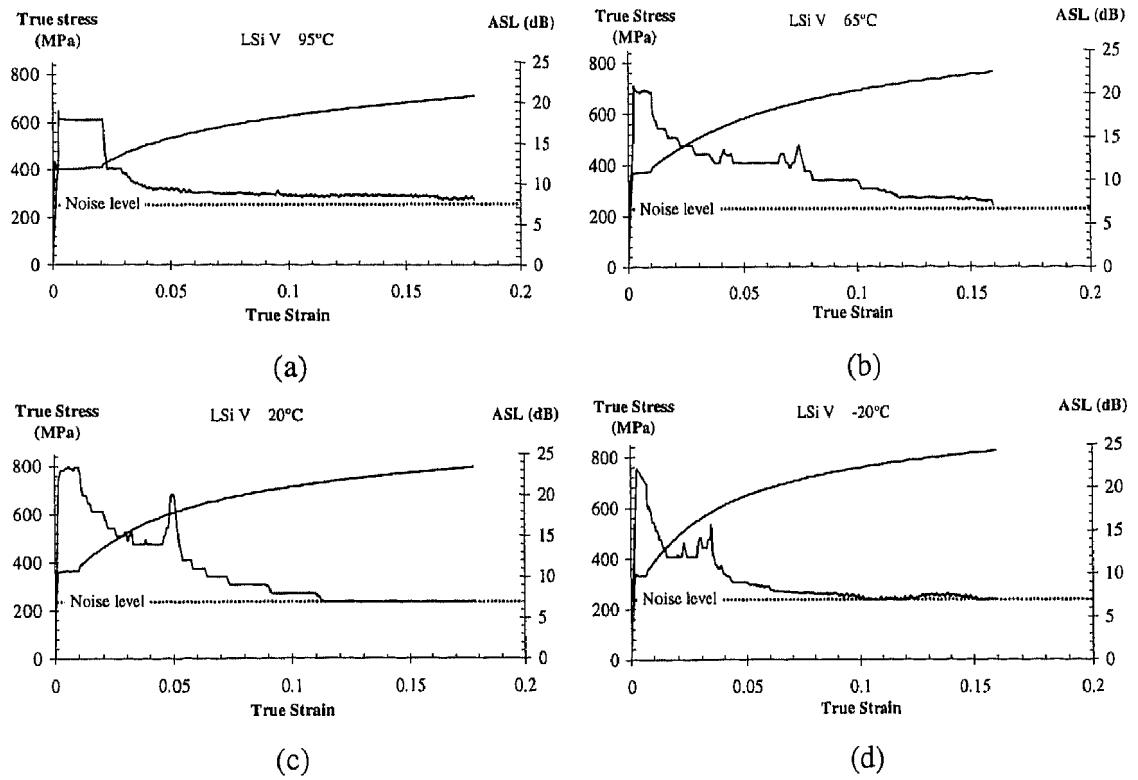

Figure 6.8: True stress - true strain curve and corresponding acoustic activity of specimen V of steel LSi tested at (a) 95°C, (b) 65°C, (c) 20°C, and (d) –20°C.

Figure 6.9 shows the evolution of the incremental work-hardening exponent ($n_{incr.}$) as a function of true strain, for specimens V and VI of steel LSi tested at different temperatures. $n_{incr.}$ curves present high values after the onset of yielding. The incremental work-hardening exponent thereafter decreases to final values around 0.17. Tensile testing at different temperatures influences the incremental work-hardening curves in the same way for specimens V and VI. Testing at temperatures lower than room temperature brings about a high value of $n_{incr.}$ in the first steps of plastic strain. However, this high value of $n_{incr.}$ is followed by a more pronounced decrease with plastic strain so that plastic instability occurs for lower true uniform strains than at high temperature. Tensile tests carried out at higher temperatures show lower initial values which decrease more slowly.

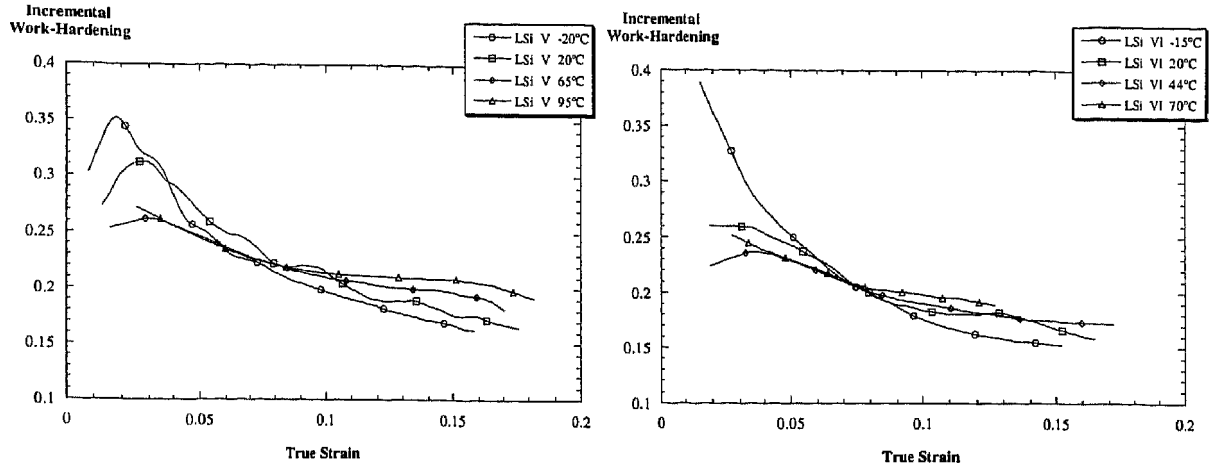

(a) (b)

Figure 6.9: Incremental work-hardening curves ($n_{incr.}$) of (a) specimen V and (b) specimen VI of steel LSi tested at various temperatures.

Figure 6.10 shows the evolution of retained austenite measured by Mössbauer spectroscopy as a function of true strain for specimen IV of steel LSi tested at room temperature and at 100°C. The very low stability of austenite in specimen IV (due to a very low carbon content as shown in chapter V) brings about its very fast martensitic transformation during straining at room temperature. In contrast, almost no austenite transforms when the tensile test is carried out at 100°C.

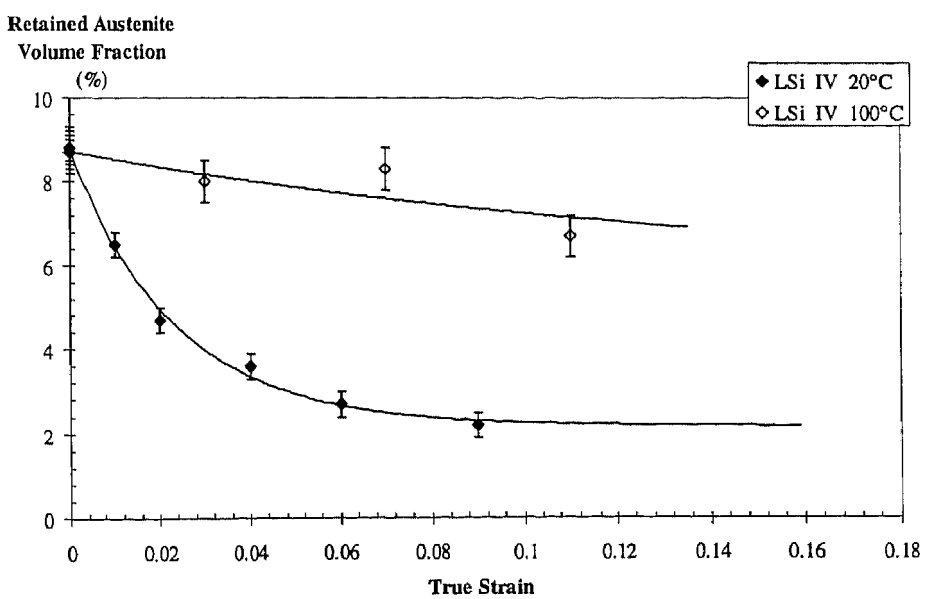

Figure 6.10: Retained austenite volume fraction as a function of true strain for specimens IV tested at room temperature and at 100°C.

Figure 6.11 presents SEM micrographs of specimens V and VI of steel LSi after tensile testing up to the onset of necking at room temperature (figure 6.11(a)) or at 100°C (figures

6.11(b) and 6.11(c)). As shown in figure 6.10, only about 2 % of austenite remains untransformed at necking when the tensile test is carried out at room temperature. This remaining austenite consists mainly of isolated intragranular austenite dispersed within idiomorphic ferrite as shown in figure 6.11(a). On the other hand, a much larger part of retained austenite remains untransformed at the onset of necking when the tensile test is carried out at 100°C. As shown in figures 6.11(b) and 6.11(c), not only intragranular austenite but also *blocky* austenite associated with bainite at grain boundaries of idiomorphic ferrite does not transform during tensile straining at 100°C.

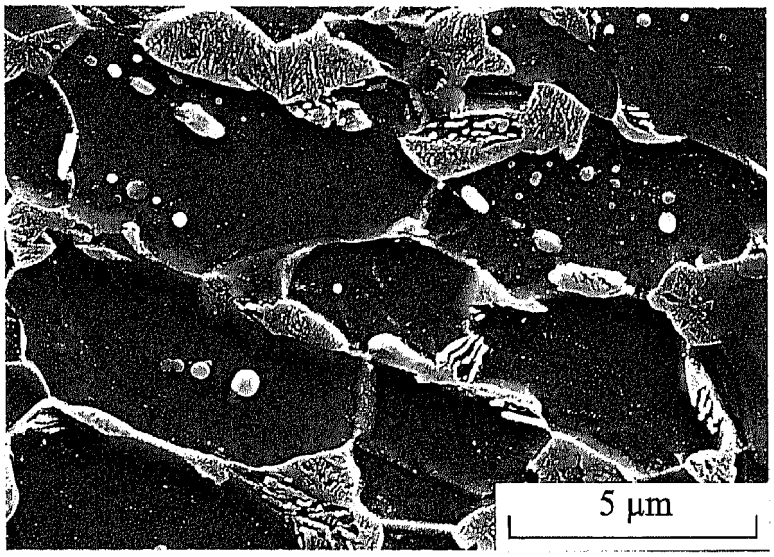

(a)

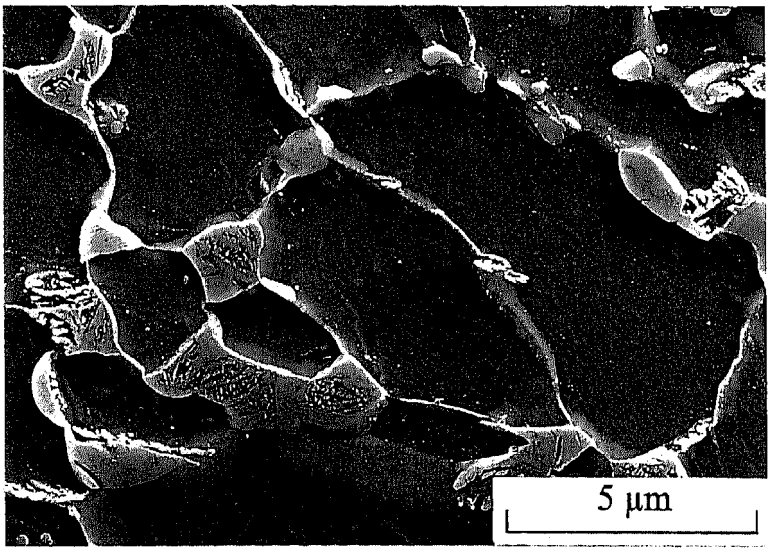

(b)

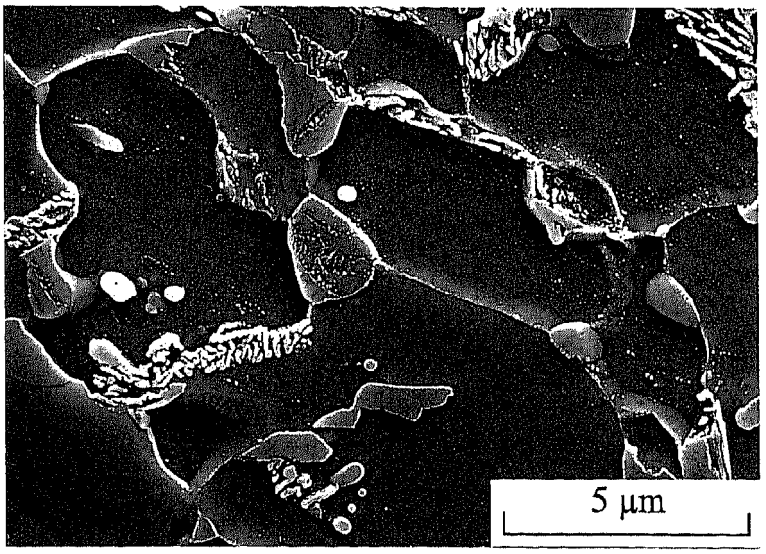

(c)

Figure 6.11: SEM micrographs after tensile testing up to true uniform strain (a) of specimen V strained at room temperature, (b) of specimen V strained at 100°C, and (c) of specimen VI strained at 100°C.

4. Discussion

In fully austenitic TRIP steels [Olson78, Olson82, Tamu82, Tamu92] or ultra-high-strength martensitic steels containing small amounts of dispersed austenite [Haid87, Haid89a, b], it was possible to define the temperature M_s^σ as the temperature corresponding to the reversal of the temperature dependence of the yield stress associated either to the martensitic transformation of retained austenite or to the deformation by slipping (or twinning) of this retained austenite. M_s^σ thus delineates the 2 temperature ranges where the beginning of yielding corresponds to different mechanisms. It was shown that optimum values of strength, ductility or toughness are obtained when the samples are tested at temperature M_s^σ [Haid87, Tamu82, Tamu92]. M_s^σ thus constitutes a quantitative parameter for characterising austenite stability against deformation-induced martensitic transformation.

In order to establish this reversal of the flow stress temperature, Richman et.al. [Rich71] developed a single specimen technique consisting in loading the specimen to the 0.2% flow stress (or to a smaller strain offset) starting from high temperature and then repeating this measurement when decreasing progressively the test temperature. One underlying hypothesis to this method of determination of M_s^σ is that the austenite behaviour dominates yielding. This hypothesis is obvious in the case of the fully austenitic TRIP steels. In the ultra high-strength martensitic steels containing dispersed retained austenite, martensite

exhibits a much higher yield strength than austenite, so that the austenite behaviour undoubtedly also dominates yielding in these steels [Haid89a].

The situation is not so evident in the case of TRIP-assisted multiphase steels for which the major part of the microstructure consists of soft idiomorphic ferrite. The onset of yielding may then be induced only by plastic deformation of ferrite or it may result from complex interactions between the different phases constituting the microstructure. This is why it was anticipated that the single specimen technique would not be successful for determining the M_s^{σ} temperature in our steels. In consequence, complete tensile tests up to the onset of necking were conducted at each investigated temperature.

The 2 sets of results dealing either with micro-yielding or with more macroscopic properties such as σ_{TS} or ε_u have shown that the temperature dependence of the properties of specimens V and VI of steel LSi allows defining transition temperatures corresponding to particular mechanical behaviours.

All different phases present in the microstructure may contribute to the onset of yielding. Indeed, figure 6.5 has shown that specimen V exhibits in the lower strain region both continuous yielding and Lüders plateau. Continuous yielding is observed in the case of Dual Phase steels because enough free dislocations are generated in ferrite for accommodating the austenite – martensite transformation occurring during cooling [Bour83, Sach83]. On the other hand, the Lüders plateau corresponds to the releasing of dislocations locked by the segregation of interstitial C and N atoms. As specimen V contains a small amount (~ 5%) of thermal martensite, both the movement of free dislocations generated by martensitic transformation and then the release of the locked dislocations, are observed in this specimen. It was shown that, in the case of Dual Phase steels [Naka77, Rigs79, Hans81] a minimum amount of martensite is necessary to avoid the appearance of the Lüders plateau as a result of a sufficient deformation of ferrite during the martensitic transformation [Rizk82, Bour83].

As reported in chapter V, acoustic emission is generated by dislocation motion in the deforming material and is more particularly related to the rate of change of the mobile dislocation density. The differences in the acoustic signature of ferrite-martensite and ferrite-bainite samples at the onset of yielding shown in figure 6.3 are therefore related to the mechanisms of movement of dislocations at the onset of microyielding. It can be postulated that the free dislocations generated in the ferritic phase of the ferrite-martensite microstructure can start moving progressively as stress concentrations rise around hard martensite grains. As a consequence, the ASL increases progressively during continuous

yielding. On the other hand, a finite stress is needed in the case of the ferrite-bainite sample in order to counteract pinning by solute atmospheres. Once this stress is attained, avalanches of dislocations are abruptly generated and the ASL shows a steep increase.

Supplementary features corresponding to particular acoustic activities arise in the lower strain regions of specimens V and VI when testing in the temperature range from -20°C to 120°C. Figure 6.12 schematically presents the typical stress-strain behaviours around the elastic – plastic transition together with the corresponding acoustic activities observed in 3 different temperature ranges for specimen VI. The evolution of the flow stresses at various strain offsets as a function of temperature is also represented. Above around 55°C, a slope change and a transient linear zone is observed in the stress – strain curve between the elastic zone and the Lüders plateau. This slope change occurs at decreasing stress when temperature increases. Furthermore, this transition zone is associated with a specific, clearly distinguishable acoustic emission. This transition zone cannot be associated with the martensitic transformation of retained austenite as figure 6.10 shows that austenite remains untransformed up to very large plastic strain (even when austenite is very unstable as in specimen IV). On the other hand, dislocation motion in idiomorphic ferrite begins with the Lüders plateau where avalanches of abruptly unlocked dislocations generate a high acoustic activity. It may therefore be concluded that the transition zone observed above 55°C corresponds to the plastic deformation of retained austenite. As already observed by transmission electron microscopy [Jeong93], retained austenite of TRIP-aided steels deformed at around 100°C does not transform but exhibit features such as shear bands and deformation twins. This plastic deformation of austenite can generate its own acoustic emission as observed in figure 6.4(a). When temperature is comprised between about room temperature and 55°C, only a sharp transition from the elastic zone to the Lüders plateau can be observed. No yielding at small strain offsets arises prior yield point elongation. As for the ferrite-bainite specimen, this type of onset of yielding is accompanied by a steep increase of the ASL level. This means that, in this temperature range, no phase other than ferrite intervenes in the first plastic deformation. Below room temperature, a second type of transition zone appears between the elastic zone and the Lüders plateau. This zone becomes larger when temperature decreases. The slope of stress-strain curve then smoothly decreases to the Lüders plateau. The acoustic activity accompanying this transition monotonically increases from approximately the noise level to a maximum during the yield point elongation. This type of acoustic signature is identical to the acoustic activity of the ferrite-martensite microstructure during the onset of continuous yielding. Furthermore, it was shown in chapter V that in specimen VI, retained austenite transforms at room temperature during the very first part of straining. It may therefore be postulated that, in this temperature range, the martensitic transformation of

retained austenite occurs before the unlocking of dislocations in ferrite. Free dislocations are thus generated in ferrite due to the accommodation of martensite, which brings about microyielding prior to the Lüders plateau.

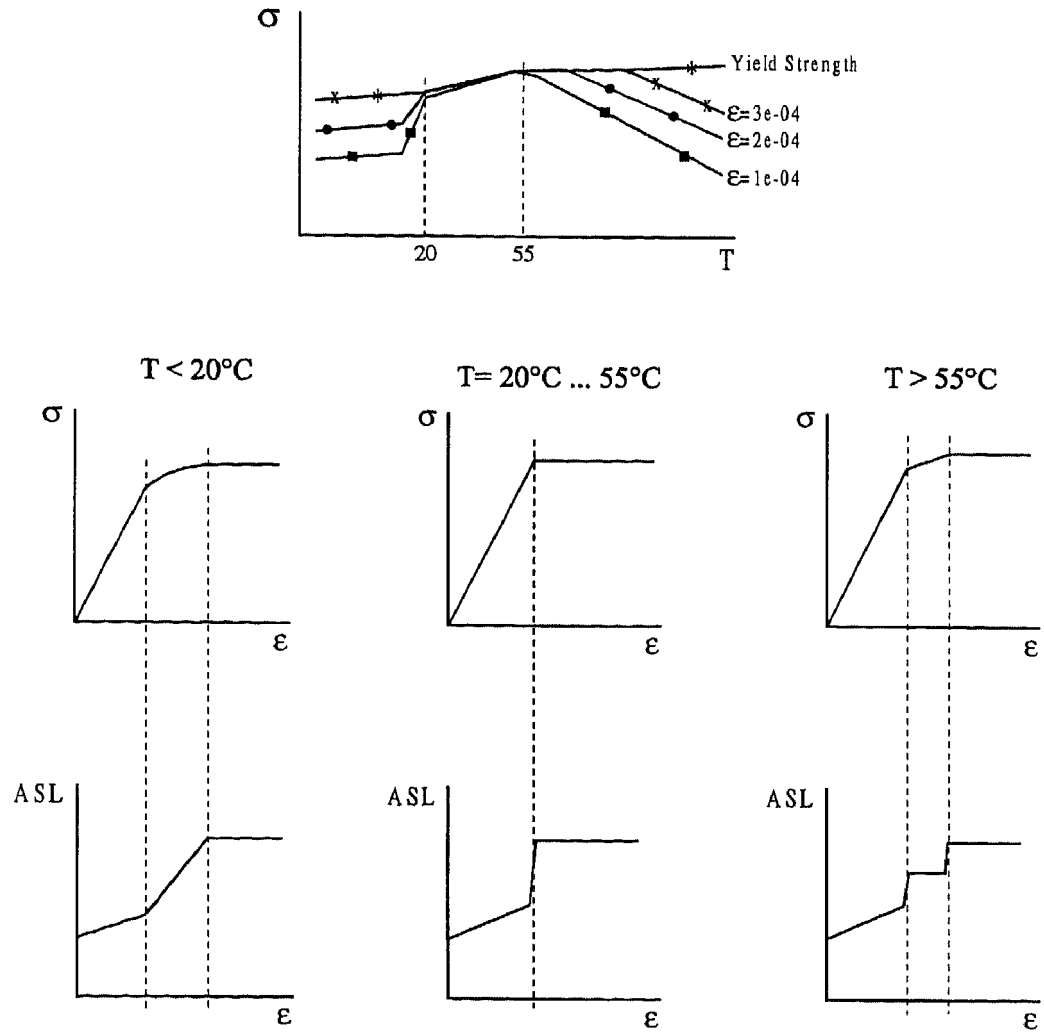

Figure 6.12: Schematic representation of typical stress-strain behaviours at the elastic – plastic transition together with the corresponding acoustic activities and of the evolution of flow stresses at various strain offsets as a function of temperature observed for specimen VI in 3 different temperature ranges.

In the case of specimen V, such different temperature regimes for the onset of yielding are not so well observable because of the presence of thermal martensite that induces a small continuous yielding region prior to yield point elongation at all temperatures. This continuous yielding hides the other mechanisms playing a role in microyielding. However, figure 6.5 has shown that above about 85°C, a slope change is observed in the continuous yielding part of the stress – strain curve of specimen V. This slope change is associated to about the same jump of ASL as for specimen VI . As shown in figure 6.2, this slope

change leads to some decrease of the flow stress at a 4 10^{-4} strain offset for temperatures higher than 85°C.

In summary, specimens V and VI exhibit different transition behaviours at the end of their elastic deformations when the temperature is varied between –20°C and 120°C. Typical acoustic signatures are associated with these behaviours which can be related to either plastic deformation or martensitic transformation of retained austenite. Furthermore, the temperature dependence of the flow stress at small strain offsets present a reversal. It may therefore be postulated that this transition corresponds to M_s^{σ} which is situated around 85°C and 55°C for specimens V and VI, respectively. As these 2 specimens only differ by their bainitic tempering time, austenite only differ by carbon content as shown in Table 6.2 (0.68wt.% and 0.73wt.% respectively). According to the empirical formula of Andrews [Andr65], Ms decreases by about 420°C per each percent in weight of carbon. It is quite remarkable that the difference in M_s^{σ} temperature between specimens V and VI is about the same as the M_s shift due to the difference in carbon content predicted by the Andrews formula. Using this same effect of carbon, M_s^{σ} temperature of retained austenite of specimen IV containing 0.61wt.% of carbon should be around 110°C

The estimated M_s^{σ} temperatures is lower for specimen VI than for specimen V. This ranking is thus identical as for the M_s temperatures. Using the correlation established in the literature between M_s^{σ} and the mechanical stability of retained austenite [Haid89a, b], this means that for tensile testing at room temperature, retained austenite should be considered as presenting a better mechanical stability in specimen VI than in specimen V. However, it was shown in chapter V that the transformation rate of retained austenite is more progressive in specimen V as a result of the presence of the other surrounding phases such as thermal martensite. It can therefore be concluded that M_s^{σ} characterises the intrinsic mechanical stability of retained austenite without taking into account the effect of the other phases and the way austenite transforms during plastic straining.

Nevertheless, the temperatures M_s^{σ} defined by considering the microyielding behaviour also corresponds to particular points in the temperature evolution of yield strength σ_y (defined as the true stress of the Lüders plateau), true stress at maximum load σ_{TS} or true uniform strain ε_u. As shown in figure 6.6(a) the yield strength is constant or slightly decreases for temperatures higher than 80°C and 50°C respectively while it decreases when temperature decreases below these 2 values. The yield strength of fully ferritic or ferrite-pearlite microstructures (in which no other deformation mechanism than slip can occur) decreases with increasing temperature [Lesl67, Lesl72, Sach82] because of the thermally activated nature of the resistance to the motion of dislocations. The fact that

yield point elongation occurs for decreasing stresses when temperature decreases below M_s^{σ} means that another mechanism than thermal activation, i.e. martensitic transformation of retained austenite, makes easier the unlocking of dislocations by generating stress concentrations. The martensitic transformation occurs more rapidly for decreasing temperatures and the formation of Lüders bands is induced at lower stress.

Figure 6.7 has shown that in specimens I and III of steel HSiI, yield strength monotonically decreases with increasing temperature as it should do when no other deformation mechanism interacts with Lüders band formation. This result is in good agreement with chapter V in which it was shown that the retained austenite in specimens I and III is very stable at room temperature in such a way that almost no austenite transforms before a true strain of 0.04. Furthermore, it may be speculated that the strong solid solution strengthening of austenite by carbon observed by some authors in the case of austenitic Fe-Ni-Cr-C steels [Chan71, Tamu82] also prevails here. In such a carbon rich austenite, yielding occurs for stresses higher than the yield strength of idiomorphic ferrite. It seems therefore that austenite does not play a role in the onset of yielding in these 2 specimens. However, specimen II which presents a reduced austenite stability due to a low carbon content exhibits the same behaviour as specimens V and VI, i.e. an earlier onset of the Lüders plateau when temperature decreases. It may be therefore speculated that the M_s^{σ} temperature of specimen II of steel HSiI is situated around 40°C.

As shown in figures 6.6(b) and 6.6(c), the true stress at maximum load and the true uniform strain are no so markedly affected by the temperature M_s^{σ}. Indeed, these 2 properties result not only of the transformation or deformation of austenite but also of the mechanical behaviour of the other phases. Figure 6.6(b) shows that the true stress at maximum load progressively decreases when the test temperature increases. This decrease was already observed in the literature [Saku92, Jeong93, Saku93, Sugi93]. It is due to the loss of strengthening provided by martensite. Indeed, deformation-induced martensitic transformation of retained austenite progressively disappears when temperature increases [Saku92, Sugi92a, Jeong93, Saku93]. As shown in figure 6.10, austenite does not transform when straining around 100°C even when austenite is very unstable at room temperature such as for specimen IV. This change in the fraction of transformed austenite as a function of plastic strain is also reflected in the acoustic emission results of figure 6.8. The part of the ASL attributed to the martensitic transformation of retained austenite in chapter V becomes progressively more distributed along plastic strain when temperature increases. However, the ASL is also lower and at 95°C (figure 6.8(a)), only acoustic signature of dislocation motion can be observed. Correspondingly, for both specimens, the incremental work-hardening exponent ($n_{incr.}$) steeply decreases with true strain at low

temperature whereas it more smoothly decreases at high temperature. The disappearance of the TRIP effect is therefore accompanied by a global decrease of the hardening that was attributed to martensite and martensite-ferrite interactions. Furthermore, higher final values of $n_{incr.}$ are sometimes obtained at high temperature when dynamic strain aging arises. The resulting inhomogeneous deformation and the high strain rate sensitivity can then lead to large true uniform strain (with a large scatter). Nevertheless, the reduction of the deformation-induced martensitic transformation seems to be accompanied by a decrease of true uniform strain. Indeed, ε_u shows lower values for temperatures higher than the temperatures M_s^{σ}.

5. Conclusion

The mechanical stability of retained austenite dispersed in the microstructure of 2 TRIP-assisted multiphase steels has been characterised by considering the effect of the testing temperature both on the onset of yielding and on the mechanical properties measured by uniaxial tensile test. It was shown that a transition temperature corresponding to a change in the evolution of yield strength, true stress at maximum load and true uniform strain can be defined for both specimens. Relating the acoustic emission to microscopic sources, it was demonstrated that temperature ranges can be defined in which the onset of yielding is generated by plastic deformation of austenite, by martensitically induced dislocation unlocking in ferrite, or by martensitic transformation of retained austenite. These results therefore allow to define the temperature M_s^{σ} of each specimen, which corresponds to a reversal of the temperature dependence of flow stresses at small strain offsets. These M_s^{σ} temperatures are in good agreement with the austenite stabilising effect conventionally attributed to carbon enrichment of austenite and with the resulting lowering of the M_s temperature. However, M_s^{σ} cannot be used in this particular case as a quantitative gauge of mechanical stability of retained austenite since chapter V has shown that the transformation rate of austenite during straining also depends on the strengthening effect of the surrounding phases. M_s^{σ} therefore characterises the intrinsic mechanical stability of retained austenite. The mechanical properties of the other phases constituting the microstructure have to be jointly considered in order to fully justify the tensile properties of the TRIP-assisted multiphase steels.

References

[Andr65] K.W. Andrews: *J. Iron and Steel Inst.*, 1965, pp. 721-727

[Bour83] D.L. Bourell, and A. Rizk: *Acta Metall.*, 1983, vol. 31(4), pp. 609-617

[Chan71] G.R. Chanani, V.F. Zackay, and E.R. Parker: *Metall. Trans.*, 1971, vol. 2, pp. 133-139

[Haid87] G.N. Haidemenopoulos, G.B. Olson, and M. Cohen: *Proc. 34th Sagamore Army Materials Research Conf.*, Lake George, New York, 1987, pp. 549-593

[Haid89a] G.N. Haidemenopoulos, M. Grujicic, G.B. Olson, and M. Cohen: *Acta Metall.*, 1989, vol. 37(6), pp. 1677-1682

[Haid89b] G.N. Haidemenopoulos, G.B. Olson, M. Cohen, and K. Tsuzaki: *Scripta Metall.*, 1989, vol. 23, pp. 207-212

[Hans81] S.S. Hansen, R.R. Pradhan: *Fundamentals of Dual-Phase Steels*, R.A. Kot and B.L. Bramfitt, eds., TMS-AIME, Warrendale, PA, 1981, pp. 113-144

[Jeong93] W.C. Jeong, D.K. Matlock, and G. Krauss: *Mater. Sc. Eng. A*, 1993, vol. A165, pp. 9-18

[Lesl67] W.C. Leslie, and R.J. Sober: *Trans. ASM*, 1967, vol. 60, pp. 459-484

[Lesl72] W.C. Leslie: *Metall. Trans.*, 1972, vol. 3, pp. 5-26

[Naka77] K. Nakaoka, K. Araki, and K. Kurihara: *Formable HSLA and Dual-Phase Steels*, A.T. Davenport ed., TMS-AIME, Warrendale, PA, 1977, pp. 126-141

[Olson78] G.B. Olson, and M. Azrin: *Metall. Trans. A*, 1978, vol. 9A, pp. 713-721

[Olson82] G.B. Olson, and M. Cohen: *Metall. Trans. A*, 1982, vol. 13A, pp. 1907-1914

[Rich71] R.H. Richman, and G.F. Bolling: *Metall. Trans.*, 1971, vol. 2, pp. 2451-2462

[Rigs79] J.M. Rigsbee, J.K. Abraham, A.T. Davenport, J.E. Franklin, and J.W. Pickens: *Proc. Conf. Structure and Properties of Dual Phase Steels*, R.A. Kot and J.W. Morris ed., TMS-AIME, Warrendale, PA, 1979, pp. 304-329

[Rizk82] A. Rizk, and D.L. Bourell: *Scripta Metall.*, 1982, vol. 16, pp. 1321-1324

[Sach82] A.K. Sachdev: *Metall. Trans. A*, 1982, vol. 13A, pp. 1793-1797

[Sach83] A.K. Sachdev: *Acta Metall.*, 1983, vol. 31(12), pp. 2037-2042

[Saku92] Y. Sakuma, D.K. Matlock, and G. Krauss: *Metall. Trans. A*, 1992, vol. 23A, pp. 1233-1241

[Saku93] Y. Sakuma, D.K.Matlock, and G. Krauss: *Mater. Sc. Technol.*, 1993, vol. 9, pp. 718-724

[Sugi92a] K. Sugimoto, M. Kobayashi, and S. Hashimoto: *Metall. Trans. A*, 1992, vol. 23A, pp. 3085-3091

[Sugi92b] K. Sugimoto, N. Usui, M. Kobayashi, and S. Hashimoto: *ISIJ Int.*, 1992, vol. 32, pp. 1311-1318

[Sugi93] K. Sugimoto, M. Misu, M. Kobayashi, and H. Shirasawa: *ISIJ Int.*, 1993, vol. 33, pp. 775-782

[Tamu82] I. Tamura: *Metal Sc.*, 1982, vol. 16, pp. 245-253

[Tamu92] I. Tamura, and C.M. Wayman: *Martensite*, G.B. Olson and W.S. Owen ed, ASM, 1992, pp. 227-242

Chapter VII

Damage and Fracture Toughness of TRIP-Assisted Multiphase Steels

A comparative characterisation of damage and fracture toughness of TRIP-assisted multiphase steel sheets exhibiting mechanically-induced martensitic transformation was performed on two different steel grades heat-treated in such a way as to contain different amounts of second phases and different retained austenite mechanical stability. Notched plates strained to various levels were used in order to analyse the coupling between damage and martensitic transformation. A phenomenological energetic criterion for the transformation was established from finite element simulation. Fracture resistance was characterised by means of JR curves and CTOD measurements using DENT specimens. Fracture toughness at cracking initiation appeared to be in the inverse ratio of the uniaxial tensile strength and ductility balance. The incompatibility between a strong TRIP effect improving formability by delaying shear localisation and a high fracture toughness at cracking initiation is shown to depend on microstructural parameters such as the volume fraction of non-idiomorphic ferrite phases or the mechanical properties of martensite. The crack propagation resistance was found similar in both steels. However, the steel presenting the largest TRIP effect seems to exhibit the best resistance to fatigue.

1. Introduction

Retained austenite can be present as a dispersed phase in a large variety of steels. Mechanical solicitation can induce martensitic transformation of this metastable austenite by providing the lacking driving force for the triggering of the transformation. This chapter is concerned with the TRansformation Induced Plasticity (TRIP) effect occurring in steels consisting of an idiomorphic ferrite matrix with retained austenite, martensite and bainite present as dispersed phases. Numerous studies have revealed that the TRIP effect can drastically improve strength and ductility [Zack67, Lud69, Olson75, Olson78, Olson82a, Strin92, Tamu92] by tuning the work-hardening rate in such a way that shear localisation is postponed [Olson82b]. Furthermore, the volume change associated with martensitic transformation is also sometimes thought to delay the nucleation of microvoids [Leal84], and thus the ensuing local softening inducing plastic localisation [Tver81, Tver82, Strin92]. Elucidation of the influence of the TRIP effect on fracture toughness is not straightforward, especially when austenite is dispersed among other phases. Indeed, the martensitic transformation of metastable austenite has been proved to have either a beneficial or a deleterious effect on fracture toughness.

Typically, mechanically-induced martensitic transformation is known to have a detrimental influence on the toughness of the heat affected zone in welds of high-strength low alloy steels [Chen84, Tail95, Tail96]. In such HAZ, the transformation of high carbon austenite (surrounded by phases such as bainite and acicular ferrite) into hard martensite during mechanical loading, gives rise to high stress concentration and stress triaxiality at the martensite-ferrite interface. Premature cracking of martensite grains or debonding of the ferrite-martensite interface can therefore impair the fracture toughness of the weld.

On the other hand, in Fe-Ni steels, Fe-Ni-Cr steels [Leal84], or other highly alloyed fully austenitic steels [Anto71], toughness shows a marked enhancement when testing temperature or steel composition is adjusted in such a way to correspond to a favourable stability of austenite. In ultra-high strength quenched and tempered martensitic steels such as AISI 4340 [Wood75, Park75, Haid89], Fe-Cr steels [Rao80], Fe-Ni steels [Yano73, Fult85], high Ni-Co secondary hardening martensitic steels [Haid87, Haid88], or also bainitic steels [Sand81, Miih87, Tomi93, Tomi95], toughening by transformation can bring about substantial improvement of fracture toughness when austenite presents an optimum stability. In these very-high strength steels, the fracture mechanism at the crack tip is strongly related to shear localisation: mixed mode zig-zag cracking and crack branching

are currently observed[1] [Olson96]. In that case, martensitic transformation indirectly improves fracture toughness by postponing shear localisation.

However, in most ductile materials, cracking from a preexisting defect is not directly related to shear localisation. Fracture toughness then usually depends on the material capacity to resist damage by nucleation and growth of internal voids or microcracks. Increasing the resistance to plastic localisation by increasing the work-hardening capacity does thus not necessarily imply an increase of cracking initiation resistance and tearing resistance. Indeed, the influence of flow properties and microstructure changes on damage is complex.

The purpose of the present chapter is to study how martensitic transformation affects damage and fracture toughness in TRIP-assisted multiphase steels. Since these steel grades are intended to formability applications, i.e. applications (such as deep-drawability or crashworthiness) requiring a high resistance to plastic instability combined with a high final strength, the literature dealing with the TRIP-aided steels is mainly focused on plastic properties.

Two TRIP-assisted multiphase steels were chosen which differed by the initial content and stability of retained austenite. A clear coupling between the damage kinetics and the martensite formation kinetics was established from metallographic observations of notched plates deformed to various strains. We also analyse the various damage mechanisms and the effect of the presence of two types of austenite, namely a blocky-type austenite and a film-type austenite. Using precracked DENT specimens, it will be shown that fracture toughness at cracking initiation characterised by means of JR curves and CTOD measurements decrease when the uniaxial tensile properties improve. Furthermore, 3D finite element simulations based on a J2 flow theory will allow establishing a phenomenological energetic criterion for the mechanically-induced martensitic transformation. The approximation of using a J2 flow theory will be discussed. The results presentation combines experimental and numerical observations but separates the characterisation of martensitic transformation and damage and the fracture toughness analysis. The discussion aims at gathering both of those microscopic and macroscopic approaches.

[1] Crack tip processes in thin sheets or in mode III loading are frequently driven by shear localisation.

2. Materials and Experimental Procedures

2.1. Materials

2.1.1. Chemical compositions and heat-treatment conditions

Steels HSiII and LSi differing by the carbon and silicon contents were investigated. Their chemical compositions are reminded in Table 7.1. Steel HSiII is a conventional TRIP-assisted multiphase steel with a silicon content of 1.5 wt.%. Steel LSi is a newly developed TRIP-aided steel (although based on an industrial alloy) with a much lower silicon content and a chemical composition rather comparable to conventional Dual Phase steels [Spei81]. A cast ingot of steel HSiII was hot-rolled to a thickness of 4mm following a classical route (see chapter II). Coiling was simulated at the relatively low temperature of 620°C for 1 hour so that the hot-rolled microstructure consisted of upper bainite with no banded structure. Steel HSiII was then cold-rolled 75% to 1 mm thickness. Steel LSi is an industrial alloy hot-rolled to a thickness of 5.5mm following classical practice. The resulting microstructure was therefore a ferrite-pearlite mixture which presented a slightly banded structure. Steel LSi was cold-rolled 82% to the same thickness of 1 mm.

(10^{-3} wt.%)	C	Mn	Si	P	S	Cr	Ni	Cu	Nb	Al	N
HSiII	290	1420	1410	12	20	3	7	4	0	40	8
LSi	160	1300	380	13	12	19	27	19	13	30	6.3

Table 7.1: Chemical compositions (10^{-3} wt.%) of the investigated steels.

Heat-treatments were carried out on 60 mm x 240 mm specimens oriented in the rolling direction. Samples were first intercritically annealed in a fluidised bed furnace. Steels HSiII and LSi were annealed at 760°C for 6min and at 730°C for 5min, respectively (i.e. in the lower part of the intercritical temperature range). They were then transferred to a lead bath furnace for the isothermal bainitic tempering. Steel HSiII was held at 410°C for 6 min while steel LSi was held at 370°C for 3 min (i.e. specimen LSi VI of chapters V and VI). Both steels were finally water-quenched to room temperature.

2.1.2. Microstructure and mechanical properties

Figure 7.1 presents typical SEM micrographs of the microstructure of steel HSiII and steel LSi respectively. It can be seen on these micrographs that the microstructure of both specimens consists of a finely grained idiomorphic ferrite matrix with a dispersion of

bainite and austenite grains mainly situated at the ferrite grain boundaries. No martensite can be found in the microstructure prior to mechanical testing. These micrographs also show that 2 types of retained austenite coexist in the microstructure: a *blocky type* austenite and a *film type* austenite associated with bainitic ferrite. The volume fractions of the different phases were measured by combining image analysis, dilatometry and Mössbauer spectroscopy (for retained austenite) (see chapter III). The results are summarised in Table 7.2. For steel HSiII, idiomorphic ferrite represents 55% of the microstructure while the volume fractions of bainite and retained austenite are 29% and 16%, respectively. In the case of steel LSi, the volume fraction of idiomorphic ferrite is larger (75%) while bainite and retained austenite represent 19% and 6% of the microstructure, respectively. The carbon content of retained austenite was estimated from the austenite lattice parameter measured by x-ray diffraction (see chapter III). The carbon content of retained austenite in steel HSiII was 0.9wt.% while it was only 0.73wt.% in steel LSi. Steel HSiII therefore presents a higher austenite volume fraction and a more stable austenite.

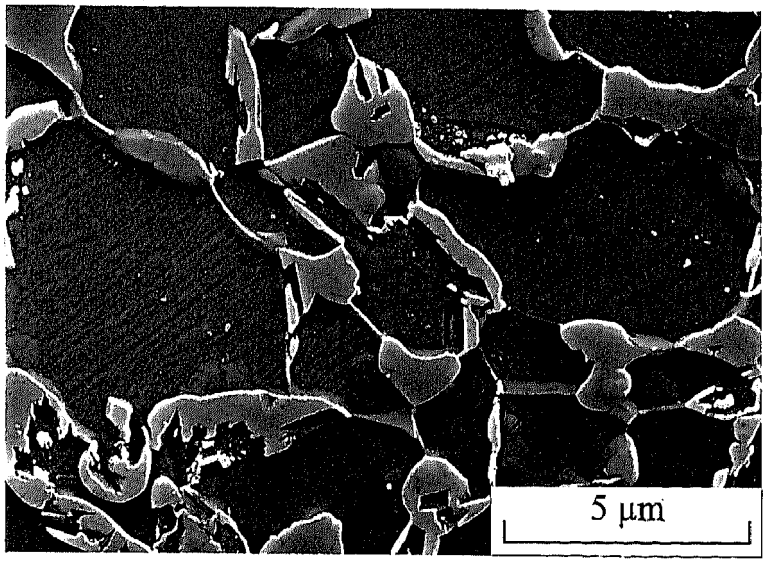

(a)

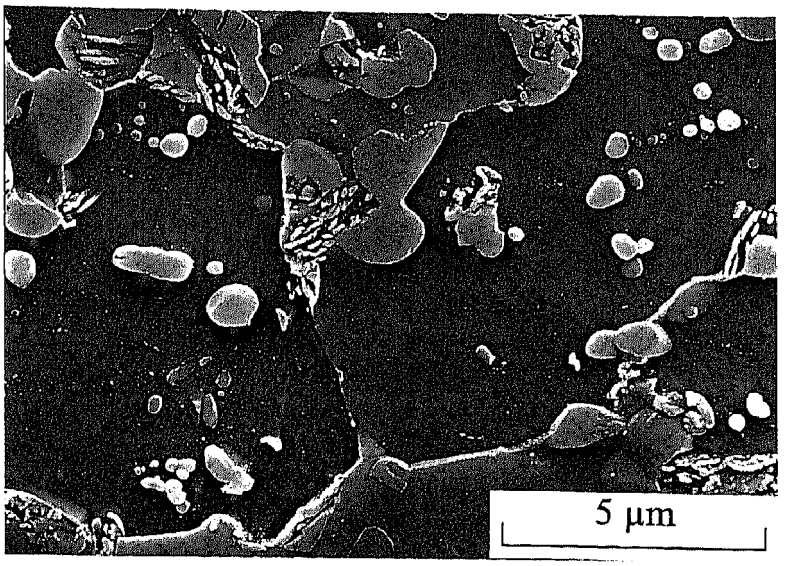

(b)

Figure 7.1: Typical SEM micrographs of the microstructure of (a) steel HSiII and (b) steel LSi before straining.

(%)	*Ferrite*	*Bainite*	*Retained Austenite*	*Cγ* (wt.%)
HSiII	55	29	16	0.9
LSi	75	19	6	0.73

Table 7.2: Volume fractions of the different phases of the microstructure of steels HSiII and LSi and estimated carbon content of retained austenite.

Figure 7.2 presents the tensile true stress – true strain curves of both specimens together with the incremental work-hardening curves ($n_{incr.}$). Tensile specimens were prepared according to the European standard EN 10002-1 with an initial gauge length and width of 50 mm and 12.5 mm respectively. Figure 7.2 shows that, with a true stress at maximum load of 1115 MPa and a true uniform strain of 0.25, steel HSiII exhibits better strength-ductility balance than steel LSi (774 MPa and 0.17 respectively). The yield strength of steel HSiII is also higher than that of steel LSi (490 MPa against 430 MPa). These differences are mainly attributed to the TRIP effect: as shown in chapters IV and V, the incremental work-hardening curves can be directly related to the austenite transformation rate. The more stable austenite of steel HSiII progressively transforms all over straining in such a way that the incremental work-hardening smoothly increases from a low initial value. This increase delays the onset of necking. On the other hand, the less stable austenite of steel LSi transforms mainly during the early stage of plastic straining. The incremental strain-hardening exponent $n_{incr.}$ of steel LSi therefore exhibits a high initial

value followed by a monotonous decrease. Mössbauer spectroscopy indicated that, whereas almost no austenite remains in steel LSi after straining to the onset of necking, about half of the initial content of austenite is still present in the microstructure of steel HSiII at ε_u.

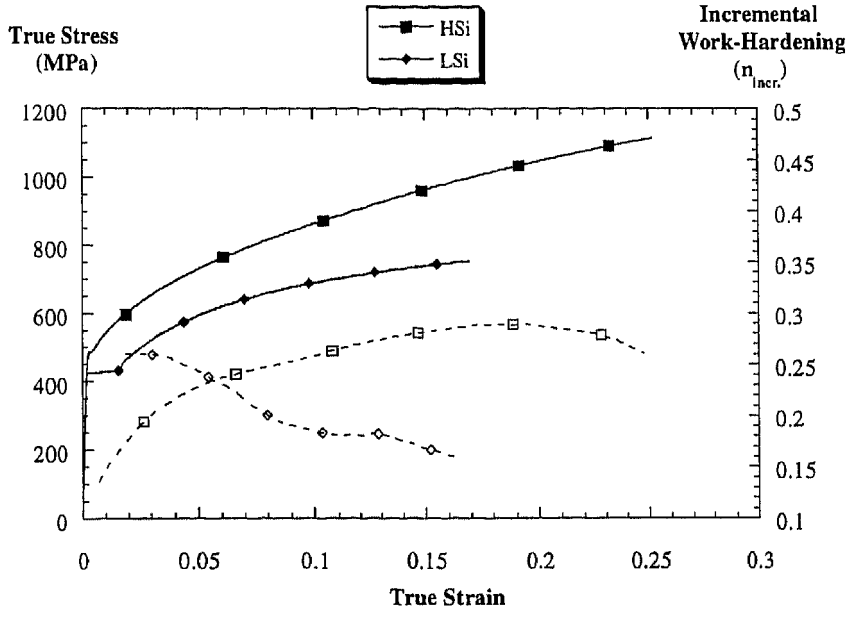

Figure 7.2: Uniaxial tensile true stress – true strain curves and incremental work-hardening curves of steels HSiII and LSi.

2.2. Experimental procedures

2.2.1. Characterisation of martensitic transformation and damage

The geometry of the notched plates used to investigate the strain dependence of martensitic transformation and damage is shown in figure 7.3. Notched plates were chosen for this study because: (i) the stress triaxiality around the notch is close to the stress triaxiality around a crack (at least beyond the finite strain crack tip zone); (ii) notched plates do not present the difficulties linked to necking which arise in non-notched specimens; (iii) notched plates allow collecting more information than smooth plates by taking advantage of the strain gradients which develop along the ligament between the notches. The specimens were strained to various average deformations, $\varepsilon_{aver} = \ln(S0/Sf)$ (where $S0$ and Sf are the initial and final minimum cross-section areas, respectively), and they were then unloaded for metallographic observation. Sf was obtained from the final ligament length measured using a travelling microscope and from the final ligament thickness measured at various locations along the ligament length using a profilometer. Each specimen was first ground to midsection, then tempered at 200°C for 2 hours in order to allow observation of martensite (see chapter II) and finally polished and etched with 2% Nital. As suggested in

figure 7.3, maps of the proportion of martensite and of the number of damage sites were obtained by SEM observation of one quarter of the strained zone. Proportion of martensite from the transformation of retained austenite was estimated by ranges of 25%. The number of damage sites was also counted. Record was also taken of the nature of the microcracks, i.e. ferrite-martensite interface debonds (FM), martensite cracking in different directions with respect to the tensile direction (MM0°, MM45°, MM90°), or other types of damage.

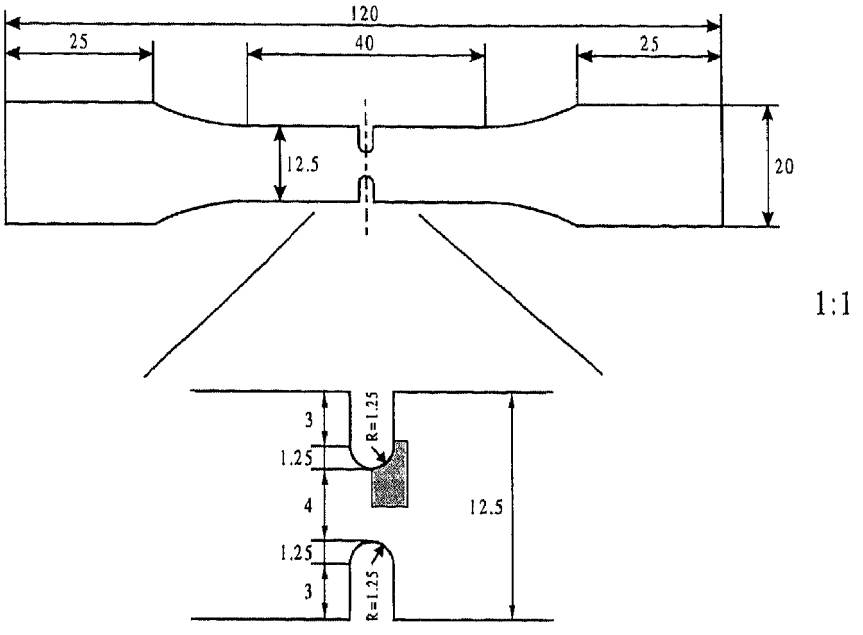

Figure 7.3: Geometry of the notched specimens used for the characterisation of damage and martensitic transformation of both steels. As represented by the darkened zone, only one quarter of the ligament was characterised due to symmetry of the specimens.

2.2.2. Fracture toughness measurements

Figure 7.4 shows the DENT geometry used for the evaluation of fracture toughness. The specimens width, w, was 55mm and the thickness, t_0, was 1 mm. Precracking of the specimens was carried out by fatigue loading using a servo-hydraulic machine. Notches were first machined by spark-erosion followed by razor blade cutting. These notches allowed rapid initiation of the fatigue precrack. In order to obtain 2 mm long fatigue cracks on both sides of each specimen and to conserve symmetry, the side of the DENT plate at which the fatigue crack length first attained 2 mm was clamped and the fatigue loading was further carried out until the second fatigue crack had also reached 2 mm length. The maximum applied load was chosen in such a way that the maximum stress intensity factor

during precracking never exceeded 20% of the expected fracture toughness of the plate (which was verified a posteriori). The ratio *a/w* after precracking was always close to 0.5. The width of the zone along crack edges where martensitic transformation had occured during fatigue precracking was measured by SEM observation. This width was found to be equal to 30 µm for steel HSiII and 40 µm for steel LSi. Assuming that the fracture process zone (FPZ) size is similar to the finite strain zone length which may be estimated as equal to at least twice the critical crack tip opening displacement δ_C [Hutch83], the FPZ size appears to be at least 3 times larger than the zone in which martensitic transformation was observed to have occurred during precracking (see further). Consequently, the fracture toughness values at cracking initiation can be considered representative of the material with retained austenite. They thus are supposed to account for the influence of the TRIP effect on cracking resistance.

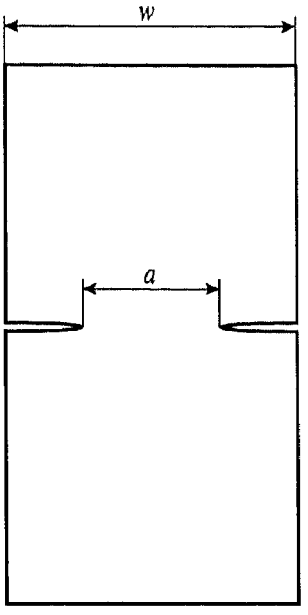

Figure 7.4: Geometry of the DENT specimens used for the fracture toughness measurements.

The precracked DENT specimens were loaded in tension. The tests were interrupted at various load levels (multiple-specimens method). In order to characterise the cracking resistance by JR curves, the J integral [Rice68] and the crack advance, Δa, were determined for each specimen. J was computed from the load/displacement curve using the formula of Rice *et al.* [Rice73] for the DENT

$$J_{Rice} = \frac{K_I^2}{E} + \frac{1}{l_0 t_0}\left(2\int_0^{U_p} P(u_p)du_p - PU_p\right) \qquad (1)$$

where K_I is the mode I stress intensity factor, E is the Young's modulus, $P(u_p)$ is the applied load and u_p is the plastic displacement. No correction for crack advance was made. Δa was measured on polished section on both sides of the specimens. In order to account for tunnelling effect, measurements were performed on the plate surface, at quarter thickness and at mid thickness of the plate. Δa was averaged on both sides of the specimens for all the through thickness measurements. This method allowed quantifying the crack tip quantities defined on figure 7.5: the total opening of the blunted crack δ_1, the opening of the tearing crack at the blunted crack δ_2, and the crack advance due to tearing, Δa_r. δ_1 - δ_2 can be used to obtain the unloaded critical crack tip opening displacement at cracking initiation, noted δ^*_C. Indeed, δ^*_C is obtained as the value of δ_1 - δ_2 when $\Delta a_r \rightarrow 0$ [Pard98a]. Because of plastic rotation and of large strain effects, δ_1 - δ_2 diverges from δ^*_C when Δa_r increases. This method has been described by Pardoen et. al. [Pard98a] together with a simple analytical model to calculate the value of δ_C before unloading. Account must be taken of the elastic part of the CTOD at cracking initiation, δ_{el}, as well as of the change of the CTOD due to the reversal of plastic strain during loading, noted Δ_{pc}. In this chapter, the unloading of the CTOD will be evaluated accurately using finite element computations (see further).

The resistance to crack propagation is characterised by the tearing modulus T_R defined as:

$$T_R = \frac{E}{\sigma_0^2}\frac{dJR}{da} \tag{2}$$

where E is the Young modulus, σ_0 is the yield strength and a is the crack advance.

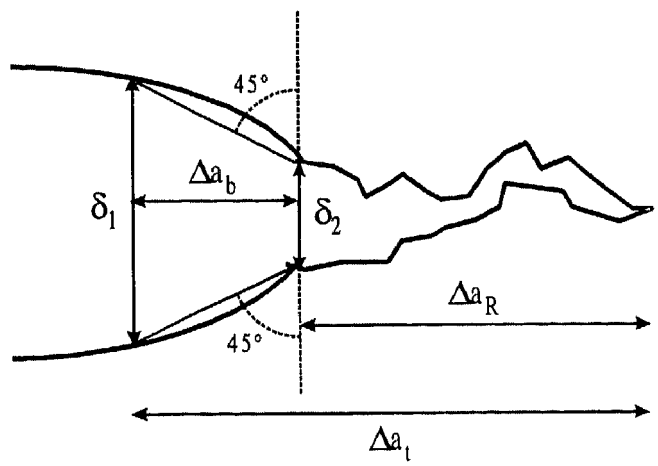

Figure 7.5: Schematic illustration of a crack tip and definition of the different parameters measured on the strained specimens.

3. Numerical Procedures

Three-dimensional finite element modelling of the notched and DENT specimens was based on a finite strain J2 flow theory with isotropic hardening and performed using the general-purpose program ABAQUS. The finite element meshes consisted of eight-node bricks. Owing to symmetry, only one eighth of each specimen was modelled. Figure 7.6 presents a mesh pattern for the two types of specimens. The minimum section of the notched specimens contained 15 elements on half of the ligament and 5 elements on half of the thickness. The initial radius of the crack tip in the DENT specimens was always taken lower than $0.15\delta_C$. The mesh consisted of 12 bricks along the half-thickness. The length of the first element close to the crack tip was chosen equal to half the initial radius of the crack tip. A mixed formulation was used in order to handle near incompressibility resulting from large plastic deformation. The uniaxial flow behaviour of steels HSiII and LSi was given in section 2.1.2. Other mesh designs were used in order to test convergence.

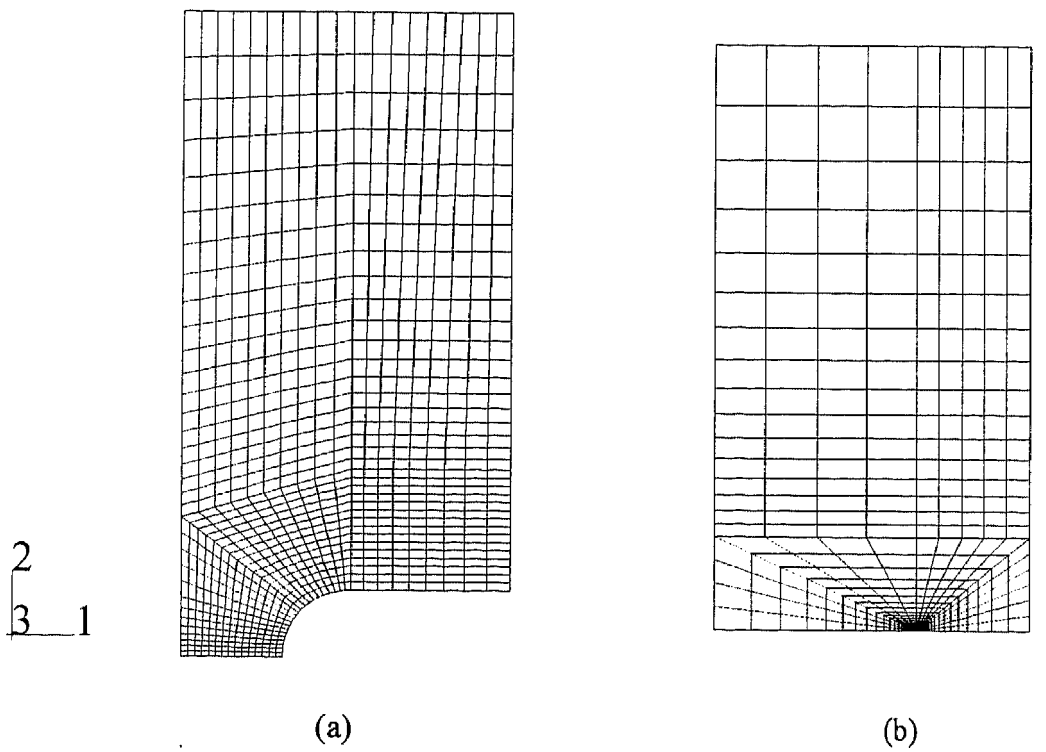

Figure 7.6: Meshes of the notch geometry (a) and of the DENT geometry (b) used for the finite element simulations.

The method of evaluations of the pointwise values of the J integral (relation (1)) over the crack front is based on the 3D domain integration technique proposed by Shih *et al.* [Shih86]. $J(s)$ was computed from various contours in order to check the path independence. A mean value for the J-integral was obtained by averaging the local values

on the entire thickness. The numerical δ_C was measured as the displacement at the intersection with the crack flanks of a 90° vertex centred at the crack tip (i.e. an identical definition as for the experimental measurement of δ_C).

There is some consistency in using the J2 theory based on the flow properties measured in uniaxial tension in order to simulate isothermal plastic flow in TRIP-assisted multiphase steels. Indeed, since the mixture of the phases is homogeneous without any preferential orientation, the J2 model based on the *macroscopic* uniaxial tension response would fairly well represent the *mean* flow behaviour[2]. However, the martensitic transformation, which presents transformation strains resulting from a displacive transformation mechanism, is stress triaxiality dependent [Strin92]. Stress triaxiality thus affects local strain-hardening. Nevertheless, the use of a J2 model appears pertinent, at least to obtain first insights into the quantification of the kinetics of the strain energy driven transformation, because (i) the range of stress triaxiality which develops in plates (with notches or cracks) is not as large as in plane strain structures; (ii) the modelled loadings are proportional except close to the crack tip in the DENT specimens; (iii) the volume affected by microstructural changes is small.

4. Experimental and Numerical Results

In this section, we present separately the results dealing with the martensitic transformation and damage of the notched specimens and the results dealing with the fracture toughness measurements using the DENT specimens. In each case, experimental and numerical results are presented together since direct comparison makes easier the apprehension of the coupling between martensitic transformation, damage occurrence and fracture toughness.

4.1. Transformation and damage

Figure 7.7 presents the average stress (ε_{aver}) versus average strain (σ_{aver}) variations determined experimentally as well as calculated numerically for the notched specimens of steels HSiII and LSi. The finite element simulations are in close agreement with the experimental results. The loadings of the different specimens unloaded for metallographic observation are indicated by rank of increasing average strain: LSi1, and from HSiII1 and to HSiII5. These specimens correspond to average strains ε_{aver} of 0.09 for steel LSi and of

[2] A more realistic description of the flow properties of this type of material should be based on a microscopic modelling of a multiphase elastoplastic composite material.

0.023, 0.06, 0.09, 0.23 and 0.53 for steel HSiII. It is noteworthy that coalescence of microvoids was observed at the tip of the notches at ε_{aver}=0.53. As for uniaxial tensile testing (figure 7.2), steel HSiII sustains higher stresses.

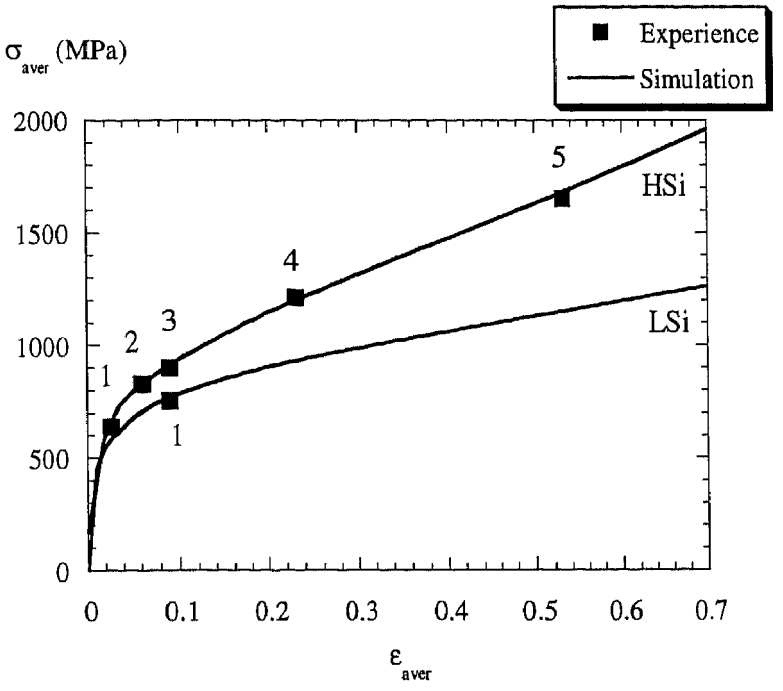

Figure 7.7: Numerical average stress (σ_{aver}) – average strain (ε_{aver}) curve and experimental results of the notched specimens of steels HSiII and LSi. Each number on this figure corresponds to a unloaded specimen used for the metallographic characterisation of transformation and damage.

The maps of figure 7.8 present the percentage of martensitic transformation of retained austenite (observed by metallography), the density of accumulated work computed from numerical simulations, and the sites and types of damage for specimens HSiII2 (ε_{aver} = 0.06 – figs. 8(a), (b), (c)), HSiII3 (ε_{aver} = 0.09 – figs. 8(d), (e), (f)) and LSi1 (ε_{aver} = 0.09 – figs. 8(g), (h), (i)).

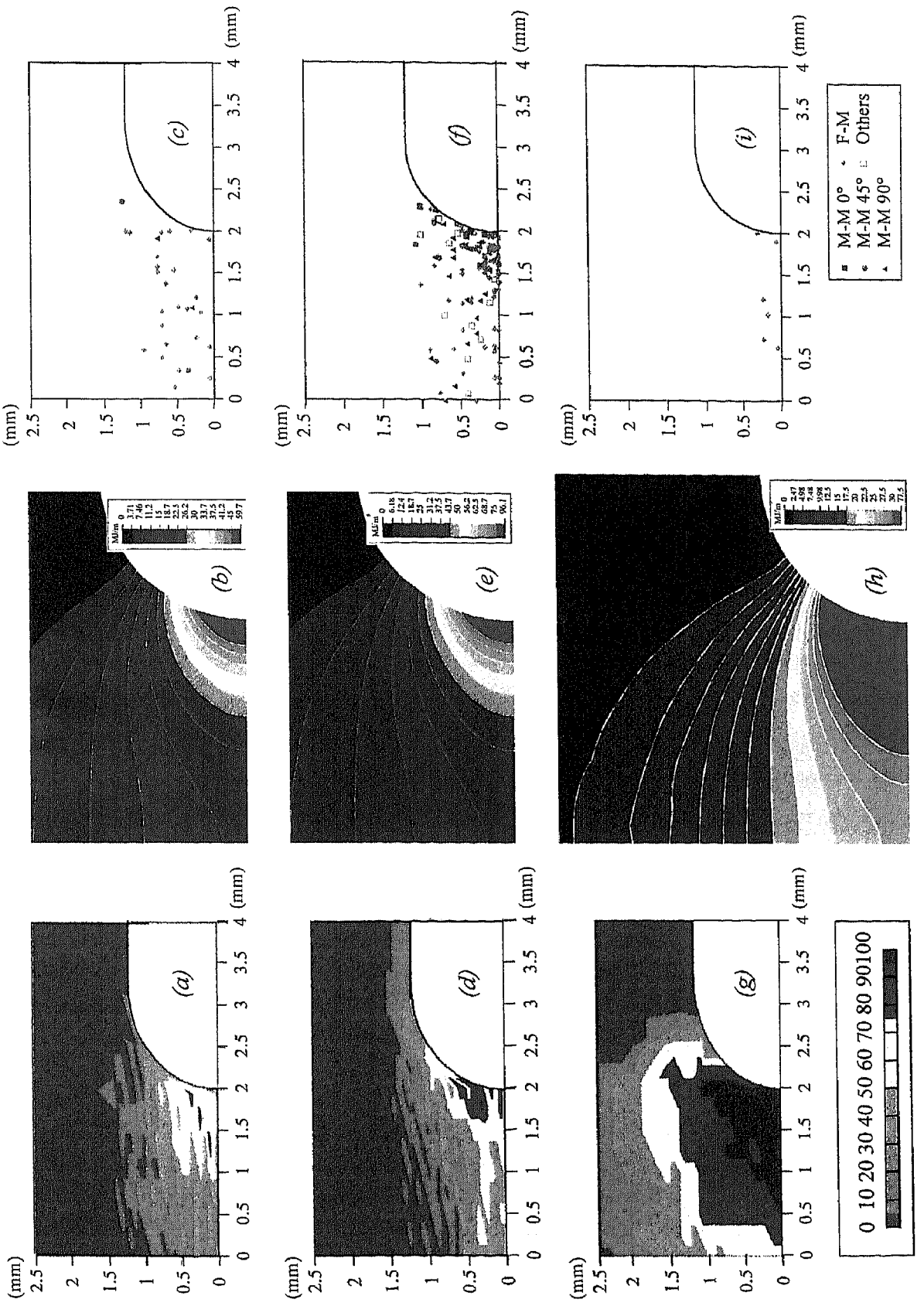

Figure 7.8: Maps covering ¼ of the notched specimens presenting the percentage of martensitic transformation, the numerically estimated density of accumulated work, and the sites of the various types of damage for specimens HSiII2 (ε_{aver}=0.06), HSiII3 (ε_{aver}=0.09) and LSi1 (ε_{aver}=0.09). Each line corresponds to a specimen (HSiII2 (a-b-c), ...). Each column corresponds to a parameter (martensitic transformation (a-d-g), ...).

Dealing first with the transformation rate of retained austenite, it can be seen in figures 7.8(a) and 7.8(d) that martensitic transformation occurs progressively in steel HSiII. The notch of specimen HSiII2 (ε_{aver} = 0.06; figure 7.8(a)) is surrounded by an approximately semi-circular zone in which 50 to 75% of the initial content of austenite has already transformed. Specimen HSiII3 (ε_{aver} = 0.09; figure 7.8(d)) shows an increase of the transformed part of austenite: more than 25% of retained austenite has transformed into martensite in almost the entire ligament. Furthermore, martensitic transformation is complete or at least higher than 75% at the notch. In contrast, specimen LSi1 (figure 7.8(g)), for which the average strain is 0.09 like in specimen HSiII3, shows a nearly complete transformation in a wide region covering the entire ligament. Hence, consistently with the expected lower stability of austenite resulting from its lower carbon content, martensitic transformation occurs more rapidly in steel LSi in such a way that no more austenite can be found in the ligament after an average strain of 0.09.

An obvious relationship exists between the contours of some level of martensitic transformation (figures 7.8(a), (d), (g)) and the contours of some density of work calculated from the finite element simulations (figures 7.8(b), (e), (h)). Figure 7.9 presents the variation as a function of average strain of the density of work corresponding to different proportions of martensitic transformation in the ligament of the notched plates HSiII and LSi. This variation was obtained by superposing the two maps and by finding the best correspondence between the contours of iso-transformation and the contours of iso-work. It is quite remarkable that, for an increasing average strain, the experimentally observed zones of iso-transformation (represented in figure 7.9 by the onset of transformation (0%), 50% transformation and complete transformation) quite well correspond to constant values of the density of work. Finite element simulations revealed a stress triaxiality of about 0.52 in the mid-plane plane at the centre of the ligament. This stress triaxiality remains nearly constant all along the ligament and decreases to the uniaxial testing value (1/3) close to the notch. The stress triaxiality also remains constant during loading and decreases slowly with distance from the minimum section of the ligament (i.e. from the region analysed metallographically). It is also worth noting that high levels of work density are required for triggering martensitic transformation in steel HSiII, especially for the last 50% of retained austenite. In contrast, the austenite of steel LSi transforms more rapidly at lower accumulated work density levels.

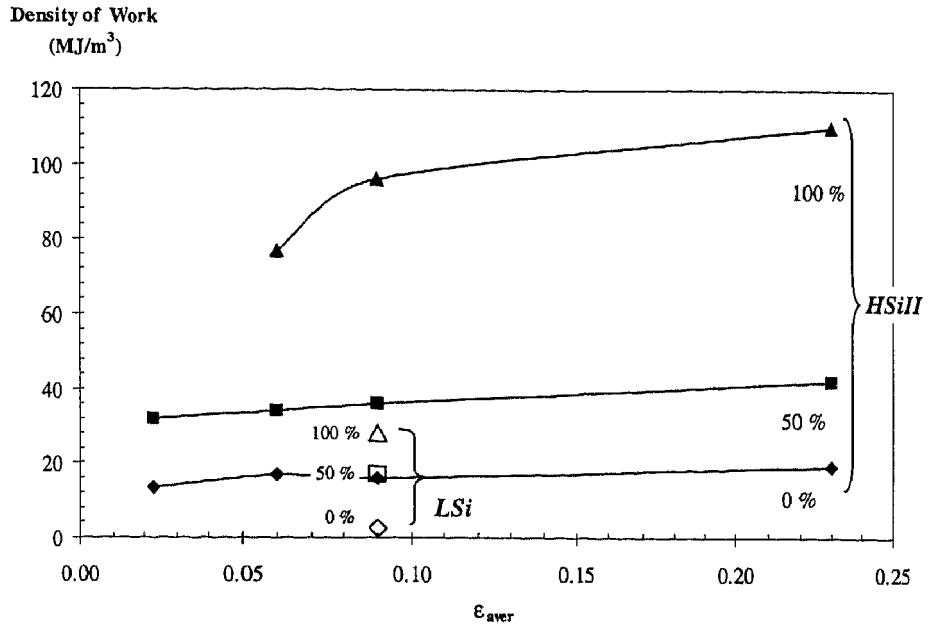

Figure 7.9: Critical density of work corresponding to the onset of martensitic transformation (0%), to 50% transformation and to the complete transformation of retained austenite in steels HSiII and LSi as a function of average strain (ε_{aver}). The curves were established by comparing the transformation maps and the density of work maps of figure 7.8.

Figures 7.8(c), (f) and (i) show that damage in steels HSiII and LSi varies in an inverse manner than martensitic transformation. Indeed, figure 8(i) shows that almost no damage site can be found when a notched specimen of steel LSi is strained up to an average strain of 0.09. On the other hand, specimens HSiII2 with $\varepsilon_{aver} = 0.06$ presents already numerous damage sites (figure 7.8(c)). At this strain level, damage mainly consists of ferrite-martensite interface debonding. Almost no cracking of martensite grains can be observed. Furthermore, damage sites are uniformly distributed in the entire strained region. For specimen HSiII3 with $\varepsilon_{aver} = 0.09$ (figure 7.8(f)), the number of damage sites shows a steep increase. However, this rise is predominantly due to the cracking of martensite grains. Indeed, a large number of cracked martensite grains can be observed in specimen HSiII3, especially in a zone of about 1mm radius around the notch (in which figure 7.8(d) has shown that martensitic transformation of retained austenite was nearly complete). The damage increase mainly results from the increase of the number of microcracking sites. Indeed, no evidence of microcrack extension or void growths can be observed after nucleation.

Figure 7.10 presents a more explicit representation of the variation of the proportion of the various types of damage sites as a function of ε_{aver} for steel HSiII. Types of damage mentioned as 'others' are ferrite or bainite cracking events that remain little significant at

all average strain. This means that the occurrence of damage in this type of microstructure necessarily involves martensite. Furthermore, the reversal of the proportions of ferrite-martensite debonding sites and martensite cracking sites occurs when ε_{aver} increases from 0.06 to 0.09. These proportions then remain constant during further straining. It is noteworthy that the steep increase of the martensite grains cracking is observed at the tip of the notch where figure 7.8(d) has shown that martensitic transformation was almost complete. This complete transformation leads to the formation of a nearly continuous bainite-martensite network. The larger fraction of sites MM90° and MM45° in figure 7.8(f) shows that cracking of the martensite grains occurs mainly in a direction perpendicular to the axis of loading.

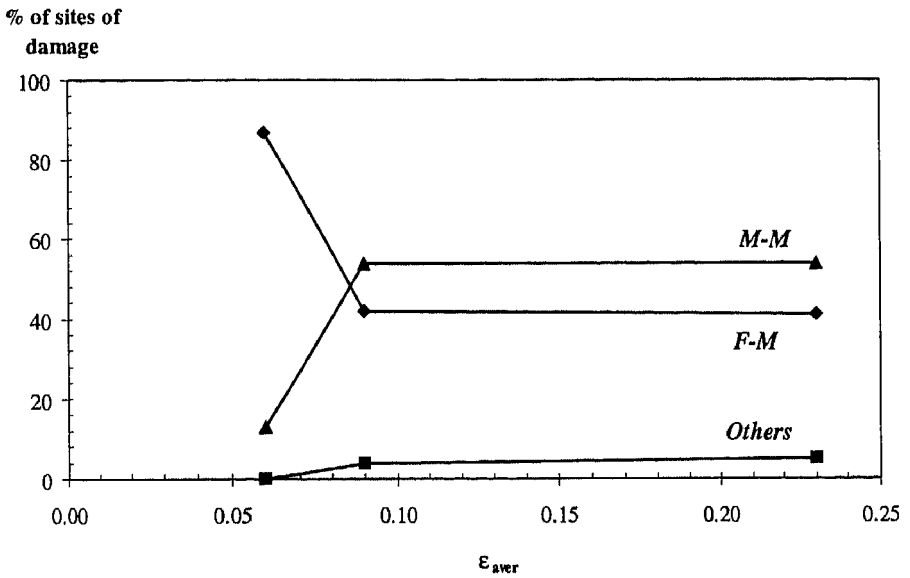

Figure 7.10: Proportions of the different types of sites of damage appearing in the microstructure of steel HSiII as a function of the average strain (ε_{aver}).

4.2. Fracture toughness

Asymmetry of the crack advance at the two specimen sides was sometimes observed during monotonic tensile loading of the DENT specimens. The specimens presenting a too large asymmetry of the crack propagation were not accounted for in the foregoing analysis. Tunnelling effects was evidenced. Typically, for crack advances larger than 1 mm, a difference of about 100-200μm was measured between the crack length at the mid-thickness and at the surface. Figure 7.11 compares the JR curves of steels HSiII and LSi. The values $J_{0.2}$ of J at the intersection with the 0.2mm offset line (parallel to the blunting line) are 220 kJ/m^2 and 350 kJ/m^2 for HSiII and LSi, respectively. Steel LSi thus presents an engineering fracture toughness significantly larger than steel HSiII. Nevertheless, for several reasons addressed hereafter, these values do not carry much physical meaning. The

tearing moduli are equal to 210 and 242 for steels HSiII and LSi, respectively. The difference between these 2 tearing moduli is of the same order as the experimental error.

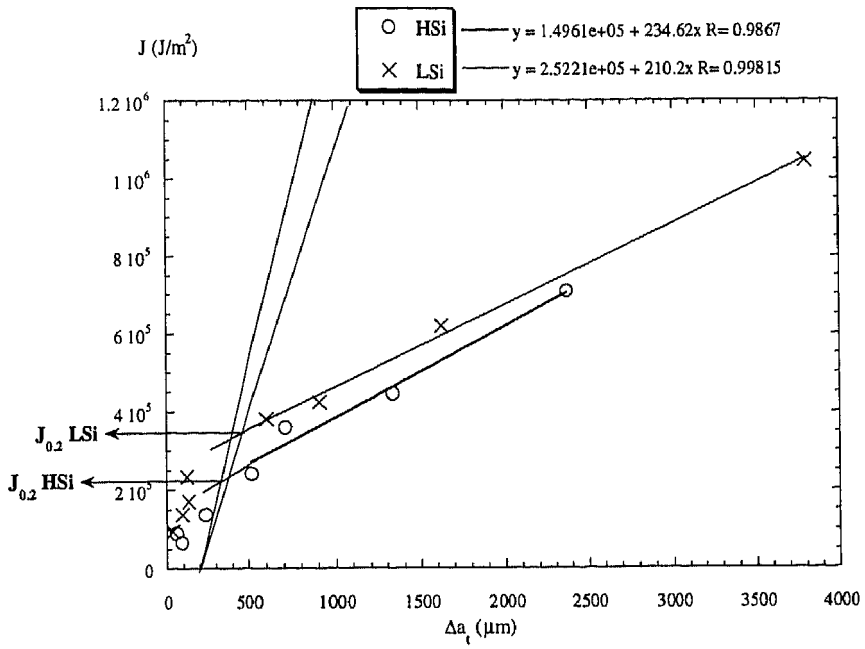

Figure 7.11: J as a function of total crack advance (JR curves) of steels HSiII and LSi.

The variations of δ_1 - δ_2 as a function of Δa_r measured at the crack tips at which cracking initiation was detected are plotted on figure 7.12 for both steels HSiII and LSi. One point corresponds to one side of the specimen: δ_1 - δ_2 is the average of the values measured on the various through thickness positions and Δa_r is the corrected crack advance for the corresponding crack. Each value is thus local, representative of one crack tip state. The experimental scatter on δ_1 - δ_2 is rather large for two reasons: (i) the limited number of observations along one crack front due to the difficulty of polishing the samples and the labor intensive character of the method, (ii) the small value of the crack opening, especially at small crack advances (especially, δ_2 is inaccurate for small crack advances). A linear regression on the δ_1 - δ_2 / Δa_r relationship gives values of δ^*_c equal to 81 μm and 52 μm for steels LSi and HSiII, respectively. The finite element simulations of the testing of the DENT specimens allowed estimation of the elastic unloading correction factor to be applied on δ^*_c [Pard98a]. Several attempts were required in order to find the displacement which gave a numerical unloaded CTOD equal to the experimental δ^*_c. The correction factors are equal to 13 μm and 8 μm for steels LSi and HSiII, respectively which means values of δ_c equal to 94 μm and 60 μm for steels LSi and HSiII, respectively. The evaluation of the part of the correction factor due to reverse plasticity is approximate because of the use of a J2 flow theory. Indeed, Bauschinger effects as well as the fact that

the TRIP effect is not reversible are not accounted for. Anyway, these approximations only result in an error on a small correction factor and do not modify significantly the result.

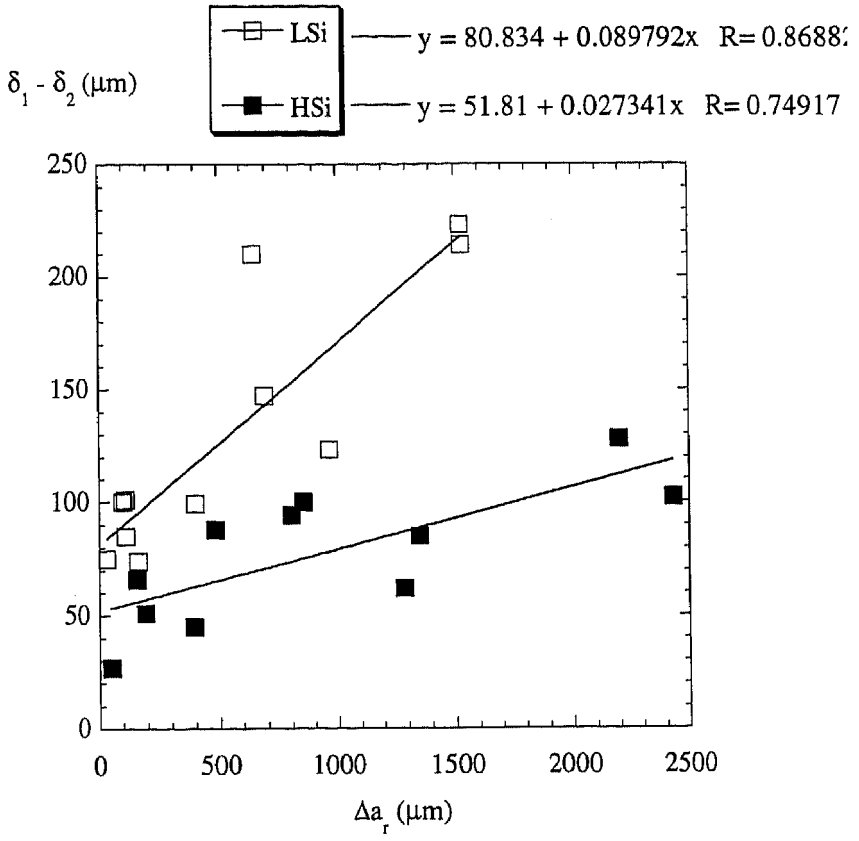

Figure 7.12: Variations of δ_1 - δ_2 as a function of Δa_r for crack tips at which cracking initiation was detected for steels HSiII and LSi.

δ_C has more physical sense for characterising fracture initiation than $J_{0.2}$ because $J_{0.2}$ is not defined at the physical crack initiation and because $J_{0.2}$ was computed using the approximate formula (1). FE simulations were also used in order to translate δ_C into a physical value of J_C. Figure 7.13 presents the variations of J (computed by the domain integral method) as a function of the CTOD for both materials. The solution predicted by Shih for pure plane stress is also added on figure 13. The stress state in the studied DENT specimens is very close to the solution of Shih and can thus be considered globally perfect plane stress. Of course, in the finite strain zone, a rise of the stress triaxiality is observed and the stress state is there intermediate between plane stress and plane strain (see also [Naka90] or [Hom90]). J_C values of about 65 kJ/m^2 for steel LSi and equal to 51 kJ/m^2 for steel HSiII are obtained using figure 7.13. These values are much smaller than the values of $J_{0.2}$ obtained from figure 7.11. Several reasons can justify this discrepancy: (i) crack initiation starts well before Δa = 0.2 mm (in fact, cracking initiates for Δa < 0.05 mm in both steels); (ii) formula (1) was found to overestimate by a factor 1.4 the value of J computed more exactly using the energy domain integral method; (iii) it is well known that for specimens with large strain hardening exponent the slope of the ASTM blunting line

equal to 2 $\Delta a(\sigma_y+\sigma_{ult})/2$ is too small [Kama98]. The finite element simulations also proved path independence of the J integral. Finally, one must recall that the measures of fracture toughness must be analysed with caution because they are obtained with thin plates and are thus very dependent on plates thickness [Pard98b]. They can thus be compared only with results obtained on plates of similar thickness.

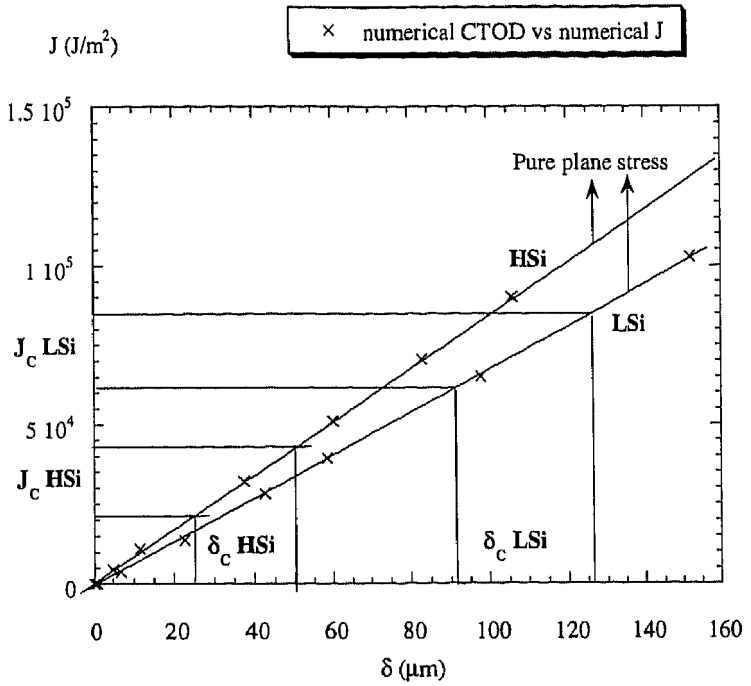

Figure 7.13: Variations of J (computed by the domain integral method) as a function of the CTOD for steels HSiII and LSi. The 'pure plane stress solution predicted by Shih has also been indicated.

As for notched specimens, the percentage of martensitic transformation and the density of accumulated work were also investigated around the crack tip of the DENT specimens. By comparison of experimental observations of martensitic transformation and finite element simulations, values of work density of 14, 30 and 44 MJ/m^3 were found for transformation levels of 0, 50 and 100%, respectively, in steel HSiII. These results are in very good agreement with the results of figure 7.9 established using notched specimens. As a matter of fact, mechanical loading is not so different in the cases of notch and DENT geometries when considering stress triaxiality: outside the finite strain zone (which has a length equal to about 2 CTOD), the stress triaxiality is found constant, equal to about 0.6 in both steels, i.e. close to the value predicted by Shih [Shih83]. This value is close to the value of the stress triaxiality in the notched specimens. The less stable austenite in steel LSi brings about a still larger zone of complete transformation covering almost half of the ligament. For steel LSi, the agreement with the results of figure 7.9 is less good. A slight stress triaxiality effect might thus exists in the DENT specimen of steel LSi. Stress triaxiality would promote martensitic transformation at lower strain. However, a more detailed

characterisation of the transformation in steel LSi should be completed in order to quantify this effect more precisely. The zone of 100% of transformation is equal roughly to 5 times the CTOD in steel HSiII but is very much larger in steel LSi.

In summary, whatever the method by which fracture toughness is evaluated, a significant difference exists between the resistance against cracking initiation of steels LSi and HSiII. However, the 2 steels appear to present similar crack propagation resistance.

5. Discussion

TRIP-assisted multiphase steels present the unique feature that part of the phases constituting the microstructure continuously changes during mechanical solicitation.

Figures 7.8 and 7.9 have shown that for the notched geometry, retained austenite transforms more rapidly in steel LSi than for steel HSiII. This result is in good agreement with the previous results of chapters V and VI dealing with the mechanical stability of retained austenite during uniaxial tensile test. Steels HSiII and LSi mainly differ by their silicon content. Silicon influences mechanical stability of retained austenite by hindering carbide precipitation during bainitic tempering and by therefore allowing a larger carbon enrichment of austenite (see chapter III). As already mentioned, the retained austenite in steel HSiII therefore contains 0.9wt.% of carbon while the carbon level of austenite in steel LSi is only of 0.73wt.%. As carbon is the best austenite stabiliser element, a carbon richer austenite means that the M_s temperature is lower so that more work is needed in order to trigger martensitic transformation. Figure 7.9 shows that a large increase of the density of accumulated work is needed in order to transform the last 50% of retained austenite in steel HSiII. Metallography indicates that this part of austenite that transforms the last corresponds to the film type austenite associated with bainite observed on the SEM micrographs of figure 7.1. It was already reported that the higher stability of this type of austenite should be attributed to a higher carbon content, a size stabilising effect and to a constrain effect due to the adjacent finely grained bainitic ferrite (see chapter V). In the case of steel LSi, no drastic increase of the density of accumulated is observed work between 50% transformation and complete transformation since the amount of film type austenite is expected to be lower (despite a relatively larger fraction of bainite). As a consequence of the lower silicon content, carbide precipitation occurs during bainitic tempering of steel LSi (see chapter III), especially in the interlath film type austenite which is the most carbon rich austenite. The density of accumulated work needed for the complete transformation of austenite in steel LSi is thus lower than the density of

accumulated work for 50% transformation in steel HSiII as a result of both the lower carbon content of austenite (chemical stabilisation) and the absence of film type austenite (morphological stabilisation). Furthermore, silicon is also known as a potent solid-solution strengthening element [Lesl72, Sugd88, Pick92]. Idiomorphic ferrite matrix is therefore a less effective load carrier in steel LSi where the silicon content is lower. Retained austenite thus carries a larger part of the load, which brings about an lower apparent lower stability (see chapter V). The present chapter therefore confirms that the composition and heat-treatment parameters of steel HSiII lead to a very stable austenite also in configurations presenting smooth strain gradients.

Micromechanical models for predicting the transformation kinetics in multiphase polycrystals have been introduced by several authors [Strin92, Bhat94, Cher98]. From the results of figure 7.9, a phenomenological mesoscopic criterion based on the density of accumulated work was proposed for the martensitic transformation of retained austenite. It can be assumed that the transformation rate of retained austenite is related to the density of spent work through a factor g describing the efficiency this work for inducing transformation. Further assuming that the transformation of the blocky type austenite is complete before the film type austenite starts to transform (as shown in chapter V), we can express the rate of transformation as:

$$\dot{f} = g_1\left(\frac{\Sigma_m}{\Sigma_{eq}}, f, \Theta\right)\Sigma_{ij}dE_{ij} \quad \text{if} \quad f < a \quad \text{and} \quad \int_0^f \Sigma_{ij}\frac{\partial E_{ij}}{\partial f}df > W_{nuclblock} \qquad (3a)$$

$$\dot{f} = g_2\left(\frac{\Sigma_m}{\Sigma_{eq}}; f, \Theta\right)\Sigma_{ij}dE_{ij} \quad \text{if} \quad f > a \quad \text{and} \quad \int_0^f \Sigma_{ij}\frac{\partial E_{ij}}{\partial f}df > W_{nuclfilm} \qquad (3b)$$

where f is the proportion of transformed austenite, a is the amount of blocky type austenite, $W_{nuclblock}$ is the strain energy density for the nucleation of the first martensitic variants corresponding to blocky type austenitic grains, $W_{nuclfilm}$ is the strain energy density for the nucleation of the first martensitic variants corresponding to film type austenitic grains, Σ_{ij} is the mesoscopic Cauchy stress tensor, E_{ij} is the mesoscopic strain tensor, Σ_m is the hydrostatic stress, Σ_{eq} is the von Mises stress, Σ_m/Σ_{eq} is the stress triaxiality, Θ is a normalised temperature (as defined by Stringfellow [Strin92] and related to M_s^{σ} and M_d in such a way that it corresponds to an intrinsic parameter of the mechanical stability of austenite), g_1 and g_2 are two unknown functions of non-dimensional parameters whose analytical expression contain constants depending on chemical parameters (like the carbon content) and microstructural parameters (blocky or film type of austenite, form of the grains, ...). The 'mesoscopic' scale refers to a representative cell which typically contains

a large number of grains thus averaging the composite effects and avoiding to consider the distribution and orientation of the various phases. If, as a first approximation, we assume (i) that the use of J2 modelling is realistic for modelling the mesoscopic response of a cell of material (thus that the coupling between the transformation and the flow behaviour can be neglected); (ii) that the parameters $W_{nuclblock}$, $W_{nuclfilm}$ are independent of the stress state; (iii) that the loading is isothermal; and (iv) that the functions g_1 and g_2 are constants independent of the stress state and of the value of f (there is indeed no autocatalytic effect in TRIP-aided steels since retained austenite is present as a dispersed phase with isolated grains within the idiomorphic ferrite matrix), one can write

$$f = g_1\left(\int \Sigma_{ij}\frac{\partial E_{ij}}{\partial f}df - W_{nuclblock0}\right) \tag{4a}$$

$$f = g_2\left(\int \Sigma_{ij}\frac{\partial E_{ij}}{\partial f}df - W_{nuclfilm0}\right) \tag{4b}$$

Assumptions (i) seems validated by the experimental results and assumptions (ii), (iii) and (iv) are validated by the limited range of the parameters variation observed in the present study (and can thus not be used in more general applications). Stringfellow et al. [Strin92] have shown that a change of stress triaxiality from 1/3 to 0.6 does not much modify the rate of transformation. This range of stress triaxiality corresponds to the range of stress triaxiality simulated in the notched specimens and in the DENT specimens (outside the finite strain zone). In steel HSiII, a = 0.5 (determined metallographically) and W_{nucl0}, $1/g_1$ and $1/g_2$ in (3a) and (3b) are thus equal to 16, 40 and 116 MJ/m^3, respectively, if we assume that transformation of the film type austenite starts just after the blocky type austenite has completely disappeared. In material LSi, a = 1 (almost no film type austenite can be found in steel LSi as a result of carbide precipitation) and W_{nucl0} and $1/g_1$ are equal to 3 and 25 MJ/m^3, respectively. In other words, a significant difference exists between the two steels for the first nucleation events and for the energy required for continuing transformation in the 2 types of austenite. The use of the strain energy density as the driving force follows the experimental evidence of figure 7.8. In the work of Stringfellow [Strin92], the account for plastic straining is rendered more complex due to the fact that the transformation depends on the intersection of shear bands as a result of the non homogeneous character of the plastic flow in very high strength steels. In the present study, the material did not present such a high strength and plastic mechanisms are more homogeneous. Further study would aimed at regarding more realistic g_1 and g_2 functions from both experimental and micromechanical analysis and at comparing the response of the J2 model with a more sophisticated flow model accounting first for the transformation

(at least phenomenologically by introducing a dependence of the strain hardening on the stress triaxiality) and for the composite structure and the transformation.

The fact that the same work density criterion was found to work in the case of the DENT specimens results from the similar stress triaxialities. Inside the FPZ, the prediction of the stress by the J2 model probably breaks down because stress triaxiality peaks to a 1.5 value, which presumably cause an increase of the transformation rate.

This study shows that damaging of TRIP-aided steels results from the martensitic transformation. This behaviour is very different from the behaviour of steels where transformation preserves the steel from damage [Olson96]. In the present case, martensitic transformation is responsible for the creation of the damage sites. Any damage modelling will first require a correct model for predicting the transformation kinetics. Nonetheless, the onset of martensitic transformation is not a sufficient condition for damage initiation. Indeed, as shown in figure 7.8, steel LSi with a faster martensitic transformation does not suffer more pronounced damage than steel HSiII. On the contrary, steel HSiII presents an earlier occurrence of damage. First of all, it is worth noting that the corollary of a high carbon austenite is a high strength martensite. Indeed, martensite inherits the high carbon content of the parent austenite, which brings about a high increase of its strength at the expense of ductility [Tamu82, Young94]. This gives rise to larger strain incompatibilities between ferrite and martensite so that debonding occurs more rapidly in the case of steel HSiII. Higher contents of carbon also render martensite more brittle and martensite cracking becomes therefore easier. Furthermore, figure 7.8 (7.8(a), 7.8(c), 7.8(d) and 7.8(f)) has shown that, for steel HSiII, the number of martensite grains cracking steeply increases in the zone at the tip of the notch where more than 75% of retained austenite has transformed. Steel HSiII initially contains 45% of non-idiomorphic ferrite phases, i.e. bainite and retained austenite. As shown in figure 7.1(a), these phases constitute a nearly continuous network along the ferrite grain boundaries. Martensitic transformation of more than 75% of the initial retained austenite content therefore causes the formation of a nearly continuous brittle network consisting of high strength bainite and martensite. This network allows brittle crack propagating inside the material by avoiding crossing of ductile phase. This means that, for the levels of mechanical stability of austenite involved in TRIP-assisted multiphase steels, damage is governed not only by the transformation rate but also by the amount of martensite.

Since the size of the fracture process zone (FPZ) where fracture controlling processes are localised corresponds to 2 to 4 times the CTOD [McM77], it can be concluded that, for both steels, this fracture process zone is rapidly embedded inside a zone where martensitic

transformation is complete. Consequently, the FPZ in steel HSiII rapidly consists of a continuous network of brittle second phase. Thus, even though steel HSiII has a higher strain-hardening capacity, cracking initiates more rapidly than in steel LSi. In other words, in steel HSiII, the TRIP effect has a deleterious effect on fracture toughness for two reasons: (i) the high stability of the austenite involves a high carbon content and thus a lower resistance to microcracking of martensite, (ii) a significant TRIP effect requires a large amount of retained austenite which involves thus the creation of a continuous network of brittle phases. When TRIP-aided steels are to be used in structural applications where fracture under monotonic loading is of concern, one must at least avoid the possibility of a continuous brittle network of second phases.

The picture is different for the crack propagation resistance. In steel HSiII, the fracture process zone together with the surrounding zone of complete transformation are moving along the ligament during crack propagation, part of the strain energy is spent for the transformation of the retained austenite. As a consequence, steel HSiII exhibits a similar tearing modulus as steel LSi for which no more retained austenite remains in the ligament at the moment of crack initiation. This conclusion is important because, for such steels with a high tearing modulus, the resistance to crack propagation is perhaps more significant for structural design than the resistance to cracking initiation.

During fatigue precracking of the specimen, it was also observed that the fatigue resistance of steel HSiII was markedly higher than that of steel LSi. This result is in agreement with the fact that fatigue cracking depends on the flow properties of the material and namely on the emission of dislocations at the crack tip. The problem of fatigue will deserve more attention in future works

6. Conclusion

This chapter has characterised the damage and fracture resistance of 2 TRIP-assisted multiphase steels differing by their retained austenite content and stability and by proportion of the other phases in their microstructure. It was shown that, for the levels of austenite stability commonly involved in TRIP-aided steels, no mechanically induced martensitic transformation occurs in the fracture process zone: cracking initiates in a FPZ containing only martensite and no more retained austenite. The effect of martensitic transformation on damaging is mainly related to the volume fraction of martensite and to the mechanical properties of martensite which is strongly dependent on carbon content. As a consequence, although steel HSiII features improved flow properties thanks to a large

amount of stable, high carbon retained austenite, this steel exhibits a lower fracture toughness than steel LSi because of the presence, in the fracture process zone, of a nearly continuous network of high strength bainite and brittle martensite. Premature cracking of martensite grains brings about faster cracking initiation. Whereas literature dealing with TRIP-assisted multiphase steels recommends high amounts of stable austenite in order to enhance the strength-ductility balance, this study shows that enhancement of the balance between resistance to plastic instability and resistance to cracking requires a limitation of the amount of retained austenite in order to avoid premature damaging due to a 'brittle network' effect. Nevertheless, even if the mechanical stability of retained austenite is too low for austenite to remain untransformed in the fracture process zone (and therefore to be able to improve fracture toughness as observed in other steels), the mechanically-induced martensitic transformation of retained austenite spends part of the strain energy during crack propagation, an effect which can improve fracture toughness by somewhat compensating for the effect of the brittleness of martensite.

Preliminary results suggest that the fatigue resistance of steel HSiII is higher than that of steel LSi. It could be speculated that the parameters controlling the sub-critical propagation of a fatigue crack are related to the flow properties rather than to the damage mechanisms characterised in this chapter.

This study has also shown that a phenomenological mesoscopic criterion based on a critical density of work can be used for predicting the mechanical activation of martensitic transformation of retained austenite. This criterion works as well for notched specimens as for DENT specimens since the stress state in sheets is less dependent on geometry than the stress state in thick specimens.

References

[Anto71] S.D. Antolovich, and B. Singh: *Metall. Trans.*, 1971, vol. 2, pp. 2135-2141

[Bhat94] A. Bhattacharyya A., and G.J. Weng: *J. Mech. Phys. Solids*, 1994, vol. 42, pp. 1699-1724

[Chen84] J.H. Chen, Y. Kikuta, T. Araki, M. Yoneda, and Y. Matsuda: *Acta Metall.*, 1984, vol. 32(10), pp. 1779-1788

[Cher98] M. Cherkaoui, M. Berveiller, and H. Sabar: *Int. J. Plasticity*, 1998, vol. 14, pp. 597-626

[Fult85] B. Fultz, J.I. Kim, Y.H. Kim, H.J. Kim, G.O. Fior, and J.W. Morris: *Metall. Trans. A*, 1985, vol. 16A, pp. 2237-2249

[Haid87] G.N. Haidemenopoulos, G.B. Olson, and M. Cohen: *Proc. 34th Sagamore Army Materials Research Conf.*, Lake George, New York, 1987, pp. 549-593

[Haid88] G.N. Haidemenopoulos: PhD Thesis, MIT, 1988

[Haid89] G.N. Haidemenopoulos, G.B. Olson, M. Cohen, and K. Tsuzaki: *Scripta Metall.*, 1989, vol. 23, pp. 207-212

[Hom90] C.L. Hom, and R.M. McMeeking: *Int. J. Fract.*, 1990, vol. 45, pp. 103-122

[Hutch83] J.W. Hutchinson: *Trans. ASME*, 1983, vol. 50, pp. 1042-1051

[Kama98] S.V. Kamat, M. Srinivas, and P. Rama Rao: *Acta Mater.*, 1998, vol. 46, pp. 4985-4992

[Leal84] R.H. Leal: PhD Thesis, MIT, 1984

[Lesl72] W.C. Leslie: *Metall. Trans.*, 1972, vol. 3, pp. 5-26

[Lud69] D.C. Ludwigson, and J.A. Berger: *J. Iron and Steel Inst.*, 1969, pp. 63-69

[McM77] R.M. McMeeking: *J. Mech. Phys. Solids*, 1977, vol. 25, pp. 357-381

[Miih87] V.T.T. Miihkinen, and D.V. Edmonds: *Mater. Sc. Technol.*, 1987, vol. 3, pp. 441-449

[Naka90] T. Nakamura, and D.M. Parks: *J. Mech.Phys. Solids*, 1990, vol. 38, pp. 787-812

[Olson75] G.B. Olson, and M. Cohen: *Metall. Trans. A*, 1975, vol. 6A, pp. 791-795

[Olson78] G.B. Olson, and M. Azrin: *Metall. Trans. A*, 1978, vol. 9A, pp. 713-721

[Olson82a] G.B. Olson, and M. Cohen: *Metall. Trans. A*, 1982, vol. 13A, pp. 1907-1914

[Olson82b] G.B. Olson: *Deformation, processing and structures*, G. Krauss, ed. ASM, 1982, pp.391-424

[Olson96] G.B. Olson: *J. de Physique IV*, 1996, pp. C1-407 – C1-418

[Pard98a] T. Pardoen, and F. Delannay: Submitted to *Engineering Fracture Mechanics*, 1998

[Pard98b] T. Pardoen, Y. Marchal, and F. Delannay: Submitted to the *J. Mech. Phys. Solids*, 1998

[Park75] E.R. Parker, and V.F. Zackay: *Eng. Frac. Mech.*, 1975, vol. 7, pp. 371-375

[Pick92] F.B. Pickering: *Materials Science and technology – Vol. 7: Constitution and Properties of Steels*, F.B. Pickering ed., VCH Publ., Weinheim, 1992, pp. 41-94

[Rao80] B.V.N. Rao, and G. Thomas: *Metall. Trans. A*, 1980, vol. 11A, pp. 441-457

[Rice68] J.R. Rice: *J. Appl. Mech*, 1968, vol. 35, pp. 379-386

[Rice73] J.R. Rice, P.C. Paris, J.G. Merkle: *Progress in Flaw Growth and Fracture Toughness Testing*, ASTM STP 536, American Society for Testing and Materials, 1973, pp. 231-245

[Sand81] B.P.J. Sandvik, and H.P. Nevalainen: *Metal Technol.*, 1981, pp. 213-220

[Shih83] C.F. Shih: *Tables of Hutchinson-Rice-Rosengren Singular Field Quantities*, MRL E-147, Division of Engineering, Brown University, Providence, R.I., 1983

[Shih86] C.F. Shih, B. Moran, and T. Nakamura: *Int. J. Fract.*, 1986, vol. 30, pp. 79-102

[Spei81] G.R. Speich: *Fundamentals of Dual-Phase Steels*, R.A. Kot and B.L. Bramfitt, eds., TMS-AIME, Warrendale, PA, 1981, 3-45

[Strin92] R.G. Stringfellow, D.M. Parks, and G.B. Olson: *Acta Metall. Mater.*, 1992, vol. 40(7), pp. 1703-1716

[Sugd88] A.A.B. Sugden, and H.K.D.H. Bhadeshia: *Metall. Trans. A*, 1988, vol. 19A, pp. 1597-1602

[Tail95] R. Taillard, P. Verrier, T. Maurickx, and J. Foct: *Metall. Trans. A*, 1995, vol. 26A, pp. 447-457

[Tail96] R. Taillard, P. Verrier, and T. Maurickx: *J. de Physique IV*, 1996, pp. C1-245 – C1-255

[Tamu82] I. Tamura: *Metal Sc.*, 1982, vol. 16, pp. 245-253

[Tamu92] I. Tamura, and C.M. Wayman: *Martensite*, G.B. Olson and W.S. Owen ed, ASM, 1992, pp. 227-242

[Tomi93] Y. Tomita, and T. Okawa: *Mater. Sc. Eng. A*, 1993, vol. A172, pp. 145-151

[Tomi95] Y. Tomita: *Z. Metallkd.*, 1995, vol. 86, pp. 568-574

[Tver81] V. Tvergaard: *Int. J. Fract.*, 1981, vol. 17, pp. 389-407

[Tver82] V. Tvergaard: *Int. J. Fract.*, 1982, vol. 18, pp. 237-251

[Wod75] W.E. Wood: *Eng. Frac.Mech.*, 1975, vol. 7, pp. 219-234

[Yano73] S. Yano, H. Sakurai, H. Mimura, N. Wakita, T. Ozawa, and K. Aoki: *Trans. ISIJ*, 1973, vol. 13, pp. 133-140

[Young94] C.H. Young, and H.K.D.H. Bhadeshia: *Mater. Sci. Technol.*, 1994, vol. 10, pp. 209-214

[Zack67] V.F. Zackay, E.R. Parker, D. Fahr, and R. Busch: *Trans. Am. Soc. Met.*, 1967, vol. 60, pp. 252-259

Conclusions and Prospects

TRIP-assisted multiphase steels are foreseen to be used as high strength formable steels in automotive applications facing drastic requirements of reductions of weight and improvement of safety. The steels studied up to now contain high levels of silicon which are incompatible with the common production practice of strip products. The present thesis enlightens the physical principles (i) allowing the formation of a multiphase microstructure containing retained austenite and (ii) influencing the deformation processes during mechanical testing. Furthermore, this thesis leads to the development of a new low silicon TRIP-assisted multiphase steel with improved mechanical properties and compatible with the industrial practice.

This work contributes to:

(1) a better understanding of the phase transformations occurring during the thermal processing of cold-rolled TRIP-assisted multiphase steels;

(2) a description of the relevant parameters of the microstructure influencing (a) the plastic properties and (b) the toughness properties.

(1) Bainite transformation plays an important role in the generation of the microstructure of TRIP-assisted multiphase steels and therefore on the resulting mechanical properties. The amount of silicon and the temperature of bainitic tempering were found to be key factors for the retention or decomposition of austenite.

The bainite transformation of conventional high silicon TRIP-assisted multiphase steels occurs following different steps. The first stage corresponds to the displacive formation of bainitic ferrite with carbon redistribution into residual austenite. This formation

proceeds until carbon enrichment of austenite attains the level of the T_0-curve in such a way that large amounts of austenite can be retained in the room temperature microstructure. A secondary stage corresponding to the precipitation of carbides from austenite was found to occur during prolonged tempering.

In the case of a low silicon steel, both the formation of bainitic ferrite and the precipitation of carbides occur simultaneously. Nevertheless, the carbide precipitation is slightly delayed so that up to 10% of carbon enriched retained austenite can be found in the room temperature microstructure despite a silicon level of 0.38wt.%.

Furthermore, the transformation kinetics is strongly dependent on the temperature of bainitic tempering because the grain size of intercritical austenite is of the same order as the length of the bainitic ferrite sub-units and because of the isolated nature of austenite dispersed in idiomorphic ferrite.

(2) Mechanical properties of TRIP-assisted multiphase steels are strongly related to some parameters of their microstructure and to the interactions occurring between the different constitutive phases.

(a) Tensile properties of TRIP-assisted multiphase steels depend on a large way on the TRIP effect. It was shown that, in both high and low silicon steels, the optimum strength-ductility balance emerges from the microstructure containing the maximum content of retained austenite which gives rise to an effective TRIP effect. However, the other phases constituting the microstructure also play a role. As a consequence, the improvement of the tensile properties of the new low silicon TRIP-assisted multiphase steel takes advantage of the strengthening by mechanically-induced martensitic transformation (the TRIP effect) and strengthening by interactions of soft ferrite and hard martensite (composite effect).

The influence of the microstructure also intervenes in the way retained austenite transforms during tensile testing at room temperature. The mechanical stability of retained austenite in TRIP-assisted multiphase steels was shown to depend on the intrinsic properties of retained austenite and on the influence of the other phases. The carbon content and the morphology of austenite first dictates its stability. However, the presence of an effective load carrier in the microstructure such as thermal martensite formed during cooling to room temperature was found to exert a shielding effect protecting austenite from the externally applied load. Dispersed

retained austenite of TRIP-assisted multiphase steels therefore exhibits an apparent stability taking into account the potential effects of the surrounding matrix.

Characterisation of the intrinsic mechanical stability of dispersed retained austenite in TRIP-assisted multiphase steels was allowed by considering the effect of the testing temperature both on the onset of yielding and on the mechanical properties measured by uniaxial tensile testing. A reversal of the temperature dependence of flow stresses at small strain offsets allows defining the temperature M_s^{σ} which is in good agreement with the austenite stabilising effect attributed to carbon enrichment and with the resulting lowering of the M_s temperature.

The use of the acoustic emission technique was revealed to constitute a very convenient technique for the study of the deformation processes occurring during straining of TRIP-assisted multiphase steels, i.e. dislocation motion and martensitic transformation. Continuous acoustic activity was related to the microscopic sources active at the onset of yielding and to the transformation rate of austenite during plastic straining.

(b) The damage and fracture resistance of TRIP-assisted multiphase steels were found not to be directly related to the TRIP effect. Indeed, for the levels of austenite stability commonly involved in TRIP-aided steels, no mechanically-induced martensitic transformation occurs in the fracture process zone. The effect of martensitic transformation on damaging is mainly related to the volume fraction and to the mechanical properties of martensite. Enhancement of the resistance to cracking requires a limitation of the amount of retained austenite in order to avoid premature damaging due to a brittle network effect. A phenomenological mesoscopic criterion based on a critical density of work was found to predict the mechanical activation of martensitic transformation of retained austenite both for notched and DENT specimens.

Prospects

This thesis has shown that remarkable mechanical properties can be obtained in a TRIP-assisted multiphase steel containing only 0.38wt.% of silicon. This result is in contrast with published results on TRIP-aided steels in which high silicon contents are reported to be necessary to stabilise austenite. Pursuing the investigation of the bainite transformation of such low silicon steels would constitute a major extension of this work in order to precisely

determine how silicon delays or inhibits carbide precipitation. Furthermore, the kinetics of the bainite transformation of intercritical austenite was shown to be drastically dependent on the tempering temperature. It would also be of primary importance to complement the present models describing the kinetics of bainite transformation such as the model of Bhadeshia by integrating the influence of local carbon supersaturation and the effect of carbide precipitation. Finally, investigating the effect of other alloying elements (such as aluminium) on the retention of austenite should constitute another part of further research in this field.

This thesis mainly studies the mechanical properties of TRIP-assisted multiphase steels by considering uniaxial tensile testing. A more thorough investigation of the influence of the TRIP effect and of the composite strengthening effect on the plastic properties should incorporate more complex deformation such as deep-drawing or biaxial stretching. Furthermore, preliminary results suggest that the fatigue resistance is also dependent on some parameters of the microstructure. The characterisation of the sub-critical propagation of a fatigue crack should be very useful since some applications (for example wheels) could require good fatigue properties. In the same way, some studies have shown that TRIP-aided steels do not exhibit the same behaviour as conventional steels during crash and high strain rate tests. These properties should also be assessed and understood.

All this experimental work should be accompanied by a micromechanical modelling of plastic and damage properties. This thesis has shown that mechanical properties of the TRIP-assisted multiphase steels, and particularly of the new low silicon steel, depend in a large way on the interactions between the different phases constituting the microstructure. A major extension of the present experimental work would aim at describing the flow properties of this type of material by the model of a multiphase elasto-plastic composite material. Specific experimental methods should lead to the characterisation of the mechanical properties of the individual phases. Numerical simulations should be used to compare the experimental work with the theoretically predicted results. Such a model could be used to design the next generation of high-strength formable steels with still improved mechanical properties thanks to a complete understanding of the deformation processes intervening in complex microstructures.